

## INFORMATION TO USERS

This manuscript has been reproduced from the microfilm master. UMI films the text directly from the original or copy submitted. Thus, some thesis and dissertation copies are in typewriter face, while others may be from any type of computer printer.

**The quality of this reproduction is dependent upon the quality of the copy submitted.** Broken or indistinct print, colored or poor quality illustrations and photographs, print bleedthrough, substandard margins, and improper alignment can adversely affect reproduction.

In the unlikely event that the author did not send UMI a complete manuscript and there are missing pages, these will be noted. Also, if unauthorized copyright material had to be removed, a note will indicate the deletion.

Oversize materials (e.g., maps, drawings, charts) are reproduced by sectioning the original, beginning at the upper left-hand corner and continuing from left to right in equal sections with small overlaps. Each original is also photographed in one exposure and is included in reduced form at the back of the book.

Photographs included in the original manuscript have been reproduced xerographically in this copy. Higher quality 6" x 9" black and white photographic prints are available for any photographs or illustrations appearing in this copy for an additional charge. Contact UMI directly to order.

# U·M·I

University Microfilms International  
A Bell & Howell Information Company  
300 North Zeeb Road, Ann Arbor, MI 48106-1346 USA  
313/761-4700 800/521-0600



**Order Number 9321211**

**Density functional studies: First principles and semi-empirical  
calculations of clusters and surfaces**

**Sinnott, Susan Buthaina, Ph.D.**

**Iowa State University, 1993**

**U·M·I**

**300 N. Zeeb Rd.  
Ann Arbor, MI 48106**



Density functional studies: First principles and semi-empirical  
calculations of clusters and surfaces

by

Susan Buthaina Sinnott

A Dissertation Submitted to the  
Graduate Faculty in Partial Fulfillment of the  
Requirement for the Degree of  
DOCTOR OF PHILOSOPHY

Department: Chemistry  
Major: Physical Chemistry

**Approved:**

Signature was redacted for privacy.

**In Charge of Major Work**

Signature was redacted for privacy.

**For the Major Department**

Signature was redacted for privacy.

**For the Graduate College**

Iowa State University  
Ames, Iowa

1993

This dissertation is lovingly dedicated to my husband John whose support and encouragement made this work possible.

**TABLE OF CONTENTS**

LIST OF FIGURES	vi
LIST OF TABLES	ix
ACKNOWLEDGMENTS	xi
GENERAL INTRODUCTION	1
An Explanation of the Dissertation Organization	2
Literature Review	2
Overview of Density Functional Theory	3
Details of Implementing Density Functional Theory	8
Derivation of the Corrected Effective Medium Theory	9
PAPER 1. DENSITY FUNCTIONAL STUDY OF THE BONDING IN SMALL SILICON CLUSTERS	15
ABSTRACT	17
INTRODUCTION	18
COMPUTATIONAL DETAILS	22
RESULTS	23
Si <sub>2</sub>	24
Si <sub>3</sub>	24
Si <sub>4</sub>	25
Si <sub>5</sub>	27
Si <sub>6</sub>	27
Si <sub>7</sub>	28

Si <sub>8</sub>	29
TRENDS IN BINDING ENERGIES	31
BONDING IN SILICON CLUSTERS	36
CONCLUDING REMARKS	43
NOTE ADDED IN PROOF	45
ACKNOWLEDGEMENTS	46
REFERENCES	47
PAPER 2. CORRECTIVE EFFECTIVE MEDIUM STUDY OF METAL-SURFACE RELAXATION	70
ABSTRACT	72
INTRODUCTION	73
THEORY	76
RESULTS	82
DISCUSSION AND CONCLUSIONS	91
APPENDIX	96
ACKNOWLEDGMENTS	99
REFERENCES	100
PAPER 3. EXPLORATION OF TWO-BODY APPROXIMATIONS TO THE KINETIC-EXCHANGE-CORRELATION ENERGY	123
ABSTRACT	125
INTRODUCTION	126
THEORY	129

<b>RESULTS AND DISCUSSION</b>	<b>135</b>
<b>Kinetic-Exchange-Correlation Energies</b>	<b>135</b>
<b>Total Interaction Energy Calculations</b>	<b>139</b>
<b>CONCLUSIONS</b>	<b>144</b>
<b>ACKNOWLEDGMENTS</b>	<b>146</b>
<b>REFERENCES</b>	<b>147</b>
<b>GENERAL CONCLUSIONS</b>	<b>163</b>
<b>GENERAL REFERENCES</b>	<b>164</b>

## LIST OF FIGURES

### PAPER 1

- Fig. 1:** The  $\text{Si}_3$  clusters studied. See text for the cluster labelling convention 61
- Fig. 2:** The  $\text{Si}_4$  clusters studied. See text for the cluster labelling convention. 62
- Fig. 3:** The  $\text{Si}_5$  clusters studied. See text for the cluster labelling convention. 63
- Fig. 4:** The  $\text{Si}_6$  clusters studied. See text for the cluster labelling convention. 64
- Fig. 5:** The  $\text{Si}_7$  clusters studied. See text for the cluster labelling convention. 65
- Fig. 6:** The  $\text{Si}_8$  clusters studied. See text for the cluster labelling convention. 66
- Fig. 7:** a) The disproportionation energy as a function of the number of atoms in the cluster. This is one measure of relative cluster stability. The line denotes the zero energy. b) The incremental binding energy as a function of the number of atoms in the cluster. This is another measure of cluster stability. The X's represent the experimental values, while the line indicates the bulk cohesive energy. 67
- Fig. 8:** The valency of the silicon atoms as a function of the quantity (2.0 - s-atomic population). This is the hybridization of the silicon atoms in the silicon clusters studied. 68
- Fig. 9:** The bond order of the individual Si atoms in the clusters as a function of the length of the bond. 69

### PAPER 2

- Fig. 1:** A comparison of the CEM LMTO and covalent embedding functions for Cu a) over a large range of jellium densities and b) over the surface region only. 117

- Fig. 2:** A comparison of the CEM LMTO and covalent embedding functions for Pd a) over a large range of jellium densities and b) over the surface region only. 118
- Fig. 3:** A comparison of the LMTO CEM and MD/MC-CEM embedding functions for Cu. 119
- Fig. 4:** The CEM energy components for a) Al(111) and b) Al(110) utilizing the LMTO embedding energies. Energies are in  $J/m^2$ . 120
- Fig. 5:** A comparison of the CEM energy components for Ni(110) utilizing the a) LMTO embedding energies and b) the semi-empirical embedding energies. Energies are in  $J/m^2$ . 121
- Fig. 6:** The LMTO cohesive energy curve for Ni. The line is a fifth-order Chebyshev representations in Eq. (9) and the points are the LMTO calculated values. 122

### PAPER 3

- Fig. 1:** The Ni-Ni two-body function as a function of iteration (Eq. 9). The fifth iteration is the last. It is clear that the convergence is very rapid. 154
- Fig. 2:** The Ni-Ni, Ag-Ag and Ni-Ag two-body functions. The Ni-Ag function shown is derived from the  $Ni_{0.5}Ag_{0.5}$  bulk lattice. 155
- Fig. 3:** a) The difference between  $\Delta G$  and  $\Delta G_{pair}$  for Ni over the physically relevant region of  $0.75a_0 - 1.10a_0$ . b)  $\Delta G$  as a function of lattice constant for Ni over the same region. The bulk equilibrium lattice constant for Ni is indicated on both figures. 156
- Fig. 4:**  $\Delta G_{MD/MC-CEM}$  versus jellium density for Ni. The density of an atom at the surface of Ni(100) and in the bulk lattice is indicated by the triangles. 157
- Fig. 5:** The difference between  $\Delta G$  and  $\Delta G_{MD/MC-CEM}$  versus lattice constant for  $Ni_{0.25}Ag_{0.75}$ ,  $Ni_{0.5}Ag_{0.5}$  and  $Ni_{0.75}Ag_{0.25}$ . 158
- Fig. 6:** a) The difference between the  $Ni_{0.25}Ag_{0.75}$  and  $Ni_{0.75}Ag_{0.25}$  functions and the  $Ni_{0.5}Ag_{0.5}$  function. b) The difference between  $\Delta G$  and  $\Delta G_{pair}$  for the  $Ni_{0.25}Ag_{0.75}$  and  $Ni_{0.75}Ag_{0.25}$  bulk alloy systems. Each  $\Delta G_{pair}$  calculation here uses the Ni-Ag two-body

- function derived from the  $\text{Ni}_{0.5}\text{Ag}_{0.5}$  alloy system. 159
- Fig. 7:** a) The difference between the  $\text{Ni}_{0.25}\text{Cu}_{0.75}$  and  $\text{Ni}_{0.75}\text{Cu}_{0.25}$  functions and the  $\text{Ni}_{0.5}\text{Cu}_{0.5}$  function. b) The difference between  $\Delta G$  and  $\Delta G_{\text{pair}}$  for the  $\text{Ni}_{0.25}\text{Cu}_{0.75}$  and  $\text{Ni}_{0.75}\text{Cu}_{0.25}$  bulk alloy systems. Each  $\Delta G_{\text{pair}}$  calculation here uses the Ni-Cu two-body function derived from the  $\text{Ni}_{0.5}\text{Cu}_{0.5}$  alloy system. 160
- Fig. 8:** The kinetic-exchange-correlation energy curves for  $\text{Ni}_2$  as a function of the bond length. 161
- Fig. 9:** The kinetic-exchange-correlation energy curves for a Cu atom on the surface of the Cu(100) surface as a function of the jellium density. The density was varied by contracting the first interlayer spacing from 0 - 25%. 162

## LIST OF TABLES

### PAPER 1

<b>Table I:</b>	Structural data and binding energies, which include the zero point energies, for Si clusters.	52
<b>Table H:</b>	Harmonic frequencies and zero point energies for Si clusters.	55
<b>Table III:</b>	Total energies of Si clusters using the VWN and PW potentials.	57
<b>Table IV:</b>	Theoretical and experimental estimates of the binding energies (in eV) for the global minima of $\text{Si}_n$ , $n = 2-8$ . The binding energies include the zero point energies. The equilibrium structures whose energies are reported below are as follows: 2.0.1.t; 3.0.1.t for the VWN calculations and 3.0.2.s for the MP4 calculations; 4.0.1.s; 5.0.1.s; 6.0.1.s; 7.0.1.s; and 8.0.1.s.	58
<b>Table V:</b>	PW/VWN binding energy (BE), promotion energy (PE), intrinsic binding energy (IBE) and the ratio PE/IBE for silicon clusters.	59
<b>Table VI:</b>	The PE/IBE ratio, average coordination number and HOMO-LUMO gap of the Si clusters.	60

### PAPER 2

<b>Table I:</b>	Relaxed surface energies, $\sigma$ ( $\text{J}/\text{m}^2$ ), calculated using the LMTO embedding functions.	106
<b>Table II:</b>	The percentage change in interlayer spacing and the relaxed surface energies for various interaction potentials.	107
<b>Table III:</b>	Percent relaxation of interlayer spacing for Al.	108
<b>Table IV:</b>	Percent relaxation of interlayer spacing for Ni.	109
<b>Table V:</b>	Percent relaxation of interlayer spacing for Cu.	110
<b>Table VI:</b>	Percent relaxation of interlayer spacing for Rh, Pd and Ag.	111

<b>Table VII:</b>	Relaxed surface energies, $\sigma$ ( $J/m^2$ ), calculated using the semi-empirical embedding functions.	113
<b>Table VIII:</b>	Percentage change in the interlayer spacing calculated using two different types of embedding functions.	114
<b>Table IX:</b>	Parameters determined for the expansion in Eq. (9) for various metals.	115
 <b>Paper 3</b>		
<b>Table I:</b>	Values of $\Delta G$ (in eV) for the low-index, bulk-terminated Ni surface layers.	149
<b>Table II:</b>	Predicted equilibrium values for selected diatomics; the binding energy ( $D_e$ ), the bond length ( $R_e$ ) and the vibrational frequency ( $\omega_e$ ).	150
<b>Table III:</b>	The surface energies (in $J/m^2$ ) for some unrelaxed low-index Ni, Cu, Rh, Pd and Ag surfaces. The % difference between the approximate methods and CEM is shown in parentheses.	151
<b>Table IV:</b>	Relaxation results for CEM, MD/MC-CEM and CEM-Pair for the (110) non-reconstructing fcc metal surfaces.	152
<b>Table V:</b>	Energies of formation calculated with CEM <sup>a</sup> , CEM-Pair and MD/MC-CEM <sup>a</sup> , in that order, $A_{0.5}B_{0.5}$ bulk alloys of selected combinations of Ni, Cu, Rh, Pd and Ag. The units are kJ/mol.	153

## ACKNOWLEDGMENTS

I gratefully acknowledge the helpful guidance of Professor Andrew E. DePristo throughout my graduate career. His patience and cheerful, persistent encouragement were instrumental in helping me achieve my goals.

This work was performed at Ames Laboratory under contract no. W-7405-eng-82 with the U.S. Department of Energy. The United States Government has assigned the DOE Report number IS-T 1649 to this thesis. This work was also supported in part by NSF grants CHE-8609832 and CHE-8921099 and by Procter & Gamble.

## GENERAL INTRODUCTION

In this work, various theoretical electronic structure techniques are used to analyze widely different systems from silicon clusters to transition metal solids and surfaces. All the theoretical techniques are in some fashion related to density functional theory (DFT).

For the silicon clusters, first principles self-consistent DFT methods are used to investigate  $\text{Si}_N$  for  $N=2-8$ . The goal is to understand the different types of bonding that can occur in geometries where the coordination of the atoms differs substantially from that of the stable bulk tetrahedral bonding. The analysis of the bonding reveals two limiting classes of silicon clusters. One of these is characterized by a large number of weak bonds, while the other has a small number of strong bonds. Such uncoordinated structures can provide a good test of more approximate theories that can eventually be used to model silicon surfaces.

For the transition metal systems, non-self-consistent electronic structure methods with DFT components are used to provide an understanding of the driving force for surface relaxations. An in-depth analysis of the results is presented and the physical basis of surface relaxation within the theory is discussed. In addition, the limitations inherent in calculations of metal surface relaxation and in the semi-empirical method itself are addressed.

Finally, in an effort to increase understanding of approximate electronic structure methods, a novel non-self-consistent method is developed that is about 1000 times faster computationally than more sophisticated methods. This new method is

tested for a variety of systems including diatomics, mixed metal systems and surfaces. The strengths and weaknesses of the new theory are discussed in detail, leading to greater understanding of non-self-consistent density functional theories as a whole.

### **An Explanation of the Dissertation Organization**

The main body of this dissertation consists of three papers, each of which covers a separate research topic. Two of these papers have been published in journals at this time; the third is suitable for publication. In papers 2 and 3, I have performed the majority of the calculations, analysis of data and the writing of the document, and am thus first author. In paper 1, the calculations were divided evenly between myself and Dr. Renè Fournier. The analysis of the data and the writing of the paper were divided such that Dr. Fournier performed a majority of the work, although I had many contributions. Hence, he is first author on this document. It should be noted that paper 1 represents a sizeable body of work, and my contributions to it are significant. This justifies its presence in the dissertation.

These papers are preceded by a literature review containing the necessary background information on DFT, the details of its applications in paper 1 and the derivation of the semi-empirical electronic structure method with DFT components used in papers 2 and 3. The papers are followed by a general summary. References cited in the general introduction and general summary follow the general summary.

### **Literature Review**

This literature review presents the background information referred to but not provided in the papers.

### ***Overview of Density Functional Theory***

DFT exploits the fact that ground states are often the quantity of interest in chemistry. The result of using the Variational Principle<sup>1</sup> is that the ground state energy of an electronic system is uniquely defined by its electron density, although the exact functional<sup>2</sup> dependence of the energy on density remains unknown. In DFT, the electronic density has replaced the electronic wavefunction as the important basic variable.

Consider an N-electron system with M nuclei and ignore relativistic effects<sup>3</sup>.

The total energy of the system is:

$$E_{\text{Total}} = E_{\text{nuc}} + E_{\text{el}} \quad (1)$$

The first term on the right hand side (RHS) is the total energy of the nuclear system, while the second term on the RHS is the total energy of the electronic system. The separation of purely electronic energy and purely nuclear energy is possible because of the Born-Oppenheimer approximation.

The nuclear interactions can be written as:

$$E_{\text{nuc}} = \sum_{\alpha < \beta}^M \frac{Z_{\alpha} Z_{\beta}}{|\vec{R}_{\alpha} - \vec{R}_{\beta}|} \quad (2)$$

where  $Z_{\alpha}$  and  $\vec{R}_{\alpha}$  are the atomic number and position in space, respectively of nucleus  $\alpha$ . This term is simple to calculate.

The electronic energy is significantly more difficult to calculate. It can be broken into four terms:

$$E_{\text{el}} = E_{\text{T}} + E_{\text{el-muc}} + E_{\text{coul}} + E_{\text{xc}} \quad (3)$$

The first of these is the kinetic energy of  $N$  noninteracting electrons with the same density as the actual set of interacting electrons:

$$E_{\text{T}} = -\frac{1}{2} \sum_{i=1}^N \int \psi_i(\vec{r}) \nabla^2 \psi_i(\vec{r}) d\vec{r} \quad (4)$$

where  $\psi_i$  are one-electron orbital wavefunctions. The second term is the electron-nucleus attraction:

$$E_{\text{el-muc}} = \sum_{\alpha=1}^M \int \frac{-Z_{\alpha}}{|\vec{r}-\vec{R}_{\alpha}|} n(\vec{r}) d\vec{r} \quad (5)$$

where  $\vec{r}$  is the position of the electron in space and  $n(\vec{r})$  is the electron density. The third term is the Coulomb interaction between two charge distributions:

$$E_{\text{coul}} = \frac{1}{2} \int \frac{n(\vec{r})n(\vec{r}')}{|\vec{r}-\vec{r}'|} d\vec{r}d\vec{r}'. \quad (6)$$

Finally, the fourth term,  $E_{\text{xc}}$ , is the exchange-correlation energy of the interacting system of electrons. This includes the kinetic energy difference between the interacting and non-interacting systems. Of all the terms on the RHS of Eq. (3), this is the only energy whose exact functional form is unknown.

The ground-state electron density is the density that satisfies<sup>1</sup>  $\delta E_{\text{el}}[n(\vec{r})]/\delta n(\vec{r})$  subject to the constraint  $\int n(\vec{r}) d\vec{r} = N$ . This gives

$$\left(-\frac{1}{2}\nabla^2 + \sum_{\alpha=1}^M \frac{-Z_{\alpha}}{|\vec{r}-\vec{R}_{\alpha}|} + \int \frac{n(\vec{r}')}{|\vec{r}-\vec{r}'|} d\vec{r}' + v_{xc}(n(\vec{r}))\right)\psi_i(\vec{r}) = \varepsilon_i\psi_i(\vec{r}) \quad (7)$$

where  $\varepsilon_i$  is the energy of the  $i$ 'th non-interacting electron,  $\psi_i$  is the one-electron orbital wavefunction seen in Eq. (4) and  $v_{xc}$  is the functional derivative of the exchange-correlation energy:

$$v_{xc}(n(\vec{r})) = \frac{\delta E_{xc}[n(\vec{r})]}{\delta n(\vec{r})} \quad (8)$$

The electron density is given by

$$n(\vec{r}) = \sum_{i=1}^N \psi_i(\vec{r})\psi_i(\vec{r}') \quad (9)$$

Eqs. (7)-(9) are known as the Kohn-Sham equations<sup>4</sup> and are exact. Up until now, no approximations have been made.

A well known and widely used approximation of  $E_{xc}$  is the Local Density Approximation (LDA). This assumes that the exchange-correlation energy for a nonuniform system can be evaluated by applying uniform-electron-gas results to infinitesimal portions of the nonuniform electron distribution and summing the individual contributions over all space.

The spin-generalized version of LDA is the Local Spin Density Approximation (LSDA). In the LSDA, the basis variables are  $n^+(\vec{r})$  and  $n^-(\vec{r})$  in addition to  $n(\vec{r})$ . In the LSDA the  $E_{xc}$  is approximated as follows:

$$E_{xc}[n^+(\vec{r}), n^-(\vec{r})] = \int n(\vec{r}) \epsilon_{xc}[n(\vec{r}), \zeta] d\vec{r} \quad (10)$$

where

$$\zeta = \frac{n^+(\vec{r}) - n^-(\vec{r})}{n^+(\vec{r}) + n^-(\vec{r})} \quad (11)$$

$\epsilon_{xc}[n(\vec{r}), \xi]$  is the exchange and correlation energy functional and includes the residual kinetic energy term per particle of an interacting homogeneous electron gas of density  $n(\vec{r})$ .  $\epsilon_{xc}[n(\vec{r}), \xi]$  can be divided into separate exchange and correlation contributions.

The exchange energy within the LSDA has the following analytic form:

$$\epsilon_x(n, \zeta) = \epsilon_x(n, 0) + [\epsilon_x(n, 1) - \epsilon_x(n, 0)]f(\zeta) \quad (12)$$

$$f(\zeta) = \frac{1}{2}(2^{1/3} - 1)^{-1} [(1 + \zeta)^{4/3} + (1 - \zeta)^{4/3} - 2] \quad (13)$$

where, in the Dirac implementation<sup>5</sup>,

$$\epsilon_x(n(\vec{r})) = -C_x n(\vec{r})^{1/3} \quad (14)$$

$$\begin{aligned} C_x &= \frac{3}{4} \left(\frac{3}{\pi}\right)^{1/3}, \zeta=0 \\ &= 2^{1/3} \frac{3}{4} \left(\frac{3}{\pi}\right)^{1/3}, \zeta=1 \end{aligned} \quad (15)$$

In contrast, the correlation energy is not known analytically and has been approximated different ways. The Gunnarsson-Lundqvist (GL) correlation functional<sup>6</sup> used in papers 2 and 3 assumes that the correlation energy has the same

analytic form as the exchange energy. Eqs. (12) and (13) are used in this implementation, replacing the "x" with a "c" and Eqs. (14) and (15) with the following expression:

$$\varepsilon_c^{\text{GL}}(r_s, \zeta) = -c(\zeta) \left[ (1+x^3(\zeta)) \ln \left( 1 + \frac{1}{x(\zeta)} \right) + \frac{1}{2} x(\zeta) - x^2(\zeta) - \frac{1}{3} \right] \quad (16)$$

$r_s$  is the radius of a sphere whose volume is the effective volume of an electron at a specific electron density (i.e.,  $n(\vec{r}) = 1 \text{ electron} / (4\pi r_s^3/3)$ ),  $x(\xi) = r_s/r(\xi)$ ,  $c(0)=0.0666$ ,  $c(1)=0.0406$ ,  $r(0)=11.4$  and  $r(1)=15.9$ .

Vosko, Wilk and Nusair (VWN)<sup>7</sup> have developed another form for the correlation energy that is used in paper 1 for the LSDA calculations.

$$\varepsilon_c^{\text{VWN}}(r_s, \zeta) = \varepsilon_c(r_s, 0) + \alpha(r_s) \left[ \frac{f(\zeta)}{f''(0)} \right] [1 + \beta(r_s) \zeta^4] \quad (17)$$

$\alpha(r_s)$  and  $\beta(r_s)$  are the spin stiffness constant and a fitting parameter respectively, and are provided in tables.  $\varepsilon_c(r_s)$  is given by the following expression:

$$\varepsilon_c(r_s) = \frac{A}{2} \left\{ \ln \frac{x}{X(x)} + \frac{2b}{Q} \tan^{-1} \frac{Q}{2x+b} - \frac{bx_0}{X(x_0)} \left[ \ln \frac{(x-x_0)^2}{X(x)} + \frac{2(b+2x_0)}{Q} \tan^{-1} \frac{Q}{2x+b} \right] \right\} \quad (18)$$

where  $x = \sqrt{r_s}$ ,  $X(x) = x^2 + bx + c$  and  $Q = \sqrt{4c - b^2}$ . When  $\xi=0$ ,  $A=0.0621814$ ,  $x_0=-0.409286$ ,  $b=13.0720$  and  $c=42.7198$ . When  $\xi=1$ ,  $A=0.0310907$ ,  $x_0=-0.743294$ ,  $b=20.1231$  and  $c=101.578$ .

In non-local density applications, which are more accurate than LSDA calculations, the gradients of the electron density is evaluated along with the density

functionals. The gradient of the density is a measure of the inhomogeneity of the density of finite systems. Paper 1 includes non-local calculations which use the Perdew-Wang gradient-corrected exchange-correlation energy functionals<sup>8</sup>. The exact forms of these functionals are not reproduced here due to their complicated form.

### ***Details of Implementing Density Functional Theory***

The first principles, self-consistent computational method used in paper 1<sup>9,10</sup> expands the one-electron molecular orbitals of Eqs. (4) and (7),  $\psi_i$ , in a linear combination of gaussian type orbitals (LCGTO):

$$\psi_i(\vec{r}) = \sum_j C_j \mu_j(\vec{r}) \quad (19)$$

Here  $\{\mu\}$  are the atom-centered gaussian-type orbitals, called the orbital basis, and  $\{C_j\}$  is the set of expansion coefficients.

The electron density  $n$  and exchange-correlation potentials,  $v_{xc}^\sigma$  (where  $\sigma = +$  or  $-$  spin) are also fit by LCGTO functions:

$$n_{\text{fit}}(\vec{r}) = \sum_i a_i f_i(\vec{r}) \quad (20)$$

$$v_{\text{xc,fit}}^\sigma(\vec{r}) = \sum_i b_i g_i(\vec{r}) \quad (21)$$

$\{f\}$  and  $\{g\}$  are termed the auxiliary basis.  $a_i$  is the set of coefficients which minimizes the error in the Coulomb repulsion energy subject to the constraint that  $\langle n_{\text{fit}} \rangle =$  the total number of electrons. They are obtained by least squares fitting.  $b_i^\sigma$  is the set of coefficients used to fit  $v_{xc}^\sigma$ ; they cannot be optimized analytically like the  $a_i$ , so the least squares fitting is performed over a set of grid points centered at

each atom. The error in the fitted potentials is also minimized with a weighted scheme. Implementing Eqs. (20) and (21) speeds up the calculations from  $N^4$  to  $N^2M$ , where  $N$  is the number of GTO's in the orbital basis and  $M$  is the total number of GTO's in the auxiliary basis (usually about the same as  $N$ ).

The program used in paper 1 makes use of frozen core electrons, called the model core potential (MCP) to further speed up the calculations. The core and valence orbitals are fit with an LCGTO expansion in a least-squares fitting procedure which minimizes the error relative to the numerical atomic calculation. A projection operator is used to ensure orthogonality of the frozen and valence orbitals.

### ***Derivation of the Corrected Effective Medium Theory***

Using the accurate DFT methods described above, it is a non-trivial, computationally intensive problem to determine the energy and forces for tens of atoms. This is especially true for atoms which have many valence electrons, such as the transition metals<sup>11</sup>. Therefore, methods known as "effective medium-type methods" have been developed specifically for systems containing many transition metals.

In the effective-medium type methods, the real  $M$ -atom system is replaced with many effective systems, each of which is the atom embedded in jellium (a homogeneous electron gas with a uniform compensating positive background). The energy of embedding the atom in jellium is termed the embedding energy. In addition to this energy, correction terms are calculated which take into account 1\ the difference in homogeneity between the electron density distributions in the real and many-atom systems; 2\ the difference between the uniform positive background

and nuclear point charges; and 3\ differences in the spin-polarization between the real system and the unpolarized atom-jellium system. There are many effective-type methods<sup>12-14</sup>, but the only one of interest here is the corrected effective medium (CEM) theory<sup>15-20</sup>.

The definition of the interaction energy is the energy difference between a system of interacting atoms and the system of non-interacting atoms.

$$\Delta E(\{A_i\}) = E(\sum_i A_i) - \sum_i E(A_i) \quad (22)$$

The embedding energy is defined as:

$$\Delta E_j(A_i; n_i) = E(A_i + n_i) - E(n_i) - E(A_i) \quad (23)$$

where the first term on the RHS is the energy of the atom-jellium system, and the second and third terms are the energy of the non-interacting jellium and atom systems respectively. Solving Eq. (23) for  $E(A_i)$  and substituting it into Eq. (22) gives:

$$\Delta E(\{A_i\}) = \sum_i \Delta E_j(A_i; n_i) + E(\sum_i A_i) - \sum_i [E(A_i + n_i) - E(n_i)] \quad (24)$$

The second and third terms on the RHS of Eq. (24) combine to form the correction energy. This can be split into two parts: the Coulomb correction energy and the kinetic-exchange-correlation correction energy.

$$\begin{aligned}
\Delta E(\{A_i\}) &= \sum_i \Delta E_f(A_i; n_i) + \\
&V_c(\sum_i A_i) - \sum_i [V_c(A_i + n_i) - V_c(n_i)] + \\
&G(\sum_i A_i) - \sum_i [G(A_i + n_i) - G(n_i)] \\
&= \sum_i \Delta E_f(A_i; n_i) + \Delta V_c + \Delta G(\{A_i\})
\end{aligned} \tag{25}$$

At this point CEM makes use of the superposition approximation to simplify the calculation. This states that the electron density at any point in space  $\vec{r}$  is the sum of the spin densities from each atom.

$$n^{\pm}(\vec{r}) = \sum_i n^{\pm}(A_i; \vec{r} - \vec{R}_i) \tag{26}$$

This additive density approximation holds for each atom in jellium, so the Coulomb interaction in the atom-jellium and jellium systems vanishes.

The explicit form of the kinetic-exchange-correlation energy functional is

$$G = \int [\tau(n^+(\vec{r})) + \tau(n^-(\vec{r})) + \epsilon_{xc}(n^+(\vec{r}), n^-(\vec{r}))] d\vec{r} \tag{27}$$

where  $\tau$  is the kinetic energy functional and  $\epsilon_{xc}$  is the exchange-correlation energy functional. The local Dirac and Gunnarsson-Lundqvist functionals are used for the exchange and correlation energy, respectively. For the kinetic energy, the following accurate Padé approximate representation of the full gradient expansion<sup>21</sup> is used.

$$\tau(n^{\pm}(\vec{r})) = \tau_0(n^{\pm}(\vec{r})) \frac{(1+0.95x+14.28111x^2-19.57962x^3+26.64777x^4)}{(1-0.05x+9.99802x^2+2.96085x^3)} \quad (28)$$

$$\tau_0(n^{\pm}(\vec{r})) = \frac{3}{10}(6\pi^2)^{2/3}n^{\pm}(\vec{r})^{5/3} \quad (29)$$

$$x = \frac{5}{108}(6\pi^2)^{-2/3} \frac{|\nabla n^{\pm}(\vec{r})|^2}{n^{\pm}(\vec{r})^{8/3}} \quad (30)$$

As  $x \rightarrow \infty$ , the kinetic energy functional becomes the Weizacker form:

$$\tau(n^{\pm}(\vec{r})) \xrightarrow{x \rightarrow \infty} \frac{|\nabla n^{\pm}(\vec{r})|}{8n^{\pm}(\vec{r})} \quad (31)$$

because the value of  $\nabla n/n^{4/3}$  becomes large. This overestimates the kinetic energy for small densities and large gradients, which will have the largest effect on weakly interacting systems.

At this point, only the jellium density remains to be determined. This was chosen so as to minimize the kinetic-exchange-correlation energy correction term,  $\Delta G$ , since it is calculated non-self-consistently and depends on the jellium density.

Because  $\Delta G$  is a complicated functional of the jellium density, an analytic minimization of  $\Delta G$  is not possible. The solution is to approximate the integrand in Eq. (27) with a quadratic in  $n^+$  and  $n^-$ .

$$\begin{aligned} \Delta G \approx & C \sum_i \sum_{j \neq i} \int \{n^+(A_i; \vec{r} - \vec{R}_i) n^+(A_j; \vec{r} - \vec{R}_j) + \\ & n^-(A_i; \vec{r} - \vec{R}_i) n^-(A_j; \vec{r} - \vec{R}_j)\} d\vec{r} - \\ & 2C \sum_i \int \{n^+(A_i; \vec{r} - \vec{R}_i) n_i^+ + n^-(A_i; \vec{r} - \vec{R}_i) n_i^-\} d\vec{r}_i \end{aligned} \quad (32)$$

C is the coefficient of the quadratic term,  $n^\pm(A_i; \vec{r} - \vec{R}_i)$  are the atomic spin densities (Hartree-Fock values were used) and  $n_i^\pm$  are the jellium densities. These are unpolarized, so  $n_i^+ = n_i^- = n_i/2$ . Thus, the jellium density can be factored out of the third term on the RHS of Eq. (32). This leaves the sum of atomic orbitals for the up and down spins, which is just the atomic number. Thus, Eq. (32) can be rewritten as:

$$\begin{aligned} \Delta G \approx & C \sum_i \sum_{j \neq i} \int \{n^+(A_i; \vec{r} - \vec{R}_i) n^+(A_j; \vec{r} - \vec{R}_j) + \\ & n^-(A_i; \vec{r} - \vec{R}_i) n^-(A_j; \vec{r} - \vec{R}_j)\} d\vec{r} - C \sum_i Z_i n_i \end{aligned} \quad (33)$$

The minimization of the absolute value of this quantity leads to solutions which are independent of the constant C. The most symmetric solution was chosen:

$$n_i = \frac{1}{Z_i} \sum_{j \neq i} \int \{n^+(A_i; \vec{r} - \vec{R}_i) n^+(A_j; \vec{r} - \vec{R}_j) + n^-(A_i; \vec{r} - \vec{R}_i) n^-(A_j; \vec{r} - \vec{R}_j)\} d\vec{r} \quad (34)$$

which can be written as follows for spin-unpolarized atoms:

$$n_i = \frac{1}{2Z_i} \sum_{j \neq i} \int n(\vec{r} - \vec{R}_i) n(\vec{r} - \vec{R}_j) d\vec{r} \quad (35)$$

Note that the original functionals are used to calculate  $\Delta G$ ; the quadratic approximation is only used to find the jellium density  $n_i$ .

PAPER 1. DENSITY FUNCTIONAL STUDY OF THE BONDING  
IN SMALL SILICON CLUSTERS

DENSITY FUNCTIONAL STUDY OF THE BONDING  
IN SMALL SILICON CLUSTERS

René Fournier,<sup>†</sup> Susan B. Sinnott and Andrew E. DePristo

Ames Laboratory - USDOE and

Department of Chemistry

Iowa State University

Ames, Iowa 50011

Printed in the

Journal of Chemical Physics **97**, 4149 (1992)

<sup>†</sup> Present address: Steacie Institute for Molecular Sciences, National Research Council, 100 Sussex Drive, Ottawa, Ontario, Canada, K1A 0R6.

**ABSTRACT**

We report the ground electronic state, equilibrium geometry, vibrational frequencies and binding energy for various isomers of  $\text{Si}_n$  ( $n=2-8$ ) obtained with the linear combination of atomic orbitals-density functional method. We used both a local density approximation approach and one with gradient corrections. Our local density approximation results concerning the relative stability of electronic states and isomers are in agreement with Hartree-Fock and Möller-Plesset (MP2) calculations [K. Raghavachari and C. M. Rohlfing, *J. Chem. Phys.* **89**, 2219 (1988)]. The binding energies calculated with the gradient corrected functional are in good agreement with experiment ( $\text{Si}_2$  and  $\text{Si}_3$ ) and with the best theoretical estimates. Our analysis of the bonding reveals two limiting modes of bonding and classes of silicon clusters. One class of clusters is characterized by relatively large s atomic populations and a large number of weak bonds while the other class of clusters is characterized by relatively small s atomic populations and a small number of strong bonds.

## INTRODUCTION

Small silicon clusters display a rich variety of structures. These structures are neither open (chains, rings), like those of small carbon clusters, nor fragments of the most stable bulk (diamond) silicon phase. Instead, the most stable  $\text{Si}_n$  clusters are usually compact but they are not always quasi-spherical and/or high-symmetry structures. For instance,  $\text{Si}_7$  is a pentagonal bipyramid but  $\text{Si}_4$  is a planar rhombus that is much more stable than the tetrahedral isomer of  $\text{Si}_4$ <sup>1-3</sup>. Many theoretical studies based on electronic structure calculations<sup>1-15</sup> have tackled the problems of: (1) predicting the relative stabilities of various  $\text{Si}_n$  isomers and (2) providing a detailed understanding of them.

In addition, a number of empirical models have been developed for use in the simulation of condensed phases of silicon.<sup>16-23</sup> These studies showed that it is very difficult, if at all possible, to devise a single classical potential that gives qualitatively correct descriptions of the bonding for vastly different arrangements of silicon atoms: crystalline phases, amorphous solids, defects, surfaces, liquids etc ... Typically, empirical models only do well at describing the selected properties and structures that are similar to those represented in the database used in adjusting the free parameters of the model. This kind of accuracy has been well exploited in the simulation of various processes: melting,<sup>16</sup> dimer reconstruction of the (100) face,<sup>17</sup> the modelling of amorphous silicon,<sup>24</sup> molecular beam epitaxy growth of the (100) surface,<sup>25,26</sup> keV bombardment of a silicon surface<sup>27</sup> and atom diffusion.<sup>28</sup>

Although devising empirical models for silicon clusters is even more difficult

than it is for surfaces and the bulk, a number of such models have been proposed recently.<sup>29-33</sup> A comparative study of  $\text{Si}_n$  ( $n=4-10$ ) with the first principles Car-Parinello method and with empirical models showed that the latter *"give only a poor description of the potential surface of the silicon microclusters"*.<sup>13</sup> A similar conclusion was reached more recently for  $\text{Si}_{13}$ .<sup>14</sup> Since many of the classical silicon potentials are derived originally from fits to accurate calculations for the bulk,<sup>34</sup> one expects that these potentials will become more appropriate for larger clusters. However, without a direct check with either experimental data or first principles calculations for clusters of "intermediate" size (roughly  $10 < n < 100$ ), it is difficult to know at what point these models start giving accurate results. In addition, these potentials may never describe surface atoms correctly since the bonding at the surface is so different from bonding in the bulk.

One of the most successful models is the very simple one proposed by Ackland.<sup>23,33</sup> This model is built with elements known from quantum chemistry: repulsion of ionic cores, tetravalency of silicon atoms, sum of bond energies, relative strength of single and double bonds and bond-bond repulsion. Further progress along these lines could be made by refining Ackland's model on the basis of a careful analysis of first principles electronic structure calculations. Such calculations can provide much more than just a database of structure and energy points for parameter fitting. They can provide insight into which effects should be included in an empirical model.

As a first step toward the making of an empirical model suitable for silicon bulk, surfaces and clusters, we have performed a series of Linear Combination of

Gaussian-Type Orbitals-Density Functional (LCGTO-DF) calculations on many silicon clusters with two to eight atoms. We have two objectives: (1) to provide a consistent set of equilibrium structures and binding energies (BE's) and (2) to provide a global picture of the different types of bonding that occur in small  $\text{Si}_n$  clusters with a rationale for the stabilities of the different structures. From the point of view of developing an empirical model, realization of the second objective provides a basis for constructing a qualitatively correct model while realization of the first gives a database for fitting adjustable parameters.

Of course, these two objectives have been addressed in earlier electronic structure studies, particularly the series of papers by Raghavachari and Rohlfiing (RR).<sup>1-5</sup> However, in the present work all structures were optimized within the Local Spin Density Approximation (LSDA), a method that includes correlation, whereas the optimization in earlier work was done at the Hartree-Fock (HF) level of theory for all except the smallest clusters ( $n \leq 4$ ). As it turns out, the accuracy of the binding energies of silicon clusters determined with the LSDA is comparable to that of the MP4 method of RR. The gradient corrected functional calculations of the present work are even more accurate and the BE's obtained in this way probably constitute the most reliable consistent set of BE's for silicon clusters. Regarding objective (2), our DF calculations also provide a simple one-electron picture of bonding. We will use simple concepts of atomic populations and bond orders to analyze the electronic structure in a way that we think relevant to the development of an empirical model.

A secondary goal of this work is to further assess the importance of gradient corrections to the exchange-correlation energy and to judge the accuracy of energy

differences calculated with these corrections. Previous work on this subject showed that the inclusion of gradient corrections greatly improves the accuracy of bond energies for a variety of systems: homonuclear diatomic molecules,<sup>35</sup> metal-ligand bonds,<sup>36</sup> a van der Waals molecule ( $\text{Mg}_2$ )<sup>37</sup> and organic molecules.<sup>38,39</sup> Recently Becke reported calculations with gradient corrections to the exchange energy for a set of 55 molecules with accurately known atomization energies.<sup>40</sup> In the present work we consider the issue of the accuracy of gradient corrected functional secondary, not because it is unimportant, but because it has already been fairly well tested and our results essentially confirm previous findings.

The rest of this paper is divided as follows. First, we give some technical details on the method used for the computations. Then the basic results (equilibrium geometries, electronic ground states, BE's and vibrational frequencies) are presented for each cluster size and compared to other theoretical studies. In the next section we show and discuss various non-empirical and empirical estimates of the BE's of silicon clusters taken from our own work and from that of RR. The implications regarding the abundance and stability of various clusters in molecular beams are briefly touched upon. The last section provides an analysis of the bonding in terms of atomic populations, hybridization and promotion energy, valency, bond lengths and bond orders.

## COMPUTATIONAL DETAILS

We used the density functional electronic structure program deMon developed by St-Amant and Salahub<sup>41</sup> that was briefly presented recently.<sup>42</sup> Gaussian atom-centered basis functions are used to expand the Kohn-Sham orbitals and to fit the associated density and exchange-correlation potential. The exchange-correlation energy is evaluated by numerical integration on a grid very similar to that of Becke<sup>43</sup> with a random orientation of each quasi-spherical shell of angular points as suggested by Jones et al.<sup>44</sup> The geometry optimization and evaluation of force constants was carried out using the LSD potential of Vosko, Wilk and Nusair (VWN),<sup>45</sup> evaluating the first energy derivatives analytically<sup>46</sup> and the second derivatives by numerical difference.<sup>47</sup> We then did calculations at the VWN-optimized geometries with the more accurate gradient-corrected functional of Perdew and Wang (PW).<sup>48</sup> The binding energies calculated that way will be denoted as "PW/VWN".

We did not treat the  $1s^2 2s^2 2p^6$  core of the silicon atoms explicitly, but used a model core potential instead. The valence orbital basis set consisted of three s functions, three shells of p functions and one shell of d functions, with the contraction pattern (311/211/1). The auxiliary bases for fitting the density and exchange-correlation potential both consisted of five s, three p and three d uncontracted gaussians. The full details on the model core potential and orbitals basis used can be found in the appendix of Ref. 49. The auxiliary bases used in the present work are similar to those reported in Ref. 49.

## RESULTS

The structures we investigated are plotted in Figs. 1-6. We denote the structures with three numbers  $n$ ,  $i$ , and  $j$ , and a letter  $l$ , as " $n.i.j.l$ ".  $n$  is the number of atoms in the cluster,  $i$  is the Hessian index (the number of imaginary frequencies) and  $j$  orders the structures with some  $n$  according to their BE, the most stable having  $j=1$ . The letter  $l$  denotes the spin multiplicity of the electronic state and, in this work, it can be either  $s$  (singlet) or  $t$  (triplet). For example, 4.0.2.t is the second most stable structure among four-atom clusters we investigated: it is a minimum on a triplet state potential surface. We supplement the structure name with point group symmetry label and/or descriptive comments when this information is helpful.

The essential results are in Tables I, II and III. In Table I we report the bond lengths in Angstroms and Mayer bond orders<sup>57</sup> and the BE's, calculated by the PW/VWN method, in eV. The BE's are calculated from the ground vibrational state, and thus include the zero point energies. The vibrational frequencies ( $\text{cm}^{-1}$ ) and zero point energy (ZPE) (kcal/mol) of all structures are listed in Table II. For completeness and easy reference we give the VWN and PW/VWN total energies (hartrees) in Table III.

The rest of this section is divided in seven subsections according to cluster size. Each provides some additional details and comments on the results reported in Tables I, II and III and a comparison to other theoretical studies and, when available, to experiment.

**Si<sub>2</sub>**

The two lowest electronic states, a  ${}^3\Sigma_g^-$  ( $R_e = 2.280 \text{ \AA}$ ) and a  ${}^3\Pi_u$  ( $R_e = 2.164 \text{ \AA}$ ) are almost equally stable. At the VWN level the  ${}^3\Pi_u$  is found to be more stable by only 0.01 eV. An earlier LCGTO-LSD study<sup>49</sup> also using the VWN potential predicted the  ${}^3\Pi_u$  to be *less* stable by 0.11 eV and found the equilibrium distance to be shorter by 0.01  $\text{\AA}$  for both states. This kind of discrepancy is not unexpected: deMon evaluates the exchange-correlation potential and energy more accurately than the program used in Ref. 49 because it uses a much better grid (more angular points, random orientation of shells, better grid point weights). The inclusion of gradient corrections reverse the order of stability and makes the  ${}^3\Sigma_g^-$  the more stable state, by 0.07 eV. The PW/VWN binding energy of Si<sub>2</sub> in its ground state is 3.62 eV, 0.41 eV larger than the experimental value of 3.21 eV.<sup>50</sup>

**Si<sub>3</sub>**

We looked at three structures: the equilateral triangle, the isosceles triangle and the linear structure, as shown in Fig. 1. The absolute minimum is the equilateral triangle in its triplet state, 3.0.1.t. The isosceles triangle (3.0.2.s) has a BE only 0.07 eV smaller than that of 3.0.1.t. This energy difference is too small for us to determine which structure is most stable. Improvements in the grid, basis sets and exchange-correlation functional could reverse the order. This very small energy difference is in line with other theoretical results. The other calculations predict the isosceles form to be slightly more stable, by 0.17 eV at most<sup>1,6,7</sup> except the LSD calculation of Dixon and Gole<sup>51</sup> which predicts 3.0.1.t to be more stable than 3.0.2.s by 0.07 eV. The BE of Si<sub>3</sub> is known experimentally to be  $7.6 \pm 0.2 \text{ eV}$ .<sup>52</sup> Our

calculated value (7.82 eV) is very close to this.

For 3.0.2.s we calculate an equilibrium angle of  $81.4^\circ$ . This is very close to the values found in Ref. 1, 6 and 7 which all fall in the range from  $78^\circ$  to  $81^\circ$  and also close to  $82.5^\circ$ , the value calculated by Dixon and Gole in their LSD study.<sup>51</sup> The bond lengths we calculate for the two structures (3.0.1.t: 2.273 Å, 3.0.2.s: 2.179 Å) are a little shorter than those calculated with the CAS-SCF method<sup>7</sup> (2.30 Å and 2.19 Å) and in agreement with the other LSD determination<sup>51</sup> (2.286 Å and 2.183 Å). The vibrational frequencies we calculate for 3.0.2 s (171, 540 and 548  $\text{cm}^{-1}$ ) are comparable to those found by Grev et al.<sup>6</sup> (157, 570 and 574  $\text{cm}^{-1}$ ) and by Raghavachari<sup>1</sup> (206, 560, 582  $\text{cm}^{-1}$ ). Our frequencies for both 3.0.1.t and 3.0.2.s agree with those of Dixon and Gole to within a few  $\text{cm}^{-1}$ . The level of agreement with this LSD study of  $\text{Si}_3$  is gratifying as it suggests that the numerical errors in both calculations (due to basis sets, grids, etc ...) are small.

There is also a triplet state with isosceles structure that is a minimum. It has an apex angle of  $123^\circ$  and a BE of 6.47 eV, 1.35 eV less than for the absolute minimum. The most stable linear structure has a singlet ground state and is 0.56 eV above the minimum. This is again in good agreement with the works of Raghavachari<sup>1</sup> and Balasubramanian<sup>7</sup> who find this energy difference to be 0.43 and 0.77 eV respectively.

## **$\text{Si}_4$**

Fig. 2 shows the structures that we considered. The most stable one is clearly the rhombus in a singlet state (4.0.1.s). The four equivalent bond lengths in 4.0.1 s are 2.316 Å and the shortest interatomic bridge distance is only 2.397 Å, suggesting

that these atoms are bonded. Indeed, the Mayer bond order for this pair of atoms is 1.03. All previous electronic structure calculations<sup>2,8-10,12</sup> similarly find that  $\text{Si}_4$  is a rhombus in a  ${}^1A_g$  state with bond lengths close to 2.3 and 2.4 Å. The vibrational frequencies we computed (55, 248, 348, 436, 464 and 495  $\text{cm}^{-1}$ ) differ substantially from those obtained by the HF method (137, 157, 328, 371, 425 and 472  $\text{cm}^{-1}$ ).<sup>2</sup> It has been pointed out that there are important correlation effects in the long bond.<sup>10</sup> That could be the reason the LSDA and HF frequencies differ so much.

Two other structures lie at approximately the same energy, roughly 0.7 eV higher than 4.0.1.s. One (4.0.2.t) is a triplet rhombus with four slightly shorter bonds (2.28 Å vs 2.32 Å) and a larger long bond (2.53 Å vs 2.40 Å). The other (4.0.3.t) is a distorted tetrahedron with  $C_{2v}$  symmetry in a triplet state. The  $C_{3v}$  trigonal pyramid (4.0.5.t) and the tetrahedron (4.0.7.s) are respectively 2.1 and 2.5 eV less stable than 4.0.1.s. The square structure (4.1.4.t) is a transition state and another triplet, the linear structure (4.2.6.t), has Hessian index of 2.

For  $\text{Si}_4$  we investigated all the structures considered by Raghavachari<sup>2</sup> except his structure 5. We find the same electronic ground states and Hessian index for all structures. We also agree on the relative stabilities but with two differences: (1) we find that the trigonal pyramid is 0.29 eV more stable than the tetrahedron, whereas Raghavachari found the tetrahedron to be the more stable of the two by 0.47 eV and (2) we find that the most stable triplet is the rhombus 4.0.2.t whereas Raghavachari apparently did not consider this structure in the triplet state and found that the most stable triplet was a distorted tetrahedron.

**Si<sub>5</sub>**

Of the five structures we considered, shown in Fig. 3, only two are minima. The trigonal bipyramid in its singlet state (5.0.1.s) is the absolute minimum, with a BE of 16.50 eV, and the planar C<sub>2v</sub> structure (5.0.2.s) lies 1.03 eV higher. The other high-symmetry structures we looked at are the square pyramid 5.1.3.s with BE=15.18 eV, the pentagon 5.4.4.t with BE=13.09 eV and the tetrahedron 5.3.5.s with BE=11.14 eV. Our predicted geometry for 5.0.1.s is somewhat different from the HF 6-31\* geometry of Ref. 2. The axial to equatorial interatomic distance we calculate is 2.304 Å, 0.034 Å shorter than that of Ref. 2 (2.338 Å). We get a smaller triangle (with sides equal to 2.98 Å compared to 3.26 Å) and a larger axial-axial distance (3.05 Å vs 2.78 Å).

**Si<sub>6</sub>**

The Si<sub>6</sub> geometries that were studied are shown in Fig. 4. We found three related low energy structures, a square bipyramid (6.2.3.s) and two distorted forms of it (6.0.1.s and 6.0.2.s), with singlet ground states that have BE's within 0.02 eV of each other. Considering the numerical uncertainty on our calculated energies, it is not possible to determine which structure is more stable. Moreover, the potential surface in the vicinity of these three structures is so flat (see the frequencies in Table II) that we cannot even be sure which structures are minima and which are higher order critical points. We note that two other DF studies<sup>9,11</sup> found 6.2.3.s as the most stable form of Si<sub>6</sub> but in both cases the authors do not report vibrational analysis and do not mention investigating structures 6.0.1.s and 6.0.2.s.

Using the HF 6-31G\* method, Raghavachari found similar results regarding

these three structures. He calculated the relative energies of 6.0.1.s, 6.0.2.s and 6.2.3.s to be 0, 0.04 eV and 0.39 eV and found their Hessian indices were 0, 1 and 2, respectively. These results are similar to ours but it is apparent that correlation stabilizes 6.2.3.s relative to the two other structures. The precise determination of BE's and vibrational frequencies for the most stable structures of  $\text{Si}_6$  presents a tough challenge for theory. Presently, methods that may be accurate enough to resolve this question are too time consuming to be applied to six-atom clusters. For now, we can only conclude from theory that there may be two, or even three, almost isoenergetic isomers of  $\text{Si}_6$  and that these have some very soft vibrational modes along which interconversion could occur.

The octahedral  $\text{Si}_6$  cluster (6.2.4.t) has a Hessian index of 2, a triplet ground state and is 0.7 eV less stable than the square bipyramid. The  $D_{2d}$  bicapped tetrahedron (6.2.5.s) is 1.6 eV less stable than structures 6.0.1.s and 6.0.2.s and has two imaginary frequencies.

## **$\text{Si}_7$**

For the seven- and eight-atom clusters, we examined only a few structures, the most likely candidates for the global minimum. For the most part, our results regarding the ground state electronic structure and the relative stability of various structures of  $\text{Si}_n$  ( $n=3-6$ ) are in line with those of Raghavachari.<sup>2</sup> There is no reason to think that this would change for larger clusters and there is no point in duplicating the extensive work of RR.<sup>1-5</sup> However, we want to compare BE's over a wider range of cluster size and provide more accurate estimates of the BE's of the most stable  $\text{Si}_n$  clusters.

The only three  $\text{Si}_7$  clusters we considered are the pentagonal bipyramid 7.0.1.s, the tricapped trigonal pyramid 7.0.2.s and a  $\text{C}_{2v}$  structure 7.2.3.s, all of which are shown in Fig. 5. The pentagonal bipyramid is the most stable with a BE of 24.91 eV. The two apex atoms have six neighbors and are therefore overcoordinated. Our value of  $d_{12}$  is 2.514 Å, 0.07 Å shorter than the HF/6-31G\* value of Ref. 3 and, contrary to Ref. 3, we find significant bonding of these atoms (bond order  $p_{12}=0.64$ ). This cluster is compact and quasi-spherical. These attributes (long bonds, high coordination, compact and nearly spherical structure) are usually associated with metal clusters and, in that sense,  $\text{Si}_7$  is peculiar. The energy of 7.0.2.s relative to 7.0.1.s is +0.60 eV (as compared to +0.95 eV found in ref. 3). The bond lengths we find for these two clusters are within 0.04 Å of those obtained by the HF method except for the longer bonds: our  $\text{Si}_1\text{-Si}_2$  interatomic distance in 7.0.1.s is 2.514 Å vs 2.582 Å and the  $\text{Si}_1\text{-Si}_5$  distance in 7.0.2.s is 2.602 Å vs 2.676 Å.

The geometry we find for 7.2.3.s is qualitatively different from that reported by Patterson and Messmer.<sup>10</sup> The bond lengths we calculate for the atom pairs (1,4), (6,7) and (1,7) are 0.54 Å, 0.26 Å and 0.21 Å shorter than those of Ref. 10. The bond orders for (6,7) and (1,7) are 1.44 and 1.05 respectively indicating strong bonding for these atom pairs whereas HF calculated bond lengths (2.50 Å) are typical of weak bonds.

### $\text{Si}_8$

Of the five eight-atom clusters we investigated, shown in Fig. 6, only 8.0.1.s is a minimum. This is the structure that Raghavachari and Rohlfiing<sup>3</sup> suggest as the global minimum of  $\text{Si}_8$ . The four other structures, all those considered by Patterson

and Messmer,<sup>10</sup> have values for the Hessian index of 1, 1, 2 and 4, respectively.

This illustrates the difficulty of finding minima (especially the global minimum) of moderately large clusters by trial and error and standard optimization algorithms and the importance of characterizing the critical points with a normal mode analysis, which was not done in Ref. 10.

The relative stability of the four Si<sub>8</sub> structures 8.1.2.s, 8.1.3.s, 8.2.4.s and 8.4.5.s calculated by PW/VWN differ significantly from that found by Patterson and Messmer<sup>10</sup> in their HF study and differ also from their Generalized Valence Bond BE's calculated at HF optimized geometries (GVB/HF) as shown below:

Relative stability (eV)

cluster:	8.1.2.s	8.1.3.s	8.2.4.s	8.4.5.s
PW/VWN	0.0	0.43	1.85	2.51
HF <sup>10</sup>	0.0	2.48	1.92	1.20
GVB/HF <sup>10</sup>	0.16	----	----	0.0

Taking PW/VWN values as the reference, we see that the HF relative energy for 8.1.3.s is in error by about 2.0 eV and the GVB/HF relative energy of 8.4.5.s is in error by about 2.5 eV. This shows that there is a real danger of underestimating the stability of a given cluster size when structures are optimized with the HF method and a more accurate (correlated) method is used subsequently only to calculate the energy of the most stable structure.

## TRENDS IN BINDING ENERGIES

The experimentally known BE's for  $\text{Si}_n$  are for  $\text{Si}_2$ ,  $\text{BE}=3.21$  eV,<sup>50</sup> and  $\text{Si}_3$ ,  $\text{BE}=7.6\pm 0.2$  eV.<sup>52</sup> (An earlier estimate of BE for  $\text{Si}_3$  is  $7.3\pm 0.5$  eV<sup>53</sup> but we assume that  $7.6\pm 0.2$  eV is the most accurate value). Our calculated BE's for these two clusters are 3.94 and 8.83 eV by the VWN method (errors: +0.73 and  $+1.2\pm 0.2$  eV) and 3.62 and 7.82 eV by the PW/VWN method (errors: +0.41 and  $+0.2\pm 0.2$  eV). As usual the BE's are overestimated at the LSDA level and the gradient corrections bring the values closer to experiment. The BE's calculated by MP4/6-31G<sup>\*2,3</sup> for  $\text{Si}_2$  and  $\text{Si}_3$  are 2.60 and 6.34 eV (errors: -0.64 and  $-1.4\pm 0.2$  eV). On that basis, the VWN BE's seem as accurate as those calculated by MP4 and the BE's calculated by PW/VWN are more accurate than both VWN and MP4. Moreover, empirically corrected MP4 and VWN BE's are closer to the PW/VWN values than to the unaltered MP4 and VWN BE's. This gives further support to the PW/VWN BE's (and also to the empirical corrections). We will now consider these empirical corrections to MP4 and VWN BE's.

Raghavachari proposed to estimate the true BE's of silicon clusters by scaling the BE's calculated with the MP4 method according to the following relation.

$$\text{BE}(\text{Si}_n; \text{corrected MP4}) = 1.2 \cdot \text{BE}(\text{Si}_n; \text{MP4})$$

With this scaling, the two experimental values are reproduced very well (3.12 vs 3.21 and 7.61 vs  $7.6\pm 0.2$ ). Moreover, this scaling increases all MP4 BE's which are generally expected to be lower limits to true BE's. RR applied this scaling to obtain their most accurate estimates to the  $\text{Si}_n$  clusters BE's. We looked for a similar

correction to VWN BE's, which are expected to almost always overestimate true BE's, and found two "reasonable" ways of correcting.

We can reproduce the experimental results almost exactly by correcting the energy of the isolated silicon atom by the empirical value -0.38 eV. This yields correction #1, expressed as:

$$\text{BE}(\text{Si}_n; \text{correction \#1; VWN}) = \text{BE}(\text{Si}_n; \text{VWN}) - n \cdot -0.38 \text{ eV}$$

This is fundamentally different from the scaling used in MP4. The correction to MP4 is based on the intuitive knowledge that lack of correlation in the clusters' wavefunctions leads to a systematic underestimate of the bonding interactions. Assuming that this underestimate is a fixed fraction of the interactions leads to the MP4 scaling relation. The VWN correction is based on the assumption that the clusters at their equilibrium geometry are very well described and that all the error is due to a poor description of the isolated atom. This is rationalized by noting that silicon atoms have more compact orbitals than clusters. This gives rise to a larger self-interaction error for N separated atoms than for a N-atom cluster.

A slight modification to correction #1 is obtained if we assume that unpaired electrons are atomic-like in that they produce self-interaction errors that are as large as those of atomic orbitals. Then, the size of the correction is proportional to  $(4n-m)$ , where  $m$  is the number of unpaired electrons in the cluster and the factor 4 is there because silicon atoms have four valence electrons. The proportionality factor that best fits the experimental results is 0.123, giving us the following expression:

$$\text{BE}(\text{Si}_n; \text{correction \#2 VWN}) = \text{BE}(\text{Si}_n; \text{VWN}) - (4n-m) \cdot -0.123 \text{ eV}$$

Both corrections #1 and #2 are probably best viewed as rough approximations to the

self-interaction corrections<sup>58</sup> of the local density approximation.

Of course, reproducing two known values using an empirical method with one adjustable parameter is not a great accomplishment. But there is more evidence in support of these corrections. First, the two sets of BE's, "corrected MP4" and "correction #1 VWN", are nearly equivalent. Either they are both very close to the true values or, somehow, they deviate in nearly the same way from these. But the MP4 and VWN methods come from *seemingly* quite different approaches to electronic structure and, as we noted above, the corrections are fundamentally different. Second, there is convincing evidence from the theory and the practice of gradient corrections that PW/VWN BE's are almost always much more accurate than VWN BE's. Therefore, the better agreement of these two sets of corrected BE's with the PW/VWN BE's than with uncorrected BE's constitute further support in favor of the corrections. Correction #2 gives BE's that are even closer to those calculated by PW/VWN.

In Table IV we list the BE's of the global minima for each cluster size calculated with six different methods: MP4, VWN, scaled MP4, corrected VWN (#1 and #2) and PW/VWN. The experimental and PW/VWN BE's are always bracketed by MP4 and VWN BE's. The scaled MP4 and corrected VWN (#1) BE's are within 0.25 eV of each other, except for Si<sub>5</sub> and Si<sub>7</sub> for which the differences are 0.47 and 0.44 eV respectively. The agreement for these clusters could improve if the MP4-optimized geometry differed substantially from that optimized by HF. For these two sets of BE's, the differences between the estimates of the cohesive energy, *in eV/atom*, are: 0.03, 0.03, 0.05, 0.09, 0.01, 0.06 and 0.03. The corrected MP4 and

correction #1 VWN cohesive energies are not too far from those calculated by PW/VWN and the correction #2 VWN is still closer to PW/VWN. The difference in cohesive energy between corrected VWN and PW/VWN increases smoothly with increasing  $n$  for the global minima:

$n$	BE(correction #1 VWN)/ $n$ -BE(PW/VWN)/ $n$ (eV/atom)	BE(correction #2 VWN)/ $n$ -BE(PW/VWN)/ $n$ (eV/atom)
2	-0.20	-0.21
3	-0.04	-0.07
4	+0.03	-0.08
5	+0.09	-0.02
6	+0.14	+0.03
7	+0.18	+0.07
8	+0.18	+0.06

The same trends in the various computed BE's are found for the local minima as well.

We will now exclusively discuss the PW/VWN BE's, which we take as the best estimates because they are not empirical and agree well with the available experimental data.

Fig. 7a shows the energy  $D_n$  required for the disproportionation reaction as a function of  $n$ :



This gives a sensitive measure of relative stability.  $\text{Si}_4$  and  $\text{Si}_7$  are especially stable toward disproportionation. Another measure of cluster stability is given by the incremental binding energy  $\Delta\text{BE}_n$ , defined as:

$$\Delta\text{BE}_n = \text{BE}(\text{Si}_n) - \text{BE}(\text{Si}_{n-1})$$

This is plotted in Fig. 7b. This also characterizes  $\text{Si}_4$  as especially stable. The limit

for large  $n$  of  $\Delta BE_n$  is the bulk cohesive energy, 4.63 eV/atom.<sup>56</sup> The curve in Fig. 7b shows that silicon clusters with  $n \leq 8$  are still far from this limit.

This brings us to an important point. RR invoked the relatively high values of  $\Delta BE_n$  for  $n = 4, 6, 7$  and 10 as evidence that these are "magic numbers" for silicon clusters. Indeed, mass spectrometry revealed large quantities of six-, seven- and ten-atom silicon clusters<sup>54,55</sup> and photofragmentation cross sections are relatively small for four-, six- and ten-atom clusters.<sup>54</sup> However  $Si_6$  is not really more stable than  $Si_5$  according to our PW/VWN calculated  $D_n$  and  $\Delta BE_n$ . Our results suggest an alternative explanation to the large quantities of six-atom clusters detected by mass spectrometry. It could be due to the presence of two stable isomers and/or to a high density of vibrational states and correspondingly large vibrational partition function resulting from the flatness of the potential surface (see the frequencies in Table II).

## BONDING IN SILICON CLUSTERS

Our discussion of bonding will be based on atomic charges ( $q_i$ ) and s, p and d populations ( $ns_i$ ,  $np_i$  and  $nd_i$ ) obtained by Mulliken analysis, atomic valency ( $V$ ) calculated in the way proposed by Mayer,<sup>53</sup> interatomic bond lengths ( $d_{ij}$ ) and Mayer bond orders ( $p_{ij}$ ). The populations and bond orders calculated with VWN and PW potentials were always very similar. We report only those calculated with the VWN potential.

One could expect all  $q_i$ 's and  $nd_i$ 's to be nearly zero. Assuming these *are* zero, each atom  $i$  would have a s population of  $ns_i$  and a p population  $np_i$  equal to  $4.0 - ns_i$ . The magnitude of the atomic charges were indeed small, usually smaller than 0.05 and all smaller than 0.15 except one. The largest values of  $|q_i|$  and  $nd_i$  are those of the central atom of 5.3.5.s,  $q = -0.27$  and  $nd_i = 0.30$ . Typically, d atomic populations are in the range of 0.05 to 0.20.

Assuming that all  $q_i$ 's and  $nd_i$ 's are zero is an oversimplification, but still useful in looking for trends. Using this assumption, values of  $ns_i$  are expected to range from 2.0 ( $s^2p^2$  hybridized atoms) to 1.0 ( $sp^3$  hybridized atoms). Actually,  $ns_i$  ranges from 2.02, the value for the end atoms of 4.2.6.t, to 1.28, the value for the central atom of 5.3.5.s. We used the central atom of the tetrahedral molecule  $\text{Si}(\text{SiH}_3)_4$  as a model for a silicon atom in bulk diamond Si. The s, p and d populations of this atom are 1.38, 2.80 and 0.06 and the charge is -0.24. The average over the five silicon atoms of  $\text{Si}(\text{SiH}_3)_4$  are  $ns = 1.40$ ,  $np = 2.50$ ,  $nd = 0.03$  and  $q = +0.05$ . This is far from the ideal  $sp^3$  hybridization. Essentially similar results were

obtained by RR.<sup>3</sup>

In the simplest picture of hybridization, a single number would be sufficient to characterize the hybridized state of a silicon atom. We choose this number to be  $2-n_{s_i}$ , the number of electrons promoted from s to p atomic orbitals. Intuitively, one expects a correlation between  $2-n_{s_i}$  and the number of bonds in which an atom  $i$  takes part. More precisely, assuming that each unpaired electron of an atom is involved in a covalent bond, and taking the Mayer valency  $V$  as a measure of the number of bonds into which an atom participates, one expects  $V=2+2(2-n_{s_i})$ . A plot of  $V$  as a function of  $2-n_{s_i}$  for the 62 distinct silicon atoms in the set of clusters we studied (Fig. 8) indeed shows a linear relationship. Also, the straight line that best fits the dataset has a slope of 2.0 as expected. The intercept however is 2.65 instead of 2.0.

The two basic attributes of a bond between atoms  $i$  and  $j$  in our analysis are the bond length  $d_{ij}$  and bond order  $p_{ij}$ . These are given in Table I. Fig. 9 is a plot of  $p$  as a function of  $d$  for all bonds shorter than 3.0 Å but excluding the bond in  $\text{Si}_2$ . The smooth line is a polynomial fit to a subset of the data points and is there only to guide the eye. There is a rough correlation between  $d$  and  $p$ . Some points break away from the rest. These interesting bonds will be discussed below but we first comment on the general features of Fig. 9.

The data points almost all fall into two regions of the  $d$ - $p$  plane and the bonds can be classified accordingly. There are short strong bonds with  $d < 2.35$  Å and  $p > 0.85$  and long weak bonds with  $d > 2.35$  and  $p < 0.85$ . In the short bond region  $p$  decreases rapidly with increasing  $d$  whereas in the long bond region  $p$  decreases

slowly and reaches a near constant value with increasing  $d$ . The breakup of the data points in two classes corresponds roughly to two modes of bonding in silicon clusters: directional covalent bonds, for which one expects  $p \geq 1.0$ , and non-directional and/or delocalized bonds typical of metallic systems.

The bonds with exceptionally large bond orders at  $d=2.40 \text{ \AA}$  and  $d=2.53 \text{ \AA}$  are those connecting atoms 1 and 2 in the rhombus structures 4.0.1.s and 4.0.2.t respectively. The strain in the 1,3,2 and 1,4,2 angles prevents atoms 1 and 2 from attaining their ideal covalently bonded distance (roughly  $2.3 \text{ \AA}$ ). The other bond with unusually large bond order,  $d=2.84 \text{ \AA}$ , is the bond connecting atoms 2 and 3 in cluster 3.0.2.s. The rationalization here is that these atoms have extremely low coordination and high propensity to bind. But again, the repulsion between the 1,2 and 1,3 bonds associated with closing the 2,1,3 angle opposes the decrease of  $d_{23}$ .

One of the most interesting features of small silicon clusters is that they display characteristics of both metallic and covalent materials. We will define three quantities that can help assess the metallic vs covalent nature of clusters. The first is a measure of the promotion energy cost (calculated from  $s$  atomic populations) relative to the binding energy. This should be smallest for metallic silicon and largest for covalent silicon. The second quantity we will use is the average coordination of atoms in the cluster. Roughly speaking, this should be at most 4.0 for covalent clusters since silicon atoms have four valence electrons. For metallic silicon, the average coordination can be larger than 4.0 (for fcc bulk silicon it is about 12.0). The third and most important quantity is the HOMO-LUMO gap. This is the cluster equivalent of the band gap of extended systems. Metallic clusters should

exhibit small gaps, covalent clusters large gaps. The variation in the gaps among the different clusters is fairly potential-independent. We therefore only report the HOMO-LUMO gaps found with the VWN potential. We will now define more precisely these quantities and use them to evaluate the nature of the clusters.

We calculated the  $s^2p^2$  to  $sp^3$  excitation energy for an isolated silicon atom by taking the difference in the total energies from PW/VWN calculations and found it to be 4.07 eV. We define the promotion energy of an atom  $i$  in a cluster as this energy difference (4.07 eV) multiplied by  $2-n_{s_i}$ . By summing over all atoms of a cluster we calculated a total promotion energy. We further define the "intrinsic" binding energy (IBE) of a cluster as the sum of the binding energy calculated with respect to ground state silicon atoms and of the total promotion energy,  $IBE=BE+PE$ . The PE is a rough equivalent of the energy, measured relative to  $n$  ground state atoms, of a system of  $n$  separated atoms in excited states that correlates with the ground state of the cluster. The IBE is the BE of the cluster measured relative to this  $n$  separated excited atoms system. The values of BE, PE and IBE derived from PW/VWN calculations and the ratio PE/IBE are given in Table V. The main points are that the values of PE are not small (they are about 20% of the IBE's) and they are not nearly constant for a given cluster size. The ranges covered by PE's for the clusters we studied are 0.37, 2.93, 1.89, 1.42, 1.44 and 2.85 eV for  $n=3$  to 8.

The ratio PE/IBE can be used to classify clusters. Large values of this ratio should be typical for covalently bonded systems in which the hybridization of atoms tends toward  $sp^3$ . Low values of PE/IBE are expected for metallic-like clusters in which atoms are overcoordinated, bonds are rather long and the stabilization

associated with strong  $sp^3$ - $sp^3$  bonds is offset by the promotion energy cost. With few exceptions, the more open structures show the largest values of PE/IBE. Linear and cyclic structures (2.0.1.t, 3.2.3.s, 4.0.2.t, 4.2.6.t, 5.4.4.t) have an average PE/IBE value of 0.27 whereas the more compact, nearly spherical "metallic" clusters (4.0.5.t, 4.0.7.s, 6.0.1.s, 6.0.2.s, 6.2.3.s, 7.0.1.s, 8.2.4.s) have an average PE/IBE of 0.19.

Empirical models proposed so far have failed to predict accurately energy differences in systems having silicon atoms with low coordination. Modelling the hybridization state of atoms and the IBE's may be a fruitful approach to the description, in a single model, of systems with low coordinated Si atoms and systems with highly coordinated Si atoms.

The second measure of the covalent/metallic character of clusters we propose is based on the picture that covalent clusters have a small number of strong bonds while metallic clusters have a large number of weak bonds. We define  $x_i$ , the coordination of atom  $i$ , as the ratio of the square of the sum of bond orders and the sum of the squares of the bond orders involving atom  $i$ :

$$x_i = \frac{(\sum_j p_{ij})^2}{\sum_j p_{ij}^2}$$

One expects  $x_i$  to be slightly larger than 4.0 (because of some delocalization) for atoms in diamond silicon, the prototypical covalent silicon system. As shown in Table VI,  $x_i$  is 4.32 for the central atom of  $\text{Si}(\text{SiH}_3)_4$ . We arbitrarily choose this value as the frontier between "metallic" and "covalent" silicon atoms. To classify

clusters, we simply take  $\langle x \rangle$ , the average of the  $x_i$ 's over all atoms  $i$  of a cluster, as the measure of the metallic character.

Clearly,  $\langle x \rangle$  cannot be larger than 4.0 for silicon clusters with less than 6 atoms and therefore all these clusters are regarded as "covalent". The situation is more interesting for 6-, 7- and 8-atom (and larger) clusters. Among these larger clusters, we found only three covalent-like clusters and none of these is a minimum. The three covalent-like clusters are rather open structures and their PE/IBE ratios (0.23, 0.29 and 0.27) are large. Contrary to RR, we find that many atoms have coordination larger than 5. For instance,  $x_i$  is 6.0 for the axial atoms in 7.0.1.s and the central atom of 7.0.2.s. Our definition of coordination is unlike that used by RR but we think that the difference is due mostly to the type of calculation. More precisely, we believe that methods with no or little correlation, the HF method in particular, do not describe accurately overcoordination of atoms.

The quantities PE/IBE and  $\langle x \rangle$  give a consistent classification, provided that comparisons are made within a given cluster size for clusters with less than six atoms. With few exceptions,  $\langle x \rangle$  is largest for those clusters that have the smallest PE/IBE. We stress that  $V_i$  and  $x_i$  give very different and complementary information on the coordination of an atom  $i$ . For singlet states  $V_i$  is exactly the sum of all bond orders related to a given atom  $i$  whereas  $x_i$  is calculated as shown above. Note that  $V_i$  and  $\langle x \rangle$  (or  $x_i$ ) follow opposite trends with respect to  $s$  atomic populations.

Curiously the HOMO-LUMO gap seem to follow a trend opposite to what is expected from the values of PE/IBE and  $\langle x \rangle$ . The clusters classified as "metallic" with respect to  $\langle x \rangle$  and PE/IBE typically have larger gaps than "covalent-like"

clusters. In fact, the gap correlates better with the binding energy. The most stable clusters of 5, 6, 7 and 8 atoms are also those that have the largest HOMO-LUMO gap in their size category. Therefore, metallic and covalent characteristics coexist not only for different silicon clusters, but, in general, within a given cluster. Silicon clusters having all the properties of a metal, or all those of a semiconductor, presumably exist only at much larger cluster size. The HOMO-LUMO gaps calculated for the most stable cluster isomers range from 1.05 eV (for 4.0.1.s) to 2.12 eV (for 7.0.1.s) and are therefore all larger than the LSD value for bulk diamond silicon, 0.5 eV<sup>59</sup> (which is an underestimate of the experimental band gap of 1.17 eV for diamond silicon).<sup>60</sup>

## CONCLUDING REMARKS

To a large extent our results concerning the structure and ground electronic state of the most stable silicon clusters and the relative stability of isomers and of different-size clusters agree with those of RR.<sup>1-5</sup> One significant difference is seen for the six-atom cluster for which we do not find an unusually large BE. However,  $\text{Si}_6$  is unique because it may have two nearly isoenergetic isomers and some of the calculated vibrational frequencies are extremely small. These features imply a large value of the vibrational partition function and a large entropic factor favoring  $\text{Si}_6$  formation. This may be why some experiments on silicon clusters characterize  $\text{Si}_6$  as a "magic number" cluster.

We tried to divide the silicon clusters into two classes: "metallic" and "covalent". Three criteria were used for this classification: the size of the promotion energy relative to the intrinsic binding energy; the average coordination number; and, the HOMO-LUMO gap. Most clusters have characteristics of both metals and semiconductors. The most stable six-, seven- and eight-atom clusters are metallic-like in that their atoms have coordination numbers well above 4.0 and are in hybridization states closer to  $s^2p^2$  than to the hybridization of the central atom of  $\text{Si}(\text{SiH}_3)_4$ . These clusters are covalent-like in that they have a large HOMO-LUMO gap. True metallic and semiconductor properties probably develop only for much larger clusters than those considered here.

The BE's calculated from MP4 and VWN methods are quite different, but simple corrections bring them into almost perfect agreement with experiment and

with each other. Yet, the two methods are essentially different, as are the nature of the corrections. The correction to MP4 assumes that a fixed fraction of the binding energy is missing due to incomplete correlation. The correction to VWN assumes that the error in BE's arises from an improper treatment of the atom (and, for correction #2, of unpaired electrons). Given the dissimilitude of the two computational methods and the level of agreement, these corrected BE's probably constitute good estimates of the true BE's. Further evidence for this is the good agreement with a third set of BE's, those calculated with the PW/VWN method. Actually, we favor this last set of BE's since they result from a truly first-principles method and yet the values agree with the two experimentally known BE's.

The calculated structures and PW/VWN BE's presented in this paper can be used as a database in constructing empirical models or classical potentials for use in molecular dynamics. Moreover, we presented bond orders and atomic populations that may help further.

One important feature is that the hybridization of silicon atoms varies significantly from case to case. We think that this *must* be included in some way in a model for it to be applicable to the diverse bonding situations occurring in clusters, on surfaces and in the bulk. A promising approach would be to model the hybridization state of atoms and fit our calculated promotion energies (PE) and intrinsic binding energies (IBE) separately. A classical potential constructed with this approach must include a sum of atomic terms (the atomic promotion energies).

**NOTE ADDED IN PROOF**

After submission of our paper a Gaussian-2 (G2) study reporting BE's for the most stable isomers of  $\text{Si}_n$  ( $n=2-5$ ) was published.<sup>61</sup> The four calculated BE's (3.19, 7.41, 11.95 and 16.15) are smaller than our PW/VWN values by a near constant amount. The G2 BE's are essentially perfect agreement with experiment for  $n=2,3$  and probably constitute the best theoretical estimates for  $n=4,5$ . The agreement in the absolute and, especially, in the relative BE's between the G2 and PW/VWN methods is excellent. This is a good indication that the relative values of the PW/VWN BE's of the 30 cluster structures reported here are highly accurate.

## ACKNOWLEDGEMENTS

This work was supported by the Division of Chemical Sciences, Office of Basic Energy Sciences of the U.S. Department of Energy through the Ames Laboratory, which is operated for the U.S. DOE by Iowa State University under Contract No. W-7405-Eng-82. The calculations were performed on a SiliconGraphics 4D/380S computer purchased by an NSF instrumentation grant. We thank Prof. D. R. Salahub and Dr. A. St-Amant for giving us access to their density functional program deMon. R.F. would like to express his gratitude to the National Science and Engineering Research Council of Canada for a postdoctoral fellowship.

## REFERENCES

1. K. Raghavachari, *J. Chem. Phys.* **83**, 3520 (1985).
2. K. Raghavachari, *J. Chem. Phys.* **84**, 5672 (1986).
3. K. Raghavachari and C. M. Rohlfing, *J. Chem. Phys.* **89**, 2219 (1988).
4. C. M. Rohlfing and K. Raghavachari, *Chem. Phys. Lett.* **167**, 559 (1990).
5. K. Raghavachari and C. M. Rohlfing, *J. Chem. Phys.* **94**, 3670 (1991).
6. R. S. Grev and H. F. Schaefer III, *Chem. Phys. Lett.* **119**, 111 (1985).
7. K. Balasubramanian, *Chem. Phys. Lett.* **125**, 400 (1986).
8. K. Balasubramanian, *Chem. Phys. Lett.* **135**, 283 (1987).
9. D. Tomanek and M. A. Schluter, *Phys. Rev. B* **36**, 1208 (1987).
10. C. H. Patterson and R. P. Messmer, *Phys. Rev. B* **42**, 7530 (1990).
11. O. F. Sankey, D. J. Niklewski, D. A. Drabold, and J. D. Daw, *Phys. Rev. B* **41**, 12750 (1990).
12. G. Pacchioni and J. Koutecky, *J. Chem. Phys.* **84**, 3301 (1986).
13. W. Andreoni and G. Pastore, *Phys. Rev. B* **41**, 10243 (1990).
14. U. Röthlisberger, W. Andreoni, and P. Giannozzi, *J. Chem. Phys.* **96**, 1248 (1992).
15. G. H. F. Dierksen, N. E. Gruner, J. Oddershede, and J. R. Sabin, *Chem. Phys. Lett.* **117**, 29 (1985).
16. F. H. Stillinger and T. A. Weber, *Phys. Rev. B* **31**, 5262 (1985).
17. D. W. Brenner and B. J. Garrison, *Phys. Rev. B* **34**, 1304 (1986).
18. J. Tersoff, *Phys. Rev. Lett.* **56**, 632 (1986); *ibid* *Phys. Rev. B* **37**, 6991 (1988); *ibid*

- Phys. Rev. B **38**, 9902 (1988).
19. R. Biswas and D. R. Hamann, Phys. Rev. B **36**, 6434 (1987).
  20. B. W. Dodson, Phys. Rev. B **35**, 2795 (1987).
  21. E. R. Cowley, Phys. Rev. Lett. **60**, 2379 (1988).
  22. M. I. Baskes, J. S. Nelson, and A. F. Wright, Phys. Rev. B **40**, 6085 (1989).
  23. G. Ackland, Phys. Rev. B **40**, 10353 (1989).
  24. M. D. Kluge, J. R. Ray, and A. Rahman, Phys. Rev. B **36**, 4234 (1987).
  25. E. T. Gawlinski and J. D. Guntar, Phys. Rev. B **36**, 4774 (1987).
  26. B. J. Garrison, M. T. Miller, and D. W. Brenner, Chem. Phys. Lett. **146**, 553 (1988); D. W. Brenner and B. J. Garrison, Surf. Sci. **198**, 151 (1988); D. Srivastava, B. J. Garrison, and D. W. Brenner, Phys. Rev. Lett. **63**, 302 (1989).
  27. R. Smith, D. E. Harrison Jr., and B. J. Garrison, Phys. Rev. B **40**, 93 (1989).
  28. P. M. Agrawal, D. L. Thompson, and L. M. Raff, J. Chem. Phys. **91**, 6463 (1989).
  29. A. D. Mistriotis, N. Flytzanis, and S. C. Farantos, Phys. Rev. B **39**, 1212 (1989).
  30. B. C. Bolding and H. C. Andersen, Phys. Rev. B **41**, 10568 (1989).
  31. J. R. Chelikowsky, J. C. Phillips, M. Kamal, and M. Strauss, Phys. Rev. Lett. **62**, 292 (1989); J. R. Chelikowsky and J. C. Phillips, Phys. Rev. Lett. **63**, 1653 (1989); *ibid* Phys. Rev. B **41**, 5735 (1990).
  32. J. R. Chelikowsky, K. M. Glassford, and J. C. Phillips, Phys. Rev. B **44**, 1538 (1991).
  33. G. J. Ackland, Phys. Rev. B **44**, 3900 (1991).
  34. M. T. Yin and M. L. Cohen, Phys. Rev. B **26**, 5668 (1982); K. J. Chang and M. L. Cohen, *ibid.* **31**, 7819 (1985).

35. A. D. Becke, in *The Challenge of d and f Electrons*, D. R. Salahub and M. C. Zerner Eds, ACS Symp. Ser. **394** (1989); A. D. Becke, *J. Chem. Phys.* **84**, 4524 (1986); A. D. Becke, *Phys. Rev. A* **33**, 2786 (1986).
36. T. Ziegler, V. Tschinke, and A. Becke, *J. Am. Chem. Soc.* **109**, 1351 (1987); *ibid.* *Polyhedron* **6**, 685 (1987); T. Ziegler, V. Tschinke, E. J. Baerends, J. G. Snijders, and W. Ravenek, *J. Phys. Chem.* **93**, 3050 (1989); L. Verluis and T. Ziegler, *J. Am. Chem. Soc.* **112**, 6163 (1990).
37. P. Mlynarski and D. R. Salahub, *Phys. Rev. B* **43**, 1399 (1991).
38. R. Fournier and A. E. DePristo, *J. Chem. Phys.* **96**, 1183 (1992).
39. J. Andzelm and E. Wimmer, *J. Chem. Phys.* **96**, 1280 (1992).
40. A. Becke, *J. Chem. Phys.* **96**, 2155 (1992).
41. A. St-Amant, Thèse de doctorat, Université de Montréal (1992); A. St-Amant and D. R. Salahub, *Chem. Phys. Lett.* **169**, 387 (1990).
42. D. R. Salahub, R. Fournier, P. Mlynarski, I. Papai, A. St-Amant, and J. Ushio in *Density Functional Methods in Chemistry*, Ed. by J. K. Labanowski and J. Andzelm (Springer, New York, 1991).
43. A. D. Becke, *J. Chem. Phys.* **88**, 2547 (1988).
44. R. S. Jones, J. W. Mintmire, and B. I. Dunlap, *Int. J. Quantum Chem. Symp.* **22**, 77 (1988).
45. S. H. Vosko, L. Wilk, and M. Nusair, *Can. J. Phys.* **58**, 1200 (1980).
46. R. Fournier, J. Andzelm, and D. R. Salahub, *J. Chem. Phys.* **90**, 6371 (1989); R. Fournier, *J. Chem. Phys.* **92**, 5422 (1990).
47. I. Papai, A. St-Amant, J. Ushio, and D. R. Salahub, *Int. J. Quantum Chem.*

- Symp. **24**, 29 (1990).
48. J. P. Perdew, Phys. Rev. Lett. **55**, 1665 (1985); J. P. Perdew and Y. Wang, Phys. Rev. B **33**, 8800 (1986).
49. J. Andzelm, N. Russo, and D. R. Salahub, J. Chem. Phys. **87**, 6562 (1987).
50. K. P. Huber and G. Herzberg, *Molecular Spectra and Molecular Structure. Constants of Diatomic Molecules* (Van Nostrand, Reinhold, New York, 1979), Vol. 4.
51. D. A. Dixon and J. L. Gole, Chem. Phys. Lett. **188**, 560 (1992).
52. C. Chatillon, M. Allibert, and A. Pattoret, C. R. Acad. Sci. Ser. C **280**, 1505 (1975).
53. D. R. Stull and H. Prophet, JANAF Thermochemical Tables, NSRDS Natl Stand. Ref. Data Serv. Natl. Bur. Stand. No. 37 (U.S. GPO, Washington D.C., 1971).
54. L. A. Bloomfield, R. R. Freeman, and W. L. Brown, Phys. Rev. Lett. **54**, 2246 (1985); L. A. Bloomfield, M. E. Geusic, R. R. Freeman, and W. L. Brown, Chem. Phys. Lett. **121**, 33 (1985).
55. J. R. Heath, Y. Liu, S. C. O'Brien, Q.-L. Zhang, R. F. Curl, F. K. Tittel, and R. E. Smalley, J. Chem. Phys. **83**, 5520 (1985); Y. Liu, Q.-L. Zhang, F. K. Tittel, R. F. Curl, and R. E. Smalley, *ibid.* **85**, 7434 (1986).
56. C.E. Moore, Atomic Energy Levels, NSRDS Natl. Stand. Ref. Data Serv. Natl. Bur. Stand. Circ. No 35 (US, GPO, Washington DC, 1969).
57. I. Mayer, Int. J. Quantum Chem. **26**, 151 (1984).
58. J. P. Perdew and A. Zunger, Phys. Rev. B **23**, 5048 (1980); S. H. Vosko and L. Wilk, J. Phys. B **16**, 3687 (1983); J. G. Harrison, J. Chem. Phys. **78**, 4562 (1983);

- K. A. Jackson and C. C. Lin, *Phys. Rev. B* **39**, 1557 (1989).
59. A. Zunger and M. L. Cohen, *Phys. Rev. B* **20**, 4082 (1979); Y. T. Shen, D. M. Bylander, and L. Kleinman, *Phys. Rev. B* **36**, 3465 (1987).
60. M. S. Hybertsen and S. G. Louie, *Phys. Rev. B* **34**, 5390 (1986).
61. C. L. Curtiss, P. W. Deutsch and K. Raghavachari, *J. Chem. Phys.* **96**, 6868 (1992).

**Table I:** Structural data and binding energies, which include the zero point energies, for Si clusters.

structure <sup>a</sup>	[(bonded atoms) bond length (Å): bond order]	PW/VWN BE(eV)
<b>Minima</b>		
2.0.1.t	[(1,2) 2.280 : 1.91]	3.62
2.0.2.t	[(1,2) 2.164 : 1.90]	3.55
3.0.1.t	[(1,2) 2.273 : 1.38]	7.82
3.0.2.s	[(1,2) 2.179 : 1.66] [(2,3) 2.840 : 0.87]	7.75
3.0.4.t	[(1,2) 2.247 : 1.53] [(2,3) 3.948 : 0.56]	6.47
4.0.1.s	[(1,2) 2.397 : 1.03] [(1,3) 2.316 : 1.07] [(3,4) 4.375 : 0.42]	12.36
4.0.2.t	[(1,2) 2.529 : 0.99] [(1,3) 2.274 : 1.10] [(3,4) 3.782 : 0.54]	11.69
4.0.3.t	[(1,2) 3.013 : 0.68] [(1,3) 2.277 : 1.13]	11.64
4.0.5.t	[(1,2) 2.256 : 1.16] [(2,3) 2.885 : 0.62]	10.23
4.0.7.s	[(1,2) 2.498 : 0.88]	9.94
5.0.1.s	[(1,2) 3.047 : 0.59] [(1,3) 2.304 : 0.94] [(3,4) 2.976 : 0.55]	16.50
5.0.2.s	[(1,2) 2.245 : 1.37] [(2,3) 2.318 : 0.91] [(2,4) 2.302 : 0.93] [(1,3) 2.394 : 0.83]	15.47
6.0.1.s	[(1,2) 2.333 : 0.80] [(2,5) 2.376 : 0.72] [(2,4) 2.390 : 0.66] [(4,5) 2.549 : 0.60] [(2,3) 2.680 : 0.61] [(1,5) 2.950 : 0.35] [(1,4) 3.889 : 0.40] [(5,6) 3.871 : 0.40]	20.72
6.0.2.s	[(1,2) 2.677 : 0.61] [(1,3) 2.347 : 0.78] [(1,5) 2.391 : 0.67] [(3,5) 2.712 : 0.46] [(5,6) 2.489 : 0.66] [(3,4) 3.092 : 0.31] [(3,6) 3.879 : 0.40]	20.69
7.0.1.s	[(1,2) 2.514 : 0.64] [(1,3) 2.461 : 0.58] [(3,4) 2.488 : 0.58] [(3,6) 4.025 : 0.23]	24.91
7.0.2.s	[(1,2) 2.500 : 0.53] [(1,5) 2.602 : 0.56] [(2,3) 2.495 : 0.56] [(4,5) 2.333 : 0.86] [(5,6) 4.155 : 0.12] [(2,7) 3.977 : 0.23]	24.31

**Table I: (continued)**

8.0.1.s	[(1,2) 2.478 : 0.54] [(1,7) 2.272 : 0.93] [(1,5) 2.401 : 0.69] [(1,4) 2.798 : 0.31] [(1,8) 3.848 : 0.10] [(2,7) 2.457 : 0.71] [(2,5) 2.772 : 0.40] [(2,6) 3.998 : 0.22] [(2,8) 4.245 : 0.10] [(2,3) 2.882 : 0.34] [(7,8) 5.667 : 0.23]	28.01
<b>Critical points with one or more imaginary frequencies</b>		
3.2.3.s	[(1,2) 2.182 : 1.78] [(2,3) 4.364 : 0.70]	7.26
4.1.4.t	[(1,2) 2.138 : 1.13] [(1,3) 3.278 : 0.54]	10.93
4.2.6.t	[(1,2) 2.164 : 1.42] [(1,3) 2.187 : 1.72] [(1,4) 4.350 : 0.29] [(3,4) 6.538 : 0.24]	9.90
5.1.3.s	[(1,2) 2.272 : 0.98] [(1,5) 2.516 : 0.70] [(1,3) 3.213 : 0.61]	15.18
5.4.4.t	[(1,2) 2.316 : 1.10] [(1,3) 3.748 : 0.44]	13.09
5.3.5.s	[(1,2) 2.221 : 1.06] [(1,3) 3.626 : 0.54]	11.14
6.2.3.s	[(1,2) 2.739 : 0.46] [(1,5) 2.361 : 0.73] [(5,6) 2.701 : 0.61] [(1,3) 3.875 : 0.41]	20.69
6.2.4.t	[(1,2) 2.447 : 0.69] [(1,3) 3.461 : 0.31]	19.99
6.2.5.s	[(1,2) 2.323 : 0.88] [(1,6) 2.391 : 0.88] [(1,4) 2.692 : 0.60] [(1,5) 3.571 : 0.15] [(5,6) 5.285 : 0.22]	19.09
7.2.3.s	[(1,2) 2.362 : 0.82] [(1,7) 2.290 : 1.05] [(1,4) 2.463 : 0.47] [(2,3) 2.780 : 0.56] [(1,6) 3.270 : 0.36] [(1,5) 3.560 : 0.17] [(6,7) 2.238 : 1.44] [(2,5) 2.339 : 0.95] [(2,6) 4.150 : 0.09] [(4,7) 3.289 : 0.36] [(5,6) 5.739 : 0.18]	22.17
8.1.2.s	[(1,2) 2.497 : 0.62] [(1,6) 2.674 : 0.40] [(1,8) 2.548 : 0.62] [(1,5) 3.848 : 0.20] [(1,4) 4.154 : 0.14] [(2,3) 2.432 : 0.73] [(2,4) 2.318 : 0.86] [(2,6) 2.461 : 0.61] [(2,7) 3.460 : 0.11] [(2,8) 4.110 : 0.09] [(4,5) 2.539 : 0.63] [(4,8) 5.706 : 0.21]	27.63
8.1.3.s	[(1,2) 2.326 : 0.85] [(1,5) 2.348 : 0.86] [(1,3) 2.606 : 0.44] [(1,7) 4.014 : 0.12] [(3,4) 2.479 : 0.62] [(3,5) 2.320 : 0.93] [(3,6) 3.483 : 0.14] [(5,6) 2.719 : 0.55] [(5,7) 5.306 : 0.13] [(5,8) 4.558 : 0.19]	27.20

**Table I: (continued)**

8.2.4.s	[(1,2) 2.388 : 0.66]	[(1,3) 2.668 : 0.47]	25.78
	[(3,4) 2.386 : 0.71]	[(3,5) 4.133 : 0.18]	
	[(3,6) 4.772 : 0.13]		
8.4.5.s	[(1,2) 2.339 : 0.99]	[(1,4) 3.600 : 0.28]	25.12
	[(1,6) 3.806 : 0.07]	[(1,5) 5.242 : 0.12]	
	[(2,3) 2.605 : 0.58]	[(2,6) 2.362 : 0.86]	
	[(2,7) 3.516 : 0.06]		

---

<sup>a</sup> n.j.m.l means the following: n=number of atoms in the cluster; j=number of imaginary frequencies; m=stability rank of the structure found in this work; l=singlet or triplet state.

**Table II:** Harmonic frequencies and zero point energies for Si clusters.<sup>a</sup>

structure <sup>b</sup>	harmonic frequencies (cm <sup>-1</sup> )	ZPE (kcal/mole)
2.0.1.t	480	0.69
2.0.2.t	549	0.78
3.0.1.t	340, 340, 508	1.70
3.0.2.s	171, 540, 548	1.80
3.0.4.t	55, 414, 513	1.40
3.2.3.s	388, 663; 79i, 79i	1.50
4.0.1.s	55, 248, 348, 436, 464, 495	2.93
4.0.2.t	169, 303, 312, 372, 461, 463	2.97
4.0.3.t	179, 202, 396, 403, 404, 479	2.95
4.1.4.t	190, 393, 393, 433, 464; 462i	2.68
4.0.5.t	101, 103, 184, 411, 415, 498	2.45
4.2.6.t	16, 16, 293, 512, 667; 34i, 34i	2.15
4.0.7.s	185, 185, 307, 307, 307, 419	2.44
5.0.1.s	178, 178, 232, 377, 377, 409, 440, 440, 476	4.44
5.0.2.s	99, 150, 189, 215, 329, 367, 472, 516, 517	4.08
5.1.3.s	250, 258, 262, 364, 423, 427, 453, 465; 295i	4.15
5.4.4.t	355, 355, 355, 454, 454; 171i, 171i, 159i, 159i	2.82
5.3.5.s	60, 60, 343, 534, 534, 534, 117i, 117i, 117i	2.95
6.0.1.s	11, 67, 147, 260, 309, 319, 379, 393, 412, 445, 448, 463	5.22
6.0.2.s	18, 53, 146, 261, 312, 318, 378, 400, 405, 444, 455, 458	5.22
6.2.3.s	150, 237, 302, 326, 389, 411, 411, 449 454, 454; 46i, 46i	5.12
6.2.4.t	153, 153, 165, 359, 362, 374, 374, 384, 384, 437; 484i, 484i	4.50
6.2.5.s	231, 248, 248, 270, 368, 368, 369, 409, 413, 499; 165i, 165i	4.89
7.0.1.s	171, 171, 220, 220, 229, 288, 288, 334, 334, 337, 337, 356, 415, 415, 431	6.50
7.0.2.s	123, 123, 154, 203, 203, 296, 296, 316, 332, 332, 348, 425, 451, 509, 509	6.60
7.2.3.s	84, 86, 177, 242, 273, 290, 328, 361, 381, 429, 445, 476, 492; 127i, 47i	5.81
8.0.1.s	57, 93, 142, 162, 218, 239, 255, 291, 293 295, 308, 313, 335, 356, 387, 392, 511, 513	7.38

**Table II:** (continued)

8.1.2.s	114, 139, 146, 178, 226, 253, 269, 278, 283, 291, 323, 331, 346, 395, 398, 477, 500; 231i	7.07
8.1.3.s	132, 142, 176, 185, 221, 234, 242, 274, 296, 344, 365, 380, 392, 399, 485, 487, 515; 135i	7.53
8.2.4.s	76, 97, 99, 106, 213, 213, 224, 225, 225, 338, 348, 348, 400, 432, 457, 457; 265i, 265i	6.08
8.4.5.s	35, 99, 180, 210, 263, 305, 318, 334, 347, 415, 424, 435, 466, 511; 156i, 108i, 86i, 86i	6.20

---

<sup>a</sup> Computed using the VWN exchange-correlation potential.

<sup>b</sup> n.j.m.l means the following: n=number of atoms in the cluster; j=number of imaginary frequencies; m=stability rank of the structure found in this work; l=singlet or triplet state.

**Table III:** Total energies of Si clusters using the VWN and PW potentials.

structure <sup>a</sup>	VWN energy (hartrees)	PW/VWN energy (hartrees)
1.0.1.t	-3.746493	-3.807553
1.0.2.q	-3.600459	-3.614254
2.0.1.t	-7.638734	-7.748750
2.0.2.t	-7.639097	-7.746123
3.0.1.t	-11.566728	-11.712871
3.0.2.s	-11.565056	-11.710177
3.2.3.s	-11.538178	-11.691696
3.0.4.t	-11.505257	-11.662687
4.0.1.s	-15.505146	-15.688910
4.0.2.t	-15.479602	-15.664584
4.0.3.t	-15.475681	-15.662743
4.1.4.t	-15.445992	-15.636294
4.0.5.t	-15.421578	-15.610173
4.2.6.t	-15.400259	-15.597249
4.0.7.s	-15.416697	-15.599213
5.0.1.s	-19.432703	-19.651122
5.0.2.s	-19.388251	-19.611354
5.1.3.s	-19.400868	-19.616704
5.4.4.t	-19.286116	-19.523428
5.3.5.s	-19.229175	-19.450788
6.0.1.s	-23.363347	-23.614884
6.0.2.s	-23.362517	-23.613982
6.2.3.s	-23.362659	-23.613695
6.2.4.t	-23.331940	-23.587256
6.2.5.s	-23.293784	-23.554478
7.0.1.s	-27.294570	-27.578682
7.0.2.s	-27.269346	-27.556774
7.2.3.s	-27.178770	-27.476987
8.0.1.S	-31.176692	-31.501601
8.1.2.s	-31.162292	-31.486930
8.1.3.s	-31.142333	-31.471816
8.2.4.s	-31.092494	-31.417071
8.4.5.s	-31.051242	-31.393575

<sup>a</sup> n.j.m.l means the following: n=number of atoms in the cluster; j=number of imaginary frequencies; m=stability rank of the structure found in this work; l=singlet or triplet state.

**Table IV:** Theoretical and experimental estimates of the binding energies (in eV) for the global minima of  $\text{Si}_n$ ,  $n = 2-8$ . The binding energies include the zero point energies. The equilibrium structures<sup>a</sup> whose energies are reported below are as follows: 2.0.1.t; 3.0.1.t for the VWN calculations and 3.0.2.s for the MP4 calculations; 4.0.1.s; 5.0.1.s; 6.0.1.s; 7.0.1.s; and 8.0.1.s.

n	MP4 <sup>b</sup>	VWN	MP4 <sup>b</sup> corr.	VWN corr.#1	VWN corr.#2	PW/VWN	experiment
2	2.60	3.94	3.12	3.18	3.20	3.62	3.21 <sup>c</sup>
3	6.34	8.83	7.61	7.69	7.60	7.82	7.6±0.2 <sup>d</sup>
4	10.57	14.00	12.68	12.48	12.03	12.36	
5	13.74	18.86	16.49	16.96	16.40	16.50	
6	18.02	23.84	21.62	21.56	20.89	20.72	
7	22.16	28.81	26.59	26.15	25.37	24.91	
8	24.31	32.46	29.17	29.42	28.52	28.01	

<sup>a</sup> n.j.m.l means the following: n=number of atoms in the cluster; j=number of imaginary frequencies; m=stability rank of the structure found in this work; l=singlet or triplet state.

<sup>b</sup> Refs. 2 and 3.

<sup>c</sup> Ref. 50.

<sup>d</sup> Ref. 52.

**Table V:** PW/VWN binding energy (BE), promotion energy (PE), intrinsic binding energy (IBE) and the ratio PE/IBE for silicon clusters.

structure <sup>a</sup>	BE(eV)	PE(eV)	IBE(eV)	PE/IBE
2.0.1.t	3.62	0.35	3.97	0.09
2.0.2.t	3.55	1.33	4.88	0.27
3.0.1.t	7.82	2.20	10.02	0.22
3.0.2.s	7.75	1.95	9.70	0.20
3.2.3.s	7.26	2.32	9.58	0.24
3.0.4.t	6.47	2.04	8.51	0.24
4.0.1.s	12.36	3.09	15.47	0.20
4.0.2.t	11.69	4.23	15.92	0.27
4.0.3.t	11.64	3.58	15.22	0.24
4.1.4.t	10.93	3.42	13.35	0.24
4.0.5.t	10.23	2.36	12.59	0.19
4.2.6.t	9.90	3.58	13.48	0.27
4.0.7.s	9.94	1.30	11.24	0.12
5.0.1.s	16.50	4.93	21.43	0.23
5.0.2.s	15.47	5.66	21.13	0.27
5.1.3.s	15.57	5.54	21.11	0.26
5.4.4.t	13.09	5.45	18.54	0.29
5.3.5.s	11.14	3.87	15.01	0.26
6.0.1.s	20.72	5.33	26.05	0.20
6.0.2.s	20.69	5.37	26.06	0.21
6.2.3.s	20.69	5.13	25.82	0.20
6.2.4.t	19.99	5.97	25.96	0.23
6.2.5.s	19.09	6.35	25.44	0.25
7.0.1.s	24.91	6.43	31.34	0.21
7.0.2.s	24.31	7.37	31.68	0.23
7.2.3.s	22.17	9.04	31.21	0.29
8.0.1.s	28.01	8.58	36.59	0.23
8.1.2.s	27.63	9.12	36.75	0.25
8.1.3.s	27.20	9.93	37.13	0.27
8.2.4.s	25.78	7.08	32.86	0.22
8.4.5.s	25.12	9.12	34.24	0.27

<sup>a</sup> n.j.m.l means the following: n=number of atoms in the cluster; j=number of imaginary frequencies; m=stability rank of the structure found in this work; l=singlet or triplet state.

**Table VI:** The PE/IBE ratio, average coordination number and HOMO-LUMO gap of the Si clusters.

structure <sup>a</sup>	PE/IBE <sup>b</sup>	$\langle x \rangle$	HOMO-LUMO gap (eV) <sup>c</sup>
2.0.1.t	0.09	1.00	1.17
2.0.2.t	0.27	1.00	1.19
3.0.1.t	0.22	2.00	1.70
3.0.2.s	0.20	1.88	1.04
3.2.3.s	0.24	1.79	1.36
3.0.4.t	0.24	1.76	0.46
4.0.1.s	0.20	2.83	1.05
4.0.2.t	0.27	2.88	1.17
4.0.3.t	0.24	2.87	1.85
4.1.4.t	0.24	2.76	1.14
4.0.5.t	0.19	2.79	0.81
4.2.6.t	0.26	1.98	1.40
4.0.7.s	0.12	3.00	0.40
5.0.1.s	0.23	3.80	1.94
5.0.2.s	0.27	3.21	0.73
5.1.3.s	0.26	3.87	0.71
5.4.4.t	0.29	3.37	0.60
5.3.5.s	0.26	3.68	0.72
6.0.1.s	0.20	4.73	2.09
6.0.2.s	0.20	4.72	2.13
6.2.3.s	0.19	4.79	2.07
6.2.4.t	0.24	4.69	1.12
6.2.5.s	0.23	3.89	0.57
7.0.1.s	0.21	5.52	2.12
7.0.2.s	0.25	5.06	1.76
7.2.3.s	0.29	3.98	0.45
8.0.1.s	0.23	5.31	1.45
8.1.2.s	0.25	5.18	0.57
8.1.3.s	0.27	4.73	0.95
8.2.4.s	0.22	5.68	0.13
8.4.5.s	0.27	3.78	0.21

<sup>a</sup> n.j.m.l means the following: n=number of atoms in the cluster; j=number of imaginary frequencies; m=stability rank of the structure found in this work; l=singlet or triplet state.

<sup>b</sup> PW/VWN values.

<sup>c</sup> For triplet states we give the average over the two spin manifolds. The HOMO-LUMO gap is reported for the VWN exchange-correlation potential.

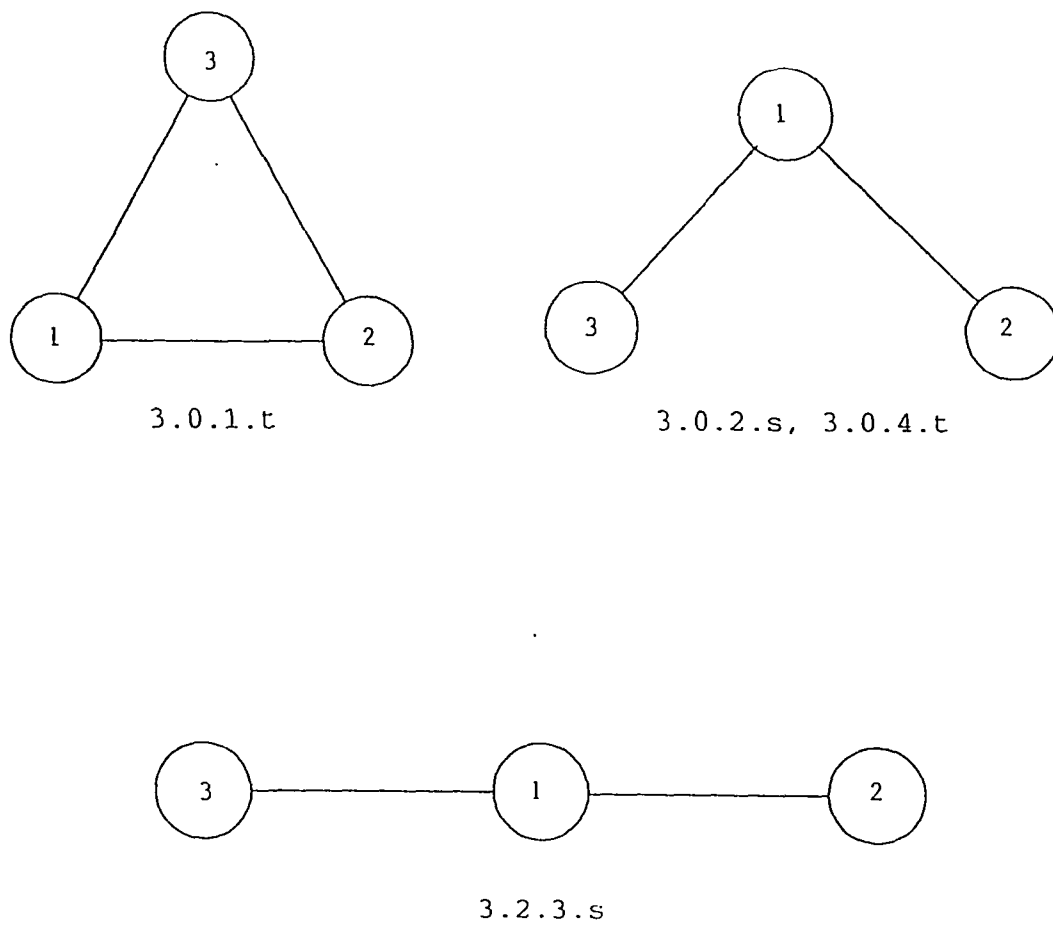


**Fig. 1:** The Si<sub>3</sub> clusters studied. See text for the cluster labelling convention.

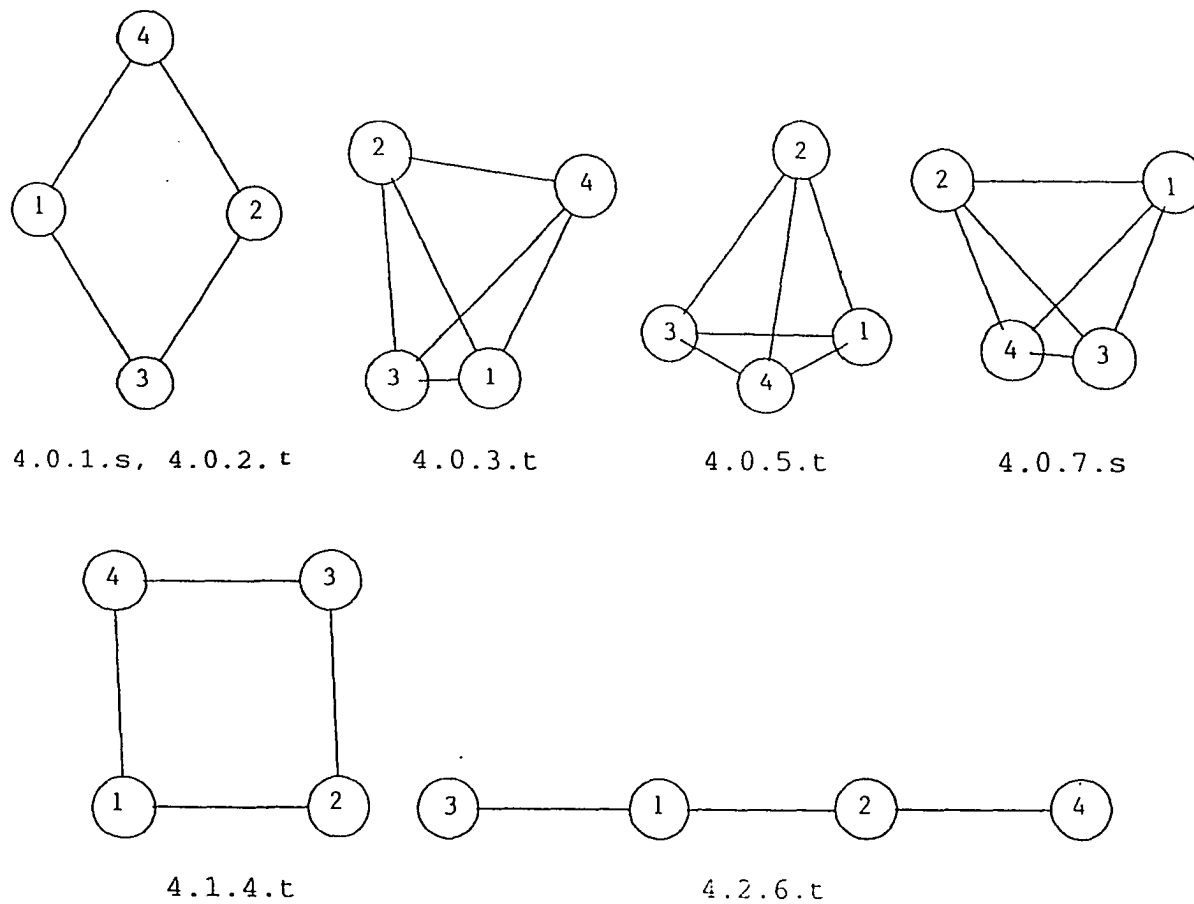


**Fig. 2:** The Si<sub>4</sub> clusters studied. See text for the cluster labelling convention.

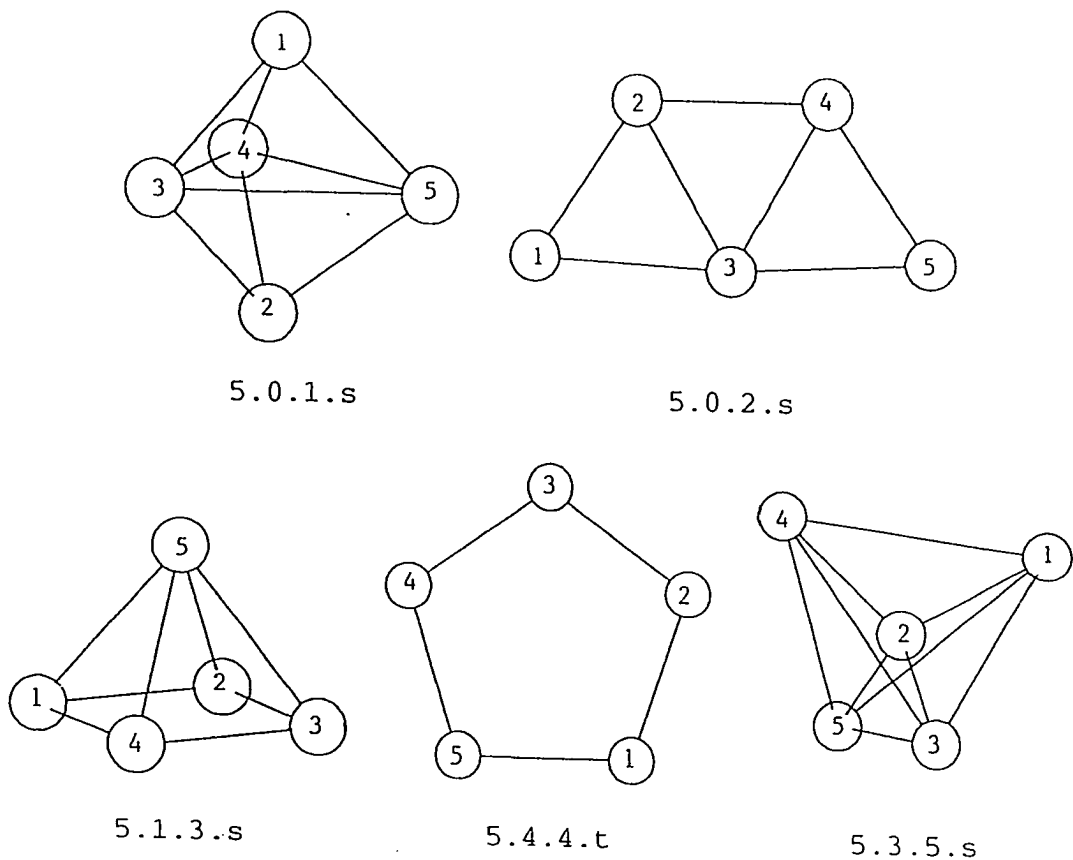


**Fig. 3:** The  $Si_5$  clusters studied. See text for the cluster labelling convention.

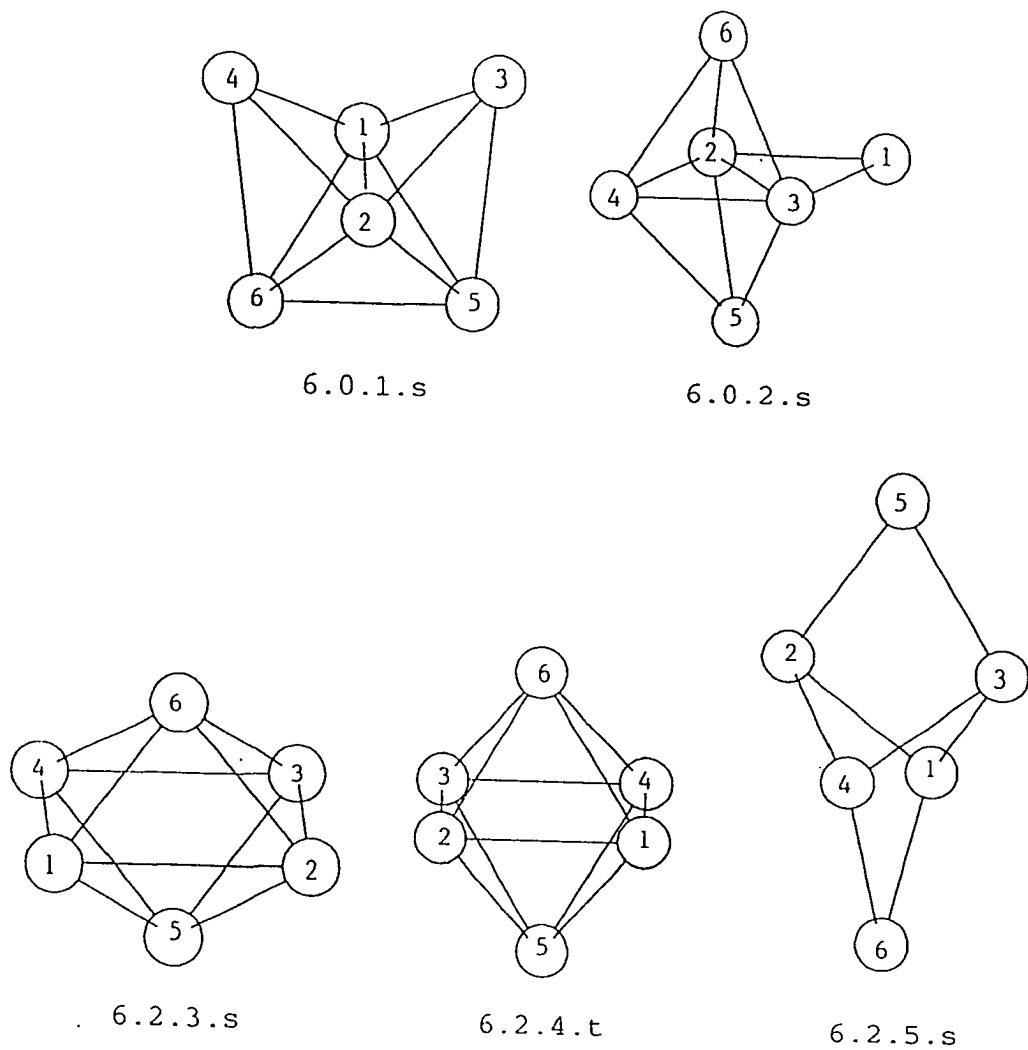


**Fig. 4:** The Si<sub>6</sub> clusters studied. See text for the cluster labelling convention.

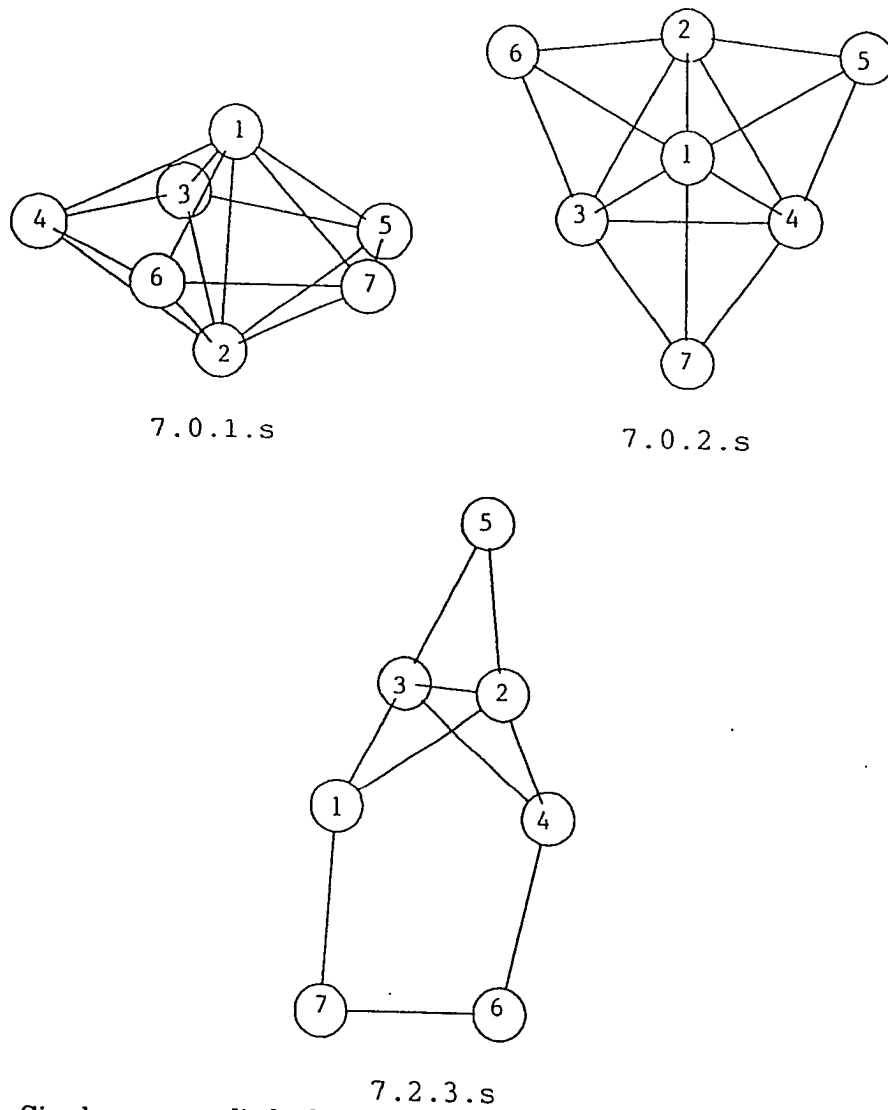
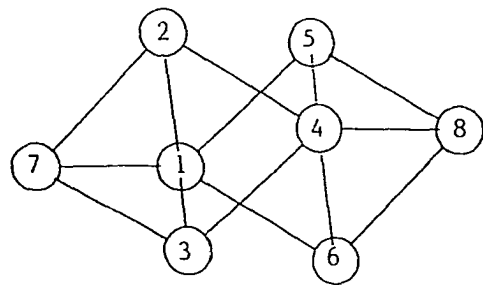
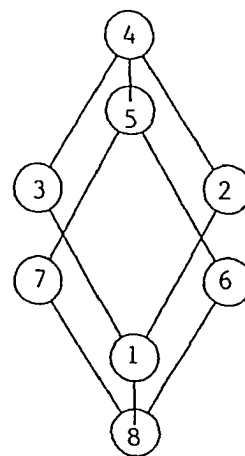


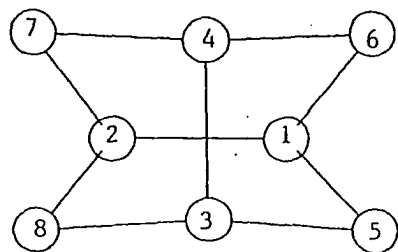
**Fig. 5:** The  $Si_7$  clusters studied. See text for the cluster labelling convention.



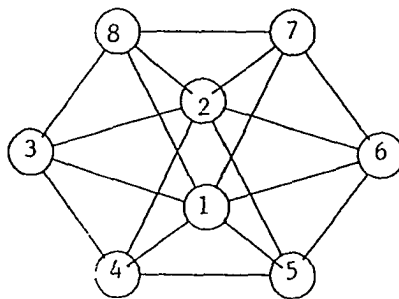
8.0.1.s



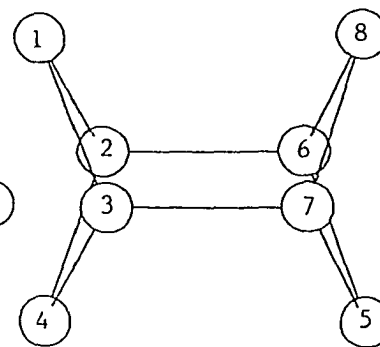
8.1.2.s



8.1.3.s



8.2.4.s



8.4.5.s

**Fig. 6:** The  $Si_8$  clusters studied. See text for the cluster labelling convention.

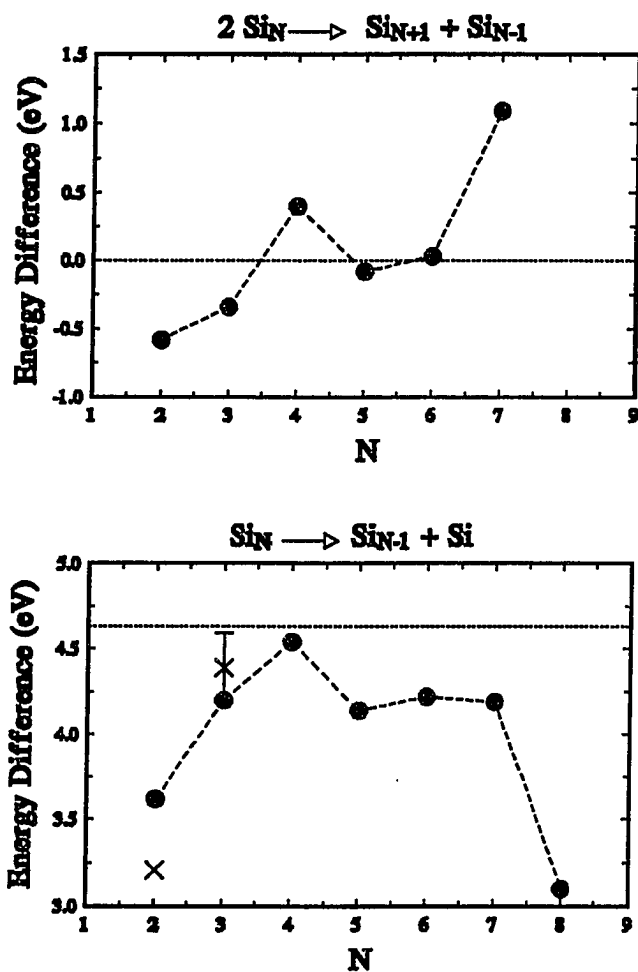


**Fig. 7:** a) The disproportionation energy as a function of the number of atoms in the cluster. This is one measure of relative cluster stability. The line denotes the zero energy. b) The incremental binding energy as a function of the number of atoms in the cluster. This is another measure of cluster stability. The X's represent the experimental values, while the line indicates the bulk cohesive energy.

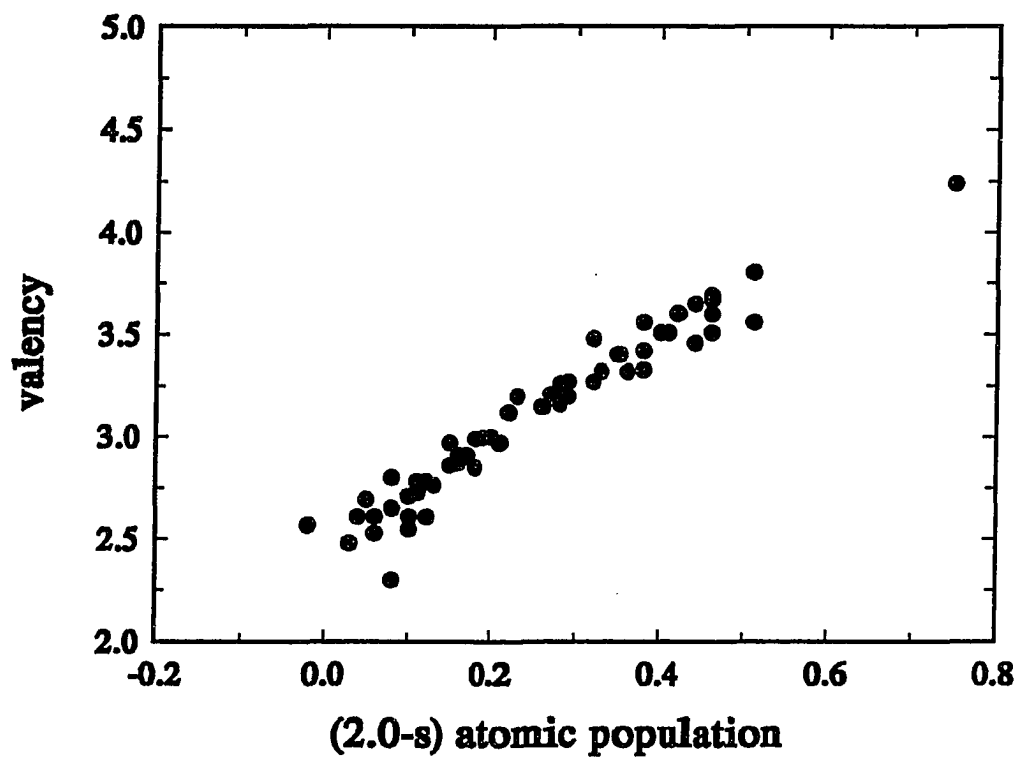


**Fig. 8:** The valency of the silicon atoms as a function of the quantity (2.0 - s-atomic population). This is the hybridization of the silicon atoms in the silicon clusters studied.

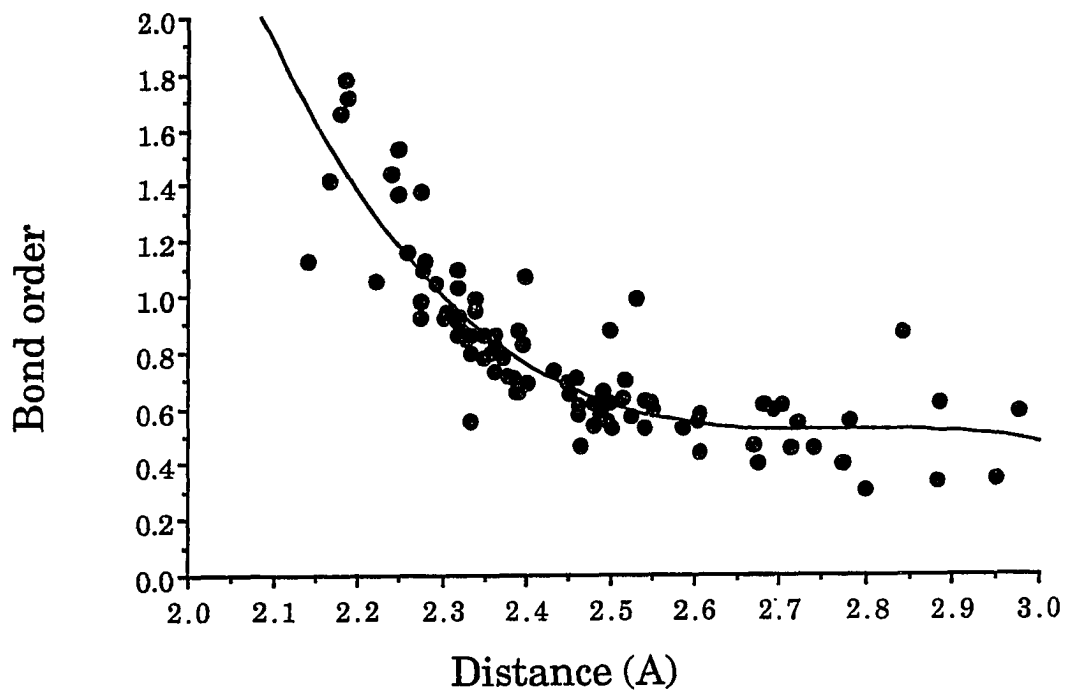


**Fig. 9:** The bond order of the individual Si atoms in the clusters as a function of the length of the bond.

PAPER 2. CORRECTED EFFECTIVE MEDIUM STUDY  
OF METAL SURFACE RELAXATION

**CORRECTED EFFECTIVE MEDIUM STUDY  
OF METAL SURFACE RELAXATION**

**Susan B. Sinnott, Mark S. Stave, Todd J. Raeker and Andrew E. DePristo**

**Department of Chemistry**

**Iowa State University**

**Ames , Iowa 50011**

**Printed in**

**Physical Review B 44, 8927 (1991)**

**ABSTRACT**

We have studied the relaxation of some metal surfaces using a corrected effective medium (CEM) theory. CEM is a non self-consistent, density functional technique. The interaction energy is calculated as a sum of three components: the embedding energy of an atom in jellium, the interatomic coulomb energy, and the kinetic-exchange-correlation energy. A new theoretical procedure has been developed to determine the embedding energies via linear muffin tin orbital calculations. This refinement of the theory is tested for surface energies and structures of some relaxed Al, Ni, Cu, Rh, Pd, and Ag surfaces. Comparisons are made to the embedded atom method, the effective medium technique, and a simpler version of CEM that is used in molecular dynamics and Monte Carlo simulations. We present an in-depth analysis of the results, and discuss the physical basis of surface relaxation within CEM. Finally, we address the limitations inherent in calculations of metal surface relaxation.

## INTRODUCTION

The phenomena of reconstruction and relaxation of metal surfaces has received considerable attention. Considerable experimental data indicate multilayer oscillatory relaxation of surfaces<sup>1</sup>. In addition, theoretical results<sup>2-19</sup> support these findings.

The most rigorous theoretical calculations have involved the self-consistent density functional method<sup>2-11</sup>. These have been used to determine the structure of metal surfaces but only for a few systems due to the large computational expense involved. More extensive investigations have utilized simpler theoretical procedures such as the embedded atom method (EAM)<sup>12-15</sup>, the effective medium (EM) theory<sup>16-18</sup> and a corrected effective medium (CEM) method<sup>19-23</sup>.

Like other effective medium type methods, CEM theory starts by modeling the interaction of any one atom with all the other atoms in the system by that atom interacting with jellium (an infinite homogeneous electron gas with a uniform compensating positive density). This is repeated for all atoms in the system, and the total of all these atom-jellium interactions forms the zero'th order representation. This process simplifies the N-body problem to a set of N one-body problems.

The interaction energy for the atom-in-jellium system, called the embedding energy of the atom, is a function of the electron density of the jellium for any particular type of atom. Since this embedding energy is a major component of the system interaction energy,<sup>24</sup> it is important to determine accurate embedding energies.

In previous work<sup>19,21,23</sup>, these embedding functions have been constructed from experimental data on homonuclear diatomic and bulk binding energy curves. The resulting semi-empirical embedding functions must be interpolated for use in the density region of importance for surface properties. In this paper we present a new purely theoretical method to determine these embedding energies. In particular, we use the linear muffin tin orbital (LMTO) technique, an SCF-LD method developed by Skriver<sup>25</sup>, to determine cohesive energy curves over a wide range of lattice constants, and then use these results to construct the embedding functions. We test this refinement of the CEM theory for surface energies and structures of some relaxed simple and transition FCC metal surfaces.

We have also improved the numerical accuracy and computational efficiency of the CEM calculations. Thus, many more surfaces are investigated in the present work.

An approximation to the CEM method, with acronym MD/MC-CEM, has been developed to allow for efficient use of the method in molecular dynamics and monte-carlo simulations<sup>22</sup>. The MD/MC-CEM theory is about  $10^3$ - $10^4$  times faster to evaluate than the full CEM theory, being comparable in speed and formal structure to the EAM method. Thus, we have also tested the adequacy of the MD/MC-CEM values for surface energies and relaxations using embedding functions determined from the LMTO technique.

We assess our attempts at improving CEM and MD/MC-CEM theories, and suggest additional improvements that might produce even better results. Some comparison is also made to the EAM and EM methods. Finally, we present an in-

depth analysis of our results, discussing the physical basis of surface relaxation within CEM and addressing the limitations inherent in calculations of the relaxation of metal surfaces.

In an appendix, we provide details of the LMTO calculations on the cohesive energies of the metals Al, Ni, Cu, Rh, Pd, Ag, Pt and Au. These results span a large range of lattice constants, and thus can be useful in any situation requiring cohesive energies for very compressed and/or expanded lattices.

## THEORY

We present a brief overview of the CEM theory here, focusing on the particular features needed to understand the bulk and surface energy applications. Other details can be found in Refs. 19-23.

Assuming that the total system electron density can be approximated as the superposition of atomic electron densities, one can show that the CEM cohesive energy is given by the expression:

$$\Delta E_{\text{coh}}(A_b) = \Delta E_J(A_b; n_b) + \frac{1}{2} \sum_{j \neq b} V_c(bj) + \Delta G_{\text{WS}(b)} \quad (1)$$

where  $A_b$  labels any equivalent (bulk) atom in the system, and is referred to as the focus atom.  $\Delta E_J(A_b; n_b)$  is the energy of embedding this atom into jellium of density  $n_b$ .  $V_c(bj)$  is the sum of electron-electron, electron-nuclear and nuclear-nuclear coulomb interactions between atoms  $A_b$  and  $A_j$ .  $\Delta G_{\text{WS}(b)}$  is an explicit correction for the kinetic-exchange-correlation energy difference between the inhomogeneous electron gas in the real bulk system and the effective atom-jellium system.<sup>26</sup> It involves an integration over the Wigner-Seitz cell of atom  $A_b$ .

Minimizing  $\Delta G_{\text{WS}(b)}$  with respect to the jellium densities yields the expression for the jellium density:

$$n_b = \frac{1}{2Z_b} \sum_{j \neq b} \int n(\vec{r} - \vec{R}_b) n(\vec{r} - \vec{R}_j) d\vec{r} \quad (2)$$

Here,  $n(\vec{r} - \vec{R}_i)$  is the unpolarized atomic electron density distribution (from Hartree-Fock (HF) calculations);  $Z_i$  and  $\vec{R}_i$  are the atomic number and nuclear position, respectively, of atom  $A_i$ ;  $\vec{r}$  is the electron density at any point in space.

It is worthwhile to emphasize that the only unknown part of the CEM energy expression is the embedding function. Once this is specified, the theory can be used to predict the interaction energies for a system in any geometry, not just for the 3D periodic geometry. The relevant formulas are given in Refs. 19-23.

To obtain these embedding functions, we have developed a theoretical procedure based upon use of LMTO calculated cohesive energies<sup>25</sup>. The details of the LMTO generation of these values is provided in the appendix. Assuming that the cohesive energy is known, we rewrite Eq. (1) as

$$\Delta E_{\text{LMTO}}(A_b; n_b) = \Delta E_{\text{coh, LMTO}}(A_b) - \frac{1}{2} \sum_{j \neq b} V_c(b_j) - \Delta G_{\text{WS}(b)} \quad (3)$$

which defines the LMTO generated embedding energy. Calculations of  $\Delta E_{\text{coh, LMTO}}(A_b)$  at various lattice constants yields  $\Delta E_{\text{LMTO}}(A_b; n_b)$  at various  $n_b$  since the jellium density varies with atomic separation via Eq. (2). The subscript 'LMTO' simply indicates that the embedding functions are generated from LMTO calculations of the cohesive energy.

Before showing results of this procedure, we emphasize the need for calculated values of  $\Delta E_{\text{coh}}$ . Experimental data on the variation of  $\Delta E_{\text{coh}}$  with lattice constant is

severely limited for two reasons: 1/ contractions of more than a few percent require extremely high pressure; 2/ stretching more than a few percent leads to fracture. Thus, it is only through calculations that significant variations of  $\Delta E_{\text{coh}}$  with lattice constant can be determined. In the present work, lattice constants were varied from 10% contractions to 30% expansions. The severity of these conditions is easily understood by noting that for Ni a 10% contraction decreases  $\Delta E_{\text{coh}}$  from 4.44 eV to 3.36 eV while a 30% expansion decreases it to 1.97 eV. For comparison, the binding energy of a surface atom on Ni(111) is estimated to be 3.82 eV. Hence, one would form a surface well before any such 30% expansion could be reached.

In Fig. 1, we compare the present LMTO generated embedding function for the Cu atom,  $\Delta E_{\text{LMTO}}(\text{Cu};n)$ , with that determined in previous work using a different procedure<sup>27</sup>. Both embedding functions have the same shape. The essential difference occurs in the density region between slight expansions of the bulk and the diatomic equilibrium position. The previous semi-empirical procedure requires an interpolation over a large density range while the present LMTO embedding functions are determined *directly* throughout this region. To see the importance of this, we have indicated the jellium density calculated from Eq. (2) for an atom in the first layer of the perfectly terminated Cu(111), Cu(100), Cu(110), Cu(331), Cu(311), and Cu(210) surfaces. The densities at these points correspond to approximately a 10-15% expansion of the lattice from the bulk lattice constant, with the more closed-packed faces corresponding to the smaller expansions (high densities) and the open faces corresponding to the larger expansions (low densities). The LMTO embedding functions have points throughout the surface region while the semi-empirical

embedding functions only have points in the high density end of the surface region. The only extrapolation in the LMTO embedding functions is between the lowest density point and the zero density point. Since the density of the region of extrapolation is so small, this has no effect on the energies of the surface or bulk region.

The difference between the two embedding functions is not the same for all atoms. It is larger for the Cu atom than for any of the other atoms studied. The disparity between the embedding energies is 0.150 eV for an atom on the perfectly terminated Cu(110) surface. The deviation between the two embedding functions is smallest for the 4d transition metals, Rh, Pd, and Ag. In Fig. 2, we compare the LMTO generated embedding function for the Pd atom,  $\Delta E_{\text{LMTO}}(\text{Pd};n)$ , with the embedding function determined previously. We have indicated the jellium density calculated from Eq. (2) for an atom in the first layer of the perfectly terminated Pd(111), Pd(100), and Pd(110) surfaces. The difference between the two curves is only 0.004 eV for an atom on the ideal Pd(110) surface.

The CEM theory has a computationally intensive part, namely the three dimensional multicenter integration needed to evaluate  $\Delta G$ . Thus, a still simpler theory, with acronym MD/MC-CEM, has been developed in Ref. 22, in which the last term in Eq. (1) is *approximated* as a function of jellium density. This yields

$$\Delta E_{\text{coh}}(A_i) = \Delta F_j(A_i;n_i) + \frac{1}{2} \sum_{j \neq i} V_c(i,j) \quad (4)$$

where  $\Delta F_j$  is an effective embedding energy within the more approximate theory.

This MD/MC-CEM theory is not as general as the original CEM theory since the  $\Delta G$  term is not simply a function of the jellium density.

The LMTO cohesive energy variation with lattice constant can be used analogously to find

$$\Delta F_{\text{LMTO}}(A_b; n_b) = \Delta E_{\text{coh,LMTO}}(A_b) - \frac{1}{2} \sum_{j \neq b} V_c(b_j) \quad (5)$$

We compare the functions  $\Delta E_{\text{LMTO}}(\text{Cu}; n)$  and  $\Delta F_{\text{LMTO}}(\text{Cu}; n)$  in Fig. 3. While the MD/MC-CEM embedding function is steeper than the CEM embedding function, the qualitative behavior of both curves is essentially the same. All metals exhibit similar characteristics to Cu in this regard.

With these newly constructed embedding functions using a purely theoretical method and relying on very little extrapolation of data, we are now in a good position to test the CEM and MD/MC-CEM theories. The surface energies and relaxations are used in this article for that purpose. To calculate these, it was shown<sup>19</sup> that for infinitely periodic, homogeneous atomic surfaces the cohesive energy of an atom in a particular layer ( $\lambda$ ) can be written as

$$\Delta E_\lambda = \Delta E_J(A_\lambda; n_\lambda) + \frac{1}{2} \sum_{j \neq \lambda} V_c(\lambda_j) + \Delta G_\lambda \quad (6)$$

The difference from Eq. (1) occurs in the jellium densities and coulomb integrals which depend upon the number of neighbors, and in the  $\Delta G_\lambda$  which now involves an integration over a generalization of the Wigner-Seitz cell. The analogous equation for MD/MC-CEM involves simply dropping the  $\Delta G_\lambda$  term and replacing  $\Delta E_J(A_\lambda; n_\lambda)$

with  $\Delta F_J(A_\lambda; n_\lambda)$ . Given the energies of any equivalent atom in a layer, the surface energies are then determined from

$$\sigma = \frac{\sum_{\lambda=1}^{\infty} [\Delta E_\lambda - \Delta E_b]}{\text{surface unit cell area}} \quad (7)$$

where  $\lambda=1$  is the surface layer and as  $\lambda \rightarrow \infty$ ,  $\Delta E_\lambda$  converges to  $\Delta E_b$ . To determine the extent of relaxation, we minimize Eq. (7) with respect to the layer distance spacings. In-plane reconstruction was not considered in these calculations.

## RESULTS

In table I we present the surface energies of some relaxed surfaces calculated with the LMTO embedding functions. The systems under study are most of the simple and transition FCC metal surfaces that do not reconstruct.

First, we must explain the notation in table I (and many of the other tables). Many of the differences in surface energies between the relaxed and unrelaxed surfaces are quite small, with the largest being on the order of  $0.1 \text{ J/m}^2$  and the smallest being on the order of  $0.001 \text{ J/m}^2$ . However, the limit to the numerical accuracy of the CEM method is about  $0.001\text{-}0.003 \text{ J/m}^2$ , depending on the area of the specific unit cell. This intrinsic accuracy arises from numerical integration in the  $\Delta G_\lambda$  and the interpolation of the embedding energy. When the relaxation energy differences are smaller than this limit, the resulting structure is uncertain. Only the Ag(111) surface falls into this category with the CEM theory. More surfaces calculated with MD/MC-CEM are uncertain, however, including Ni(100), Rh(100), Pd(100), Ag(100), Rh(111), Pd(111), and Ag(111). The relaxed surface structures that are uncertain are distinguished by square brackets in the tables. For consistency in identifying these surfaces, we have also placed square brackets around the analogous surface energies although these surface energies are not uncertain, just essentially unchanged between the relaxed and perfectly terminated surface.

The calculated surface energies,  $\sigma$ , for the low-index faces follow the ordering of  $\sigma(1,1,1) < \sigma(1,0,0) < \sigma(3,3,1) < \sigma(1,1,0) \approx \sigma(3,1,1) < \sigma(2,1,0)$ . This progression is correctly described by the number of missing nearest neighbors (MNN) for each

surface. Assuming that all NN bonds are of equal strength at the surface and in the bulk, such a dependence on MNN leads to the formula

$$\frac{\sigma(i,j,k)}{\sigma(1,1,1)} = \frac{MNN(i,j,k)}{3} \frac{area(1,1,1)}{area(i,j,k)} \quad (8)$$

where (i,j,k) specifies the Miller indices and area(i,j,k) is the surface unit cell area. Eq. (8) yields the following numerical results.  $\sigma(1,1,1) : \sigma(1,0,0) : \sigma(3,3,1) : \sigma(1,1,0) : \sigma(3,1,1) : \sigma(2,1,0) = 1 : 1.15 : 1.19 : 1.22 : 1.22 : 1.29$ . Not only is the ordering perfect but the prediction that  $\sigma(1,1,0) \approx \sigma(3,1,1)$  holds to high accuracy. The latter is especially surprising since  $MNN(1,1,0)=6$  while  $MNN(3,1,1)=7$ . However, the values of the surface energy do not correspond quantitatively to the MNN/area formula. Instead, this simple dependence upon MNN/area overestimates the surface energy by roughly a factor of 2. This makes sense, since once the bonds to the MNN are broken, the bonds to the remaining neighbors will strengthen, thus lowering the energy of surface formation.

Some surface free energies found from experimentally measured quantities of the polycrystalline surface of each metal are also listed in table I. These surface free energies have been determined at room temperature<sup>28</sup> and at the metal's melting temperature<sup>28,29</sup>. It is necessary to extrapolate the experimental values to 0 K for comparison to our surface energies. This leads to considerable uncertainties since there are quite large discrepancies between the two sets of surface free energies

found at the metal's melting temperature. To obtain surface energies, we plotted surface free energy versus temperature and extrapolated linearly to zero Kelvin. Apparently, CEM and MD/MC-CEM underestimate slightly the surface energies consistently for all the metals. The predicted values are quite good. By comparison, the related EAM method consistently underestimates the values of  $\sigma(i,j,k)$  by up to 50%<sup>23,30</sup>. This is discussed more below.

For a comparison of the CEM and MD/MC-CEM surface energies with those calculated using simple two-body potentials and the very common EAM method<sup>12-15</sup>, we considered Cu with the results shown in table II. The two parameters in the Lennard-Jones (12,6) potential were chosen to duplicate the lattice constant and cohesive energy of Cu, while the three parameters in the Morse potential were chosen to also duplicate the Debye frequency. The surface energies found with the Lennard-Jones (12,6) potential are gross overestimates but at least are correctly ordered with surface face. By contrast, the results with the Morse potential indicate that the (100) surface is more stable than the (111) surface. Although it is perhaps surprising that the more flexible Morse potential is worse, one should keep in mind that the use of a two-body potential to describe metallic bonding is not even qualitatively correct, and thus which potential is better turns out to be a moot point. The EAM method is considerably better than either of the two-body potentials for Cu, but sometimes underestimates  $\sigma$  by about a factor of two which is about as much as the two-body potentials overestimate it. The interested reader is referred to Refs. 23 and 30 for more extensive comparisons among the EAM, EM, CEM, MD/MC-CEM and two-body potentials. The general conclusion from these studies and table II is

that both the CEM and MD/MC-CEM methods do a good job of finding reliable surface energies.

Now, we turn to the prediction of surface geometries, in particular the change in the interlayer spacing. A recent, comprehensive listing of experimental relaxation data can be found in Ref. 1. For many surfaces, there is so much relaxation data available (with many disagreements) that we had to make some decisions about what to include. One major criterion was used: when any experiment found significant multilayer relaxation, a particular set of experimental data was retained only if multiple layer relaxation was allowed in the analysis. Within this restriction, we have referenced the most recent results when the number of experiments was still too large. In all cases, we try to present a collection of data that is internally consistent at least with respect to qualitative behavior.

The CEM and MD/MC-CEM results are compared to experimental data and to other effective medium type values in tables III-VI. Focus on the Al system in table III first. The CEM values describe the qualitative features of the relaxation of the first layer of most of the surfaces studied, especially the systematic variation with surface. In contrast to the behavior of surface energies, the (110) and (311) surfaces do not contract equally. The larger contraction of the latter indicates that the increase in MNN is more important than the increase in surface area. In addition, the agreement between CEM and experimental values for  $\Delta d_{12}$  (%) is within 3-4% for the surfaces with significant contractions. Nevertheless, there are some discrepancies, especially the CEM prediction of a small contraction of the top layer in Al(111) and Al(100). This 3-4% overestimation of the contraction is consistent

throughout all of the Al surfaces, but is just more striking for the low index faces which show negligible contractions or even an expansion experimentally. The second discrepancy involves the underestimation of the second layer expansion.

For the Ni system in table IV, CEM again describes the qualitative features of the relaxation of the first layer of most of the surfaces studied. Similar overestimates of 3-4% for  $\Delta d_{12}$  (%) can be seen as well as the underestimate of  $\Delta d_{23}$  (%).

For the Cu system in table V, CEM again describes the qualitative features of the first layer relaxation except for the small relaxation of the (311) surface. The much smaller value of  $\Delta d_{12}$  (%) for Cu(311) than Ni(311) is quite surprising given the very similar results for the (110) face. One might speculate that a small in-plane reconstruction occurs in the Cu(311) surface which eliminates the driving force for a large contraction.

For the Rh, Pd and Ag systems in table VI, CEM is much more quantitatively accurate, with the glaring exceptions of the Rh(100) and Pd(100) surfaces. Possible reasons for this disagreement are discussed in the next section.

Let us summarize the comparisons in tables III-VI. We find larger first layer contractions than experiment for most surfaces, especially the low-index planes of Ni and Cu. We also find that the first layer of the Al(111), Pd(100) and Rh(100) surfaces contracts while the experiments find expansions. In addition, in every case where experiments find relaxation past the second layer, CEM underestimates the extent of the relaxation of the second layer. Often experiments find relaxation of the third and fourth layers as well, while the CEM method finds negligible relaxation

past the second layer.

Comparison of CEM and other effective medium type methods indicates some interesting effects. The MD/MC-CEM results show the same general trends as those of CEM but find consistently less surface relaxation. The best agreement between the two is found for Al because  $\Delta G$  in Eq. (6) is less important for this nearly free electron metal than for the transition metals. While MD/MC-CEM values are generally in better quantitative agreement with experiment than CEM, this is merely fortuitous as discussed in the next section of this paper.

EM relaxation results, which are only available for Al, show good agreement with CEM and excellent agreement with MD/MC-CEM values, respectively. Accordingly, EM does not find a first layer expansion of the Al(111) surface.

Similarly, EAM does not find first layer expansions of the Al(111), Pd(100) and Rh(100) surfaces, in agreement with CEM and MD/MC-CEM but in disagreement with experiment. Furthermore, the EAM generally finds greater relaxation of the second layer than CEM but does not usually agree in the magnitude of relaxation reported by experiment. The EAM predictions are rather good for Ni and Cu, and clearly better than CEM for Cu. In contrast, the EAM results for Pd are much worse than for the Ni system, and clearly inferior to the CEM ones. The EAM shows excellent agreement with CEM for Ag.

To provide a further point of reference, note that both the LJ and Morse potentials predict expansions for all the low-index Cu surfaces in table II, with the Cu(110) surface having the largest expansion. This is blatantly incorrect and arises because the LJ and Morse potentials have minima at 2.62 Å and 2.87 Å, respectively.

At a Cu-Cu separation equal to its nearest neighbor distance of 2.55 Å both potentials are slightly contracted inside the two-body minimum. Thus, at the surface, the atoms in the first surface layer expand to larger separations from the second layer atoms. Since the Morse potential equilibrium distance is significantly larger than that of the LJ potential, larger first layer expansions are found for the former. In addition, the universality of the LJ potential implies that all metals modeled by this two-body potential will be predicted to expand at the surface. One can thus conclude that simple two-body potentials cannot even describe metal surfaces qualitatively.

The fact that many of the experimental relaxation results were obtained at temperatures between  $\approx 90\text{K}$  and room temperature prompted us to study the effects of temperature on the relaxation of the first layer of the low-index Cu surfaces. This was done using molecular dynamics to initialize the surface at the desired temperature, calculating energies and forces via the MD/MC-CEM theory. In all cases, warming the surface led to a negligible decrease in  $\Delta d_{12}$  (%) since the surface and bulk expanded by essentially equal amounts. This agrees with some experiments that have examined the temperature dependence of metal surface relaxation<sup>32,56</sup>.

Lastly, we compare the surface energies and relaxations calculated using two different embedding functions: the present LMTO based one,  $\Delta E_{\text{LMTO}}(A_i; n_i)$ , and the previous one developed using experimental cohesive energies and diatomic binding curves,  $\Delta E_{\text{C}}(A_i; n_i)$ . Tables I and VII show that the surface energies are about 5-10% smaller for Al, Ni and Cu using the latter type of embedding function. For Rh, Pd

and Ag, the surface energies are nearly unchanged. Many more changes in the surface energy are within the error limits for the calculation using  $\Delta F_C(A_i; n_i)$ , as indicated by the brackets in table VII, which make surface relaxation results less reliable.

Table VIII compares the LMTO and semi-empirical relaxation data. There is good qualitative agreement between the two sets of results. We can be more quantitative by comparison to the experimental values. The Al system is described better for the (111) and (100) faces by  $\Delta E_C(\text{Al}; n)$ , the (110) and (311) by  $\Delta E_{\text{LMTO}}(\text{Al}; n)$ , and the (331) and (210) equally by either. The Ni system is described better for the (111), (100) and (110) faces by  $\Delta E_C(\text{Ni}; n)$ , and the (311) by  $\Delta E_{\text{LMTO}}(\text{Ni}; n)$ . The Cu system is described better for the (111), (100), (110) and (311) faces by  $\Delta E_C(\text{Cu}; n)$ . For all eight known results on the Rh, Pd and Ag systems both functions predict experimental values equally well. Hence, it is mainly the Cu system that would seem to indicate the new LMTO embedding functions do not describe the surface region as well as the previous semi-empirical values. However, one should note that not much relaxation is observed past the first layer for any of the surfaces studied using either embedding function.

At this point there is no overwhelming reason to choose one embedding function over another for CEM. The relaxation results are roughly equivalent as described above, while the surface energies are slightly better with  $\Delta E_{\text{LMTO}}$ . For MD/MC-CEM, another reason is that the number of surfaces where the change in surface energy with relaxation is within the error limits is decreased using the LMTO embedding function. In addition, due to a fortuitous accident that we discuss

below, the MD/MC-CEM results for the first layer agree with experiment quite respectably when the LMTO embedding functions are used. Thus, a realistic description of these surfaces in a molecular dynamics or monte-carlo simulation should use the LMTO embedding function.

## DISCUSSION AND CONCLUSIONS

From the results presented in the previous section, we conclude that all of the effective medium type methods compared here show good qualitative agreement with each other and conflict with experiment on some aspects of surface relaxation. This is an important point. If the experiments are correct, there are some inherent features of the effective medium type theory that is unable to reproduce some of the experimentally observed phenomena, namely expansions of the first layer of some close-packed surfaces and significant relaxation below the second layer. Also, the lack of consistency between the effective medium type predictions and the experimental values indicates some inherent failings.

It is worthwhile to question the experimental results that indicate expansions of the first layer. In Ref. 66 it was hypothesized that the presence of interstitial hydrogen or a possible difference in magnetic moment between the Pd(100) surface and bulk might be the cause of the experimentally observed expansion of the first layer of Pd(100). In addition, Feibelman et. al.<sup>11</sup> postulated that undetected adsorbed hydrogen is responsible for the experimental results for Rh(100), since their SCF-LD calculations find a 5.1% contraction of the first layer of that surface. The ability of Pd to absorb H raises questions about the expansion of the Pd(100) surface, especially since the trend for increasing contraction in the order (111)→(100)→(110) is not obeyed. Therefore, it should be kept in mind that the observed first layer expansions in many of the surfaces *might* be related to some experimental conditions that are not reproduced theoretically. On the other hand, recent DFT-LDA

calculations performed by Hennig et. al.<sup>75</sup> reproduce the unusual surface relaxation of Pd(100) and Rh(100). The unconventional behavior of these surfaces is theorized to result from a competition between charge-density smoothing and the bonding/antibonding character of the d-derived states. More work needs to be done to investigate this matter. Nevertheless, at this time, we believe that the Al(111) experimental results describe the clean surface and these do indicate some error in the effective medium theories.

For the Al(111), Al(100) and Ni(110) surfaces, we have analyzed the individual energy components in the CEM method as displayed in Figs. 4 and 5. These include the kinetic-exchange-correlation term ( $\Delta G$ ), the sum of the coulomb correction and the embedding energy, and the surface energy. These figures illustrate four significant features of surface relaxation.

First, very small energy changes on the order of  $0.01 \text{ J/m}^2$  ( $0.0002 \text{ eV/bohr}^2$ ) determine interlayer relaxation. Since all effective medium type theories are parameterized from bulk information (e.g. the LMTO calculated cohesive binding curve), considerable caution must be used in accepting the results of relaxation studies.

Second, and related to the above small energy changes, the relaxation of the first layer is *very* sensitive to slight changes in the embedding energies. Fig. 5 illustrates how the sum of the embedding and coulomb energies rises less sharply for the LMTO than covalent embedding functions. This is a direct reflection of the steeper  $\Delta E_{\text{LMTO}}(\text{Ni};n)$  vs.  $n$  curve as compared to  $\Delta E_{\text{C}}(\text{Ni};n)$  vs.  $n$ . The faster rising variation in the latter results in a difference of nearly  $0.1 \text{ J/m}^2$  ( $0.002 \text{ eV/bohr}^2$ ) when

the first layer is contracted by 13%.

Third, the kinetic-exchange-correlation energy plays an active role in determining relaxation. Indeed, at large first layer contractions this term begins to dominate the surface energy for Al(111) and Al(110) in Fig. 4.

Fourth, the qualitative difference in the relaxation of closed and open faces is caused by all the energy components. Fig. 4a shows that for the Al(111) surface when the first layer expands, the sum of the coulomb and embedding energies increases due to the fact that the embedding energy decreases more slowly than the coulomb energy increases.  $\Delta G$  decreases but not enough to lead to an expansion. Once the first layer starts to contract, however, the sum of the embedding and coulomb energies decreases while  $\Delta G$  increases, leading to a small contraction. For the Al(110) surface in Fig. 4b,  $\Delta G$  increases more slowly with contraction and the sum of the embedding and coulomb energies decreases more quickly, leading to large contractions.

The last point raises an important question: how can effective medium type theories that do not explicitly calculate the kinetic-exchange-correlation energy term, such as MD/MC-CEM and EAM, obtain accurate relaxation results? For the MD/MC-CEM method, it is due to cancellation of errors. In particular, the  $\Delta G$  term for a *bulk* atom is included in the CEM embedding energy to get the MD/MC-CEM effective embedding energy. This bulk  $\Delta G$  value is larger than the actual  $\Delta G$  term at the surface, thus incorrectly raising the embedding plus correction energy at the surface. Moreover,  $\Delta F_{\text{LMTO}}$  rises more sharply than  $\Delta E_{\text{LMTO}}$  and thus leads to smaller contractions in the MD/MC-CEM theory. The better agreement with experimental

values is simply fortuitous. Hence, finding agreement with experiment does not say *anything* about how inherently good the theory is. This is useful to know, since it allows us to explore the limitations of a good effective medium type technique.

In general, it seems that effective medium type methods are poor tools to use to study surface relaxation phenomena since these depend on small energy changes. This causes great sensitivity in the method to any errors in the embedding functions, and even could lead to sensitivity to the use of additive atomic electron densities (as described later). On the other hand, effective medium type methods when properly formulated can be quite useful for finding surface energies for *specific* surfaces. This information is not available from experimental data which utilize polycrystalline samples<sup>28,29</sup>. These apparently contradictory statements arise because the magnitude of the embedding energy curve determines the surface energy while the variation (e.g. slope) in the embedding energy curve determines the surface relaxation. The latter is much more difficult to predict accurately and consistently.

From the above, it is clear that extreme care must be used in determining the embedding curves. The LMTO embedding functions are preferable to the covalent ones because of the presence of data points throughout the surface region in the former and the significant extrapolation in the latter. Even better embedding functions could be made using a more exact method than LMTO for finding very reliable cohesive energy curves.

As a final point, we should mention that in previous CEM relaxation calculations, reasonable second and third layer relaxations were predicted<sup>19</sup>. The major difference between the previous and present calculations involves the atomic

electron densities. An even tempered gaussian basis<sup>76</sup> is used to fit to the HF atomic electron density for computational speed. In Ref. 19, the tails of the gaussian densities were slightly larger and of longer range than the HF densities. Using a better fitting procedure and more basis functions, we improved the fit to the HF density for the present calculations. This new density produces the smaller second layer relaxations observed here. The previous fit *unintentionally* mimicked the delocalization of electron density in the solid, and thus led to larger overlaps in Eq. (2) and an increased sensitivity of the second layer to the contraction of the first layer. We conclude that surface relaxation is too sensitive to the deviation of the electron density between surface and bulk atoms to allow for any method using simple superposition of electron densities to be accurate. In other words, electron density rearrangement must be included to predict surface relaxation but not surface energy.

## APPENDIX

We outline the LMTO method and show exactly how it was used to generate the cohesive energy curves. Briefly, the atomic charge densities are calculated using a Hartree-Fock-Dirac-Slater program by Desclaux which uses various local-density approximations.<sup>25</sup> Canonical LMTO structure constants and some structure factors are calculated for the chosen lattice type, in this case FCC. Next, the electronic structure of the material is calculated by LMTO, and the state densities are found based on the LMTO energy bands. Finally, the self consistent solution of the local-density one-electron Schrodinger equation is found through the canonical scaling principle, thus yielding the total energy of the system. The independently varied parameter in the calculations is the Wigner-Seitz radius of the lattice.

The above procedure yields the total energy per atom as a function of the Wigner-Seitz radius. Because the LMTO method is inaccurate for isolated atoms, the cohesive energy was obtained from experimental data by shifting the minimum of the LMTO generated energy curve to match the experimental value. We have also forced the LMTO equilibrium lattice constant to agree exactly with the experimental value by simple subtraction of the difference from all LMTO calculated values. Since the raw LMTO value is within 1% of the experimental one for every system considered here, this is an insignificant shift. The raw LMTO results are thus shifted in energy and lattice constant to agree with the experimental data. No further transformation of the LMTO data is done.

To increase the accessibility of the results to others, we have devised a

convenient Chebyshev representation of the cohesive energy variation which enables the reader to generate the cohesive energy for all lattice constants from 10% contraction to an infinite expansion.

To see how this is done, assume the existence of the shifted LMTO data:  $\{S_i, \Delta E_{\text{coh}}(S_i), i=1, \dots, N_{\text{calc}}\}$ , where  $S_i$  is the Wigner-Seitz radius,  $\Delta E_{\text{coh}}(S_i)$  is the cohesive energy at the appropriate radius, and  $N_{\text{calc}}$  is the number of calculated values. These are represented in the formula:

$$\Delta E_{\text{coh}}(S) = \sum_{k=0}^N c_k T_k(-1 + 2\exp[-\alpha(V - V_{\text{min}})]) \quad (9)$$

where  $V (=4\pi S^3/3)$  is the volume of the Wigner-Seitz cell,  $V_{\text{min}} (=4\pi S_{\text{min}}^3/3)$  is the volume of the smallest Wigner-Seitz cell, and  $T_k$  is the Chebyshev polynomial of order  $k$ . The relationship between the lattice constant and Wigner-Seitz radius for an FCC solid,  $4\pi S^3/3 = a^3/4$ , can be used to transform the data in terms of the lattice constant.

An iterative fitting procedure is used:

1. specify the number of polynomials,  $N$ , and an initial value for  $\alpha$ ;
2. determine the expansion coefficients,  $c_k$ , by weighted linear least squares fitting to the set of LMTO data,  $\{\Delta E_{\text{coh}}(S_i)\}$ ; the weights are  $w_i = 1/\Delta E_{\text{coh}}(S_i)$ , which is midway between unweighted and relative least squares fitting;
3. vary  $\alpha$  and repeat step 2 until the sum of square residuals is minimized.

This yields the best least squares fit for a given polynomial expansion. To determine the number of polynomials, we increase  $N$  until the sum of square residuals levels off

and/or the fit represents the data points to within the estimated accuracy of the data,  $\pm 0.001$  eV.

A sample result of the above procedure is shown in Fig. 6 for Ni. The use of  $N=5$  leads to an extremely accurate representation. For convenience, all coefficients (including  $\alpha$ ), equilibrium constants and cohesive energies are listed in table IX for all the FCC metals for which LMTO embedding functions were constructed.

## ACKNOWLEDGEMENTS

This work was supported by NSF grants CHE-8609832 and CHE-8921099. All calculations were performed on the Silicon Graphics 4D/380S purchased by an NSF instrumentation grant. One of the authors (M.S.S.) also acknowledges the support of the Alworth Memorial Foundation.

**REFERENCES**

1. F. Jona and P. M. Marcus, in *The Structure of Surfaces II*, 90-99, edited by J. F. van der Veen and M. A. Van Hove (Springer, New York, 1987).
2. J. Ihm and D. Joannopoulos, *Phys. Rev. B* **23**, 4429 (1982).
3. C. L. Fu, S. Ohnishi, E. Wimmer, and A. J. Freeman, *Phys. Rev. Lett.* **53**, 675 (1984).
4. K. M. Ho and K. P. Bohnen, *Phys. Rev. B* **32**, 3446 (1985).
5. C. L. Fu, A. J. Freeman, E. Wimmer, and M. Weinert, *Phys. Rev. Lett.* **54**, 2261 (1985).
6. D. Singh, S. H. Wei, and H. Krakauer, *Phys. Rev. Lett.* **57**, 3292 (1986).
7. A. Fasolino and E. Tosatti, *Phys. Rev. B* **35**, 4264 (1987).
8. K. P. Bohnen and K. M. Ho, *Surf. Sci.* **207**, 105 (1988).
9. X. W. Wang, C. T. Chan, K. M. Ho, and W. Weber, *Phys. Rev. Lett.* **60**, 2066 (1988).
10. N. Takeuchi, C. T. Chan, and K. M. Ho, *Phys. Rev. Lett.* **63**, 1273 (1989).
11. P. J. Feibelman and D. R. Hamann, *Surf. Sci.* **234**, 377 (1990).
12. M. S. Daw and M. I. Baskes, *Phys. Rev. B* **29**, 6443 (1984).
13. S. M. Foiles, M. I. Baskes and M. S. Daw, *Phys. Rev. B* **33**, 7983 (1986).
14. T. Ning, Q. Yu and Y. Ye, *Surf. Sci.* **206**, L857 (1988).
15. M. S. Daw, *Phys. Rev. B* **39**, 7441 (1989).
16. K. W. Jacobsen, J. K. Norskov and M. J. Puska, *Phys. Rev. B* **35**, 7423 (1987).

17. K. W. Jacobsen and J. K. Norskov, *Phys. Rev. Lett.* **59**, 2764 (1987).
18. K. W. Jacobsen and J. K. Norskov, *Phys. Rev. Lett.* **60**, 2496 (1988).
19. T. J. Raeker and A. E. DePristo, *Phys. Rev. B* **39**, 9967 (1989).
20. a) J. D. Kress and A. E. DePristo, *J. Chem. Phys.* **87**, 4700 (1987);  
b) J. D. Kress and A. E. DePristo, *J. Chem. Phys.* **88**, 2596 (1988).
21. J. D. Kress, M. S. Stave and A. E. DePristo, *J. Phys. Chem.* **93** 1556 (1989).
22. M. S. Stave, D. E. Sanders, T. J. Raeker and A. E. DePristo, *J. Chem. Phys.* **93**, 4413 (1990).
23. T. J. Raeker and A. E. DePristo, *Int. Rev. Phys. Chem.* **10**, 1 (1991).
24. CEM theory determines explicit corrections to this zero'th order model by considering the inhomogeneous electron density of the real atoms in the system. The interested reader is encouraged to refer to a series of papers<sup>19-22</sup> dealing with the derivation and various applications of the method and a review<sup>23</sup> that compares it to other effective medium type techniques. A brief overview of the theory is also provided in section II.
25. H. L. Skriver, *The LMTO Method* (Springer-Verlag, New York, 1984).
26. See Refs. 19, 22, and 23 for details concerning the specific kinetic, exchange, and correlation functionals used.
27. This procedure used a Morse expansion of the cohesive energy in the lattice constant, valid only for very small contractions and expansions of  $\pm 5\%$ . This is directly analogous to the LMTO generated values here but with a much smaller lattice variation. Thus, it also used the diatomic binding curve for  $\text{Cu}_2$  to determine the low density values of the embedding function. The

reader should consult Refs. 19, and 21-23 for more details.

28. L. Z. Mezey and J. Giber, *Jap. J. App. Phys.* **21**, 1569 (1982).
29. W. R. Tyson and W. A. Miller, *Surf. Sci.* **62**, 267 (1977).
30. D. Wolf, *Surf. Sci.* **226**, 389 (1990).
31. H. B. Nielsen and D. L. Adams, *J. Phys. C* **15**, 615 (1982).
32. J. R. Noonan and H. L. Davis, *J. Vac. Sci. Technol. A* **8**, 2671 (1990).
33. F. Jona, D. Sondericker, and P. M. Marcus, *J. Phys. C* **13**, L155 (1980).
34. V. Martinez, F. Soria, M. C. Munoz, and J. L. Sacedon, *Surf. Sci.* **128**, 424 (1983).
35. M. Van Hove, S. Y. Tong, and N. Stoner, *Surf. Sci.* **54**, 259 (1976).
36. N. Masud, R. Baudoing, D. Aberdam, and C. Gaubert, *Surface Sci* **133**, 580 (1983).
37. D. L. Adams and C. S. Sorensen, *Surface Sci* **166**, 495 (1986).
38. J. R. Noonan and H. L. Davis, *Phys. Rev. B* **29**, 4349 (1984).
39. J. N. Anderson, H. B. Nielsen, L. Peterson, and D. L. Adams, *J. Phys. C* **17**, 173 (1984).
40. J. R. Noonan, H. L. Davis, and W. Erley, *Surf. Sci.* **152**, 142 (1985).
41. D. L. Adams, V. Jensen, X. F. Sun, and J. H. Vollesen, *Phys. Rev. B* **38**, 7913 (1988).
42. T. Narusawa, W. M. Gibson, and E. Tornqvist, *Phys. Rev. Lett.* **47**, 417 (1981).
43. W. Oed, H. Lindner, V. Starke, K. Heinz, K. Muller, and J. B. Pendry, *Surf. Sci.* **224**, 179 (1989).

44. J. W. M. Frenken, R. G. Smeenk, and J. F. van der Veen, *Surf. Sci.* **135**, 147 (1983).
45. J. W. M. Frenken, J. F. van der Veen, and G. Allen, *Phys. Rev. Lett.* **20**, 1876 (1983).
46. R. Feidenhans'l, J. E. Sorensen, and I. Stensgaard, *Surf. Sci.* **134**, 329 (1983).
47. Y. Gauthier, R. Baudoing, Y. Joly, G. Gaubert, and J. Rundgren, *J. Phys. C* **17**, 4547 (1984).
48. D. L. Adams, L. E. Petersen, and C. S. Sorensen, *J. Phys. C* **18**, 1753 (1985).
49. S. M. Yalisove, W. R. Graham, E. D. Adams, M. Copel, and T. Gustafsson, *Surf. Sci.* **171**, 400 (1986).
50. M. L. Xu and S. Y. Tong, *Phys. Rev. B* **31**, 6332 (1985).
51. D. L. Adams, T. W. Moore, and K. A. R. Mitchell, *Surf. Sci.* **149**, 407 (1985).
52. S. A. Lindgren, L. Wallden, J. Rundgren, and T. Westrin, *Phys. Rev. B* **29**, 576 (1984).
53. H. L. Davis and J. R. Noonan, *J. Vacuum Sci. Technol.* **20**, 842 (1982).
54. R. Mayer, C. S. Zhang, K. G. Lynn, W. E. Frieze, F. Jona, and P. M. Marcus, *Phys. Rev. B* **35**, 3102 (1987).
55. I. Stensgaard, R. Feidenhans'l, and J. E. Sorensen, *Surf. Sci.* **128**, 281 (1983).
56. J. Marcano, Y. Darici, H. Min, Y. Yin, and P. A. Montano, *Surf. Sci.* **217**, 1 (1989).
57. M. Copel, T. Gustafsson, W. R. Graham, and S. M. Yalisove, *Phys. Rev. B*

- 33, 8110 (1986).
58. D. L. Adams, H. B. Nielsen, and J. N. Andersen, *Surf. Sci.* **128** 294 (1983).
59. H. L. Davis and J. R. Noonan, *Surf. Sci.* **126**, 245 (1983).
60. P. R. Watson and K. A. R. Mitchell, *Surf. Sci.* **203**, 323 (1988).
61. S. Hengrasmee, K. A. R. Mitchell, P. R. Watson, and S. J. White, *Can. J. Phys.* **58**, 200 (1980).
62. W. Oed, B. Dotsch, L. Hammer, K. Heinz, K. Muller, *Surf. Sci.* **207**, 55 (1988).
63. W. Nichtl, N. Bickel, L. Hammer, K. Heinz, and K. Muller, *Surf. Sci.* **188**, L729 (1987).
64. Y. Kuk, L. C. Feldman, and P. J. Silverman, *Phys. Rev. Lett.* **50**, 511 (1983).
65. R. J. Behm, K. Christmann, G. Ertl, and M. A. Van Hove, *J. Chem. Phys.* **73**, 2984 (1980).
66. J. Quinn, Y. S. Li, D. Tian, H. Li, F. Jona, and P. M. Marcus, *Phys. Rev. B* **42**, 11348 (1990).
67. C. J. Barnes, M. Q. Ding, M. Lindroos, R. D. Diehl, and D. A. King, *Surf. Sci.* **162**, 59 (1985).
68. F. Soria, J. L. Sacedon, P. M. Echenique, and D. Titterington, *Surf. Sci.* **68**, 448 (1977).
69. R. J. Culbertson, L. C. Feldman, P. J. Silverman, and H. Boehm, *Phys. Rev. Lett.* **47**, 657 (1981).
70. H. Li, J. Quinn, Y. S. Li, D. Tian, F. Jona, and P. M. Marcus, *Phys. Rev. B* **43**, 7305 (1991).

71. J. R. Noonan and H. L. Davis, *Bull. Am. Phys. Soc.* **26**, 224, AP 4 (1981).
72. M. Lindroos, C. J. Barnes, M. Valden, and D. A. King, *Surf. Sci.* **218**, 269 (1989).
73. Y. Kuk and L. C. Feldman, *Phys. Rev. B* **30**, 5811 (1984).
74. E. Holub-Krappe, K. Horn, J. W. M. Frenken, R. L. Krams, and J. F. van der Veen, *Surf. Sci.* **188**, 335 (1987).
75. D. Hennig, M. Methfessel, S. Weber, and M. Scheffler, *Bull. Am. Phys. Soc.* **36**, 810, M12 2 (1991).
76. M. W. Schmidt and K. Ruedenberg, *J. Chem. Phys.* **76**, 3951 (1979).

**Table I:** Relaxed surface energies,  $\sigma$  ( $J/m^2$ ), calculated using the LMTO embedding functions.

face	Al	Ni	Cu	Rh	Pd	Ag	Method
111	1.20	2.08	1.51	2.37	1.63	[0.90]	CEM
	0.93	2.53	1.76	[2.73]	[1.89]	[1.02]	MD/MC-CEM
100	1.30	2.24	1.64	2.52	1.74	0.95	CEM
	1.02	[2.70]	1.91	[2.88]	[2.00]	[1.10]	MD/MC-CEM
331	1.37	2.36	1.72	-	-	-	CEM
	1.08	2.89	2.04	-	-	-	MD/MC-CEM
110	1.38	2.38	1.75	2.71	1.87	1.04	CEM
	1.10	2.90	2.08	3.12	2.18	1.22	MD/MC-CEM
311	1.38	2.39	1.75	-	-	-	CEM
	1.10	2.91	2.07	-	-	-	MD/MC-CEM
210	1.44	2.47	1.82	-	-	-	CEM
	1.15	3.01	2.17	-	-	-	MD/MC-CEM
	1.09	2.36	1.93	2.83	2.04	1.30	Expt. <sup>a</sup>
	0.94	1.77	1.58	2.12	1.38	1.05	Expt. <sup>b</sup>
	1.14	2.38	1.79	2.66	2.00	1.25	Expt. <sup>c</sup>
	1.15	2.49	2.04	2.94	2.17	1.38	Expt. <sup>d</sup>

<sup>a</sup> Experimental data on polycrystalline samples at 298K from Ref. 28.

<sup>b</sup> Experimental data on polycrystalline samples at the metal's melting point from Ref. 28.

<sup>c</sup> Experimental data on polycrystalline samples at the metal's melting point from Ref. 29.

<sup>d</sup> Experimental data extrapolated linearly to 0K using 298K data from Ref. 28 and melting point data from Ref. 28.

**Table II:** The percentage change in interlayer spacing and the relaxed surface energies for various interaction potentials.

face	$\Delta d_{12}$ (%)	$\Delta d_{23}$ (%)	$\sigma$ (J/m <sup>2</sup> )	Method [Ref.]
Cu 111	-4.6	+0.5	1.51	CEM
	-1.9	0.0	1.76	MD/MC-CEM
	+1.2	0.0	3.25	LJ
	+4.8	+1.2	4.03	Morse
	-2.5	-0.0	1.18	EAM [14]
Cu 100	-6.2	+0.5	1.63	CEM
	-2.6	-0.5	1.91	MD/MC-CEM
	+2.5	+0.5	3.39	LJ
	+9.8	+2.8	3.90	Morse
	-3.8	-0.5	1.37	EAM [14]
Cu 110	-15.0	+1.4	1.75	CEM
	-7.8	+1.1	2.08	MD/MC-CEM
	+3.5	+1.0	3.57	LJ
	+14.7	+3.7	4.08	Morse
	-8.7	+1.6	1.51	EAM [14]
		1.93	Expt. <sup>a</sup>	
		1.58	Expt. <sup>b</sup>	
		1.79	Expt. <sup>c</sup>	
		2.04	Expt. <sup>d</sup>	

<sup>a</sup> Experimental data on polycrystalline samples at 298K from Ref. 28.

<sup>b</sup> Experimental data on polycrystalline samples at the metal's melting point from Ref. 28.

<sup>c</sup> Experimental data on polycrystalline samples at the metal's melting point from Ref. 29.

<sup>d</sup> Experimental data extrapolated linearly to 0K using 298K data from Ref. 28 and melting point data from Ref. 28.

**Table III:** Percent relaxation of interlayer spacing for Al.

face	$\Delta d_{12}$ (%)	$\Delta d_{23}$ (%)	Method [Ref.]
111	-2.4	0.0	CEM <sup>a</sup>
	-1.8	0.0	MD/MC-CEM <sup>a</sup>
	-1	0	EM [16]
	-3.26	-1.70	EAM [14]
	+0.9±0.5		LEED <sup>b</sup> [31]
	+1.7±0.3	+0.5±0.7	LEED [32]
	+2.2±1.3		LEED [33]
	+3±2		LEED [34]
100	-3.2	0.0	CEM
	-2.3	0.0	MD/MC-CEM
	-3	0	EM [16]
	-4.90	-2.24	EAM [14]
	0		LEED [35], MEED [36]
331	-14.5	-2.4	CEM
	-9.7	-1.9	MD/MC-CEM
	-11.7±2.3	-4.1±3.1	LEED [37]
110	-10.0	+1.4	CEM
	-6.7	+0.5	MD/MC-CEM
	-7	+1	EM [16]
	-10.47	+3.64	EAM [14]
	-8.5±1.0	+5.5±1.1	LEED [38]
	-8.6±0.8	+5.0±1.1	LEED [39]
311	-13.8	+2.4	CEM
	-9.1	+1.2	MD/MC-CEM
	-13.3±1.0	+8.8±1.5	LEED [40]
210	-19.7	-1.0	CEM
	-13.8	-1.0	MD/MC-CEM
	-16±2	-1±3	LEED [41]

<sup>a</sup> The LMTO embedding function was used.

<sup>b</sup> Low energy electron diffraction.

**Table IV:** Percent relaxation of interlayer spacing for Ni.

face	$\Delta d_{12}$ (%)	$\Delta d_{23}$ (%)	Method [Ref.]
111	-4.1	+0.5	CEM <sup>a</sup>
	-1.2	0.0	MD/MC-CEM <sup>a</sup>
	-1.85	-0.04	EAM [14]
	0.0		HEIS [42]
100	-5.2	+0.5	CEM
	[-1.0	0.0]	MD/MC-CEM
	-3.04	-0.35	EAM [14]
	-1 $\pm$ 1	0 $\pm$ 1	LEED [43]
	-3.2 $\pm$ 0.5		RBS [44], RBS [45]
331	-16.6	-0.5	CEM
	-7.9	-0.5	MD/MC-CEM
110	-12.3	0.0	CEM
	-4.1	+0.5	MD/MC-CEM
	-7.01	+1.84	EAM [14]
	-4.8 $\pm$ 1.7	+2.4 $\pm$ 1.2	HEIS [46]
	-8.4 $\pm$ 0.8	+3.1 $\pm$ 1.0	LEED [47]
	-8.7 $\pm$ 0.5	+3.0 $\pm$ 0.6	LEED [48]
	-9.0 $\pm$ 1.0	+3.5 $\pm$ 1.5	MEIS [49]
	-9.8 $\pm$ 1.8	+3.8 $\pm$ 1.8	LEED [50]
311	-15.5	+0.5	CEM
	-6.9	+1.8	MD/MC-CEM
	-15.9 $\pm$ 1.0	+4.1 $\pm$ 1.5	LEED [51]
210	-19.9	-4.9	CEM
	-10.0	+0.5	MD/MC-CEM

<sup>a</sup> The LMTO embedding function was used.

**Table V:** Percent relaxation of interlayer spacing for Cu.

face	$\Delta d_{12}$ (%)	$\Delta d_{23}$ (%)	Method [Ref.]
111	-4.6	+0.5	CEM <sup>a</sup>
	-1.9	0.0	MD/MC-CEM <sup>a</sup>
	-2.48	-0.04	EAM [14]
	-0.7±0.5		LEED [52]
100	-6.2	+0.5	CEM
	-2.6	-0.5	MD/MC-CEM
	-3.79	-0.54	EAM [14]
	-1.10±0.40	+1.70±0.60	LEED [53]
	-2.1±1.7	+0.45±1.7	LEED,LEPD [54]
331	-18.9	-5.7	CEM
	-11.9	-1.4	MD/MC-CEM
110	-15.0	+1.4	CEM
	-7.8	+1.1	MD/MC-CEM
	-8.73	+1.56	EAM [14]
	-5.3±1.6	+3.3±1.6	HEIS [55]
	-6.7±2	+4.2±2	LEED [56]
	-7.5±1.5	+2.5±1.5	MEIS [57]
	-8.5±0.6	+2.3±0.8	LEED [58]
	-10.0	+1.90	LEED [59] <sup>b</sup>
	-7.90	+2.40	LEED [59] <sup>b</sup>
	-9.50	+2.60	LEED [59] <sup>b</sup>
311	-18.6	+1.1	CEM
	-11.0	+2.0	MD/MC-CEM
	-7.3	+3.7	LEED [60]
210	-25.3	-4.7	CEM
	-17.5	0.0	MD/MC-CEM

<sup>a</sup> The LMTO embedding function was used.

<sup>b</sup> Results of different R-factor analysis on the same set of LEED data.

**Table VI:** Percent relaxation of interlayer spacing for Rh, Pd and Ag.

Atom	face	$\Delta d_{12}$ (%)	$\Delta d_{23}$ (%)	Method [Ref.]
Rh	111	-2.3	0.0	CEM <sup>a</sup>
		[-1.0	0.0]	MD/MC-CEM <sup>a</sup>
		-0.7±0.8		LEED [61] <sup>b</sup>
		-1.6±0.8		LEED [61] <sup>b</sup>
	100	-3.2	0.0	CEM
		[0.0	0.0]	MD/MC-CEM
		+0.5±2		LEED [62]
		+0.5±1.2		LEED [61] <sup>b</sup>
		+1.0±0.9		LEED [61] <sup>b</sup>
110	-7.8	+0.5	CEM	
	-4.2	+0.5	MD/MC-CEM	
	-2.5±1.2		LEED [61] <sup>b</sup>	
	-3.3±1.5		LEED [61] <sup>b</sup>	
	-6.9±1.0	+1.9±1.0	LEED [63]	
Pd	111	-2.2	0.0	CEM
		[-0.5	0.0]	MD/MC-CEM
		-3.17	+0.27	EAM [14]
		0.0		HEIS,LEED,AES[64]
	100	-2.8	0.0	CEM
		[0.0	0.0]	MD/MC-CEM
		-4.94	+0.17	EAM [14]
		+2.5±2.5		LEED [65]
		+3	-1	LEED [66]
110	-7.6	-0.5	CEM	
	-3.6	+0.5	MD/MC-CEM	
	-11.20	+2.49	EAM [14]	
	-6±2	+1±2	LEED [67]	
Ag	111	[-1.2	+0.5]	CEM
		[0.0	0.0]	MD/MC-CEM
		-1.86	+0.13	EAM [14]
		0		LEED[68],HEIS [69]

**Table VI:** (continued)

100	-3.1	0.0	CEM
	[0.0	0.0]	MD/MC-CEM
	-2.99	-0.01	EAM [14]
	0±1.5		LEED[70]
110	-7.3	+0.5	CEM
	-4.4	+1.0	MD/MC-CEM
	-6.87	+2.19	EAM [14]
	-5.7±1.5	+2.2±2.0	LEED [71]
	-7±2	+1±2	LEED [72]
	-7.8±2.5	+4.3±2.5	HEIS [73]
	-9.5±2	+6.0±2.5	RBS [74]

<sup>a</sup> The LMTO embedding function was used.

<sup>b</sup> Results of different R-factor analysis on the same set of LEED data.

**Table VII** Relaxed surface energies,  $\sigma$  ( $\text{J/m}^2$ ), calculated using the semi-empirical embedding functions.

face	Al	Ni	Cu	Rh	Pd	Ag	Method
111	[1.12]	1.95	1.41	2.39	1.65	0.94	CEM
	0.87	[2.37]	[1.63]	2.76	[1.91]	[1.08]	MD/MC-CEM
100	[1.19]	2.07	1.49	2.55	1.75	1.00	CEM
	0.95	[2.48]	[1.73]	[2.92]	[2.03]	[1.15]	MD/MC-CEM
331	1.27	2.21	1.59	-	-	-	CEM
	1.02	2.69	1.87	-	-	-	MD/MC-CEM
110	1.28	2.23	1.60	2.73	1.88	1.07	CEM
	1.05	[2.70]	[1.88]	3.15	2.20	1.25	MD/MC-CEM
311	1.28	2.24	1.61	-	-	-	CEM
	1.04	2.71	1.88	-	-	-	MD/MC-CEM
210	1.33	2.31	1.66	-	-	-	CEM
	1.10	2.81	1.96	-	-	-	MD/MC-CEM
	1.09	2.36	1.93	2.83	2.04	1.30	Expt. <sup>a</sup>
	0.94	1.77	1.58	2.12	1.38	1.05	Expt. <sup>b</sup>
	1.14	2.38	1.79	2.66	2.00	1.25	Expt. <sup>c</sup>
	1.15	2.49	2.04	2.94	2.17	1.38	Expt. <sup>d</sup>

<sup>a</sup> Experimental data on polycrystalline samples at 298K from Ref. 28.

<sup>b</sup> Experimental data on polycrystalline samples at the metal's melting point from Ref. 28.

<sup>c</sup> Experimental data on polycrystalline samples at the metal's melting point from Ref. 29.

<sup>d</sup> Experimental data extrapolated linearly to 0K using 298K data from Ref. 28 and melting point data from Ref. 28.

**Table VIII:** Percentage change in the interlayer spacing calculated using two different types of embedding functions.

	LMTO				Semi-empirical			
	CEM		MD/MC-CEM		CEM		MD/MC-CEM	
	$\Delta d_{12}(\%)$	$\Delta d_{23}(\%)$						
Al(111)	-2.4	0.0	-1.8	0.0	[0.0	0.0]	-1.0	+0.5
(100)	-3.2	0.0	-2.3	0.0	[0.0	0.0]	-1.8	+0.5
(331)	-14.5	-2.4	-9.7	-1.9	-9.6	+1.7	-11.9	+1.0
(110)	-10.0	+1.4	-6.7	+0.5	-4.4	+1.0	-6.9	+1.4
(311)	-13.8	+2.4	-9.1	+1.2	-7.8	+3.3	-10.4	+3.1
(210)	-19.7	-1.0	-13.8	-1.0	-13.8	+3.2	-18.9	+2.8
Ni(111)	-4.1	+0.5	-1.2	0.0	-2.6	0.0	[0.0	0.0]
(100)	-5.2	+0.5	[-1.0	0.0]	-3.2	0.0	[+1.2	0.0]
(331)	-16.6	-0.5	-7.9	-0.5	-13.6	-2.0	-6.4	+2.9
(110)	-12.3	0.0	-4.1	+0.5	-7.9	0.0	[-1.3	+0.5]
(311)	-15.5	+0.5	-6.9	+1.8	-11.4	+1.1	-4.3	+3.1
(210)	-19.9	-4.9	-10.0	-0.5	-16.3	-2.0	-9.2	+4.1
Cu(111)	-4.6	+0.5	-1.9	0.0	-2.3	+0.5	{0.0	0.0}
(100)	-6.2	+0.5	-2.6	-0.5	-2.6	0.0	[+1.0	0.0]
(331)	-18.9	-5.7	-11.9	-1.4	-12.3	-1.6	-5.7	+2.2
(110)	-15.0	+1.4	-7.8	+1.1	-7.1	0.0	[-1.4	+0.5]
(311)	-18.6	+1.1	-11.0	+2.0	-10.0	+1.0	-4.1	+2.6
(210)	-25.3	-4.7	-17.5	0.0	-14.9	-1.4	-8.6	+3.2
Rh(111)	-2.3	0.0	[-1.0	0.0]	-2.4	+0.5	-1.0	0.0
(100)	-3.2	0.0	[0.0	0.0]	-2.9	+0.5	[-0.5	0.0]
(110)	-7.8	+0.5	-4.2	+0.5	-7.9	+0.5	-3.8	0.0
Pd(111)	-2.2	0.0	[-0.5	0.0]	-2.2	+0.5	[-0.5	0.0]
(100)	-2.8	0.0	[0.0	0.0]	-2.8	+0.5	[0.0	0.0]
(110)	-7.6	-0.5	-3.6	+0.5	-7.1	+0.5	-3.6	+0.5
Ag(111)	[-1.2	+0.5]	[0.0	0.0]	-2.1	+0.5	[-0.5	0.0]
(100)	-3.1	0.0	[0.0	0.0]	-2.8	+0.5	[0.0	0.0]
(110)	-7.3	+0.5	-4.4	+1.0	-6.8	0.0	-2.7	0.0

**Table IX:** Parameters determined for the expansion in Eq. (9) for various metals.

Value	Al	Ni	Cu	Rh
$\alpha$ ( $\text{\AA}^{-3}$ )	9.0E-3	1.9E-2	1.1E-2	1.1E-2
$c_0$ (eV)	0.11432518E+1	0.14134208E+1	0.14571759E+1	0.24165984E+1
$c_1$ (eV)	-0.15184879E+1	-0.15744062E+1	-0.17636163E+1	-0.15545836E+1
$c_2$ (eV)	0.57960347E+0	0.11938613E+1	0.32681219E+0	0.19881543E+1
$c_3$ (eV)	-0.25339627E-1	-0.91979019E-1	0.20598476E+0	0.48745918E+0
$c_4$ (eV)	0.10046380E+0	0.11005449E+0	0.98421562E-1	0.23260850E+0
$c_5$ (eV)	-0.22854350E-1	-0.56276294E-1	-0.49960518E-1	0.94609578E-3
$c_6$ (eV)	-	-	-	0.46461025E-1
$c_7$ (eV)	-	-	-	-
$c_8$ (eV)	-	-	-	-
$S_{\min}$ ( $\text{\AA}$ )	1.42445	1.23805	1.26970	1.33652
$S_0$ ( $\text{\AA}$ )	1.58273	1.37560	1.41077	1.48503
$\Delta E_{\text{coh}}(S_0)$ (eV)	-3.39	-4.44	-3.49	-5.75

Pd	Ag	Pt	Au
1.0E-2	1.5E-2	1.5E-2	1.6E-2
0.16681805E+1	0.85217445E+0	0.21618827E+1	0.12484934E+1
-0.10439296E+1	-0.52081826E+0	-0.71005576E+0	-0.12006080E+1
0.12793565E+1	0.91189961E+0	0.22439594E+1	0.11234482E+1
0.42785362E+0	-0.10233345E+0	-0.54158656E-1	-0.26519356E-1
0.22365501E+0	0.18965911E+0	0.25941877E+0	0.99011854E-1
-0.24143541E-1	-0.19843950E+0	-0.10786330E+0	-0.51440556E-1
0.78589146E-1	0.74632403E-1	0.17819474E+0	0.96887166E-2
-	-0.10003594E+0	-0.42240214E-2	-0.50792790E-1
-	-	0.12024458E+0	-
1.36817	1.43852	1.37873	1.43500
1.52019	1.59836	1.53192	1.59445
-3.89	-2.95	-5.84	-3.81

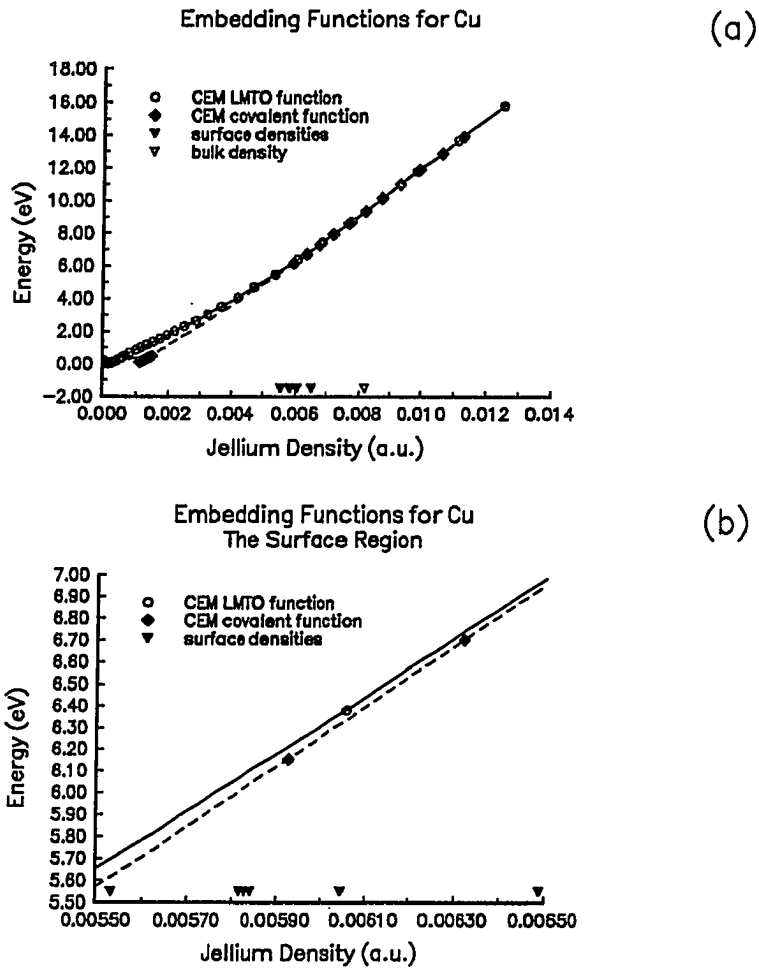


**Fig. 1:** A comparison of the CEM LMTO and covalent embedding functions for Cu a) over a large range of jellium densities and b) over the surface region only.

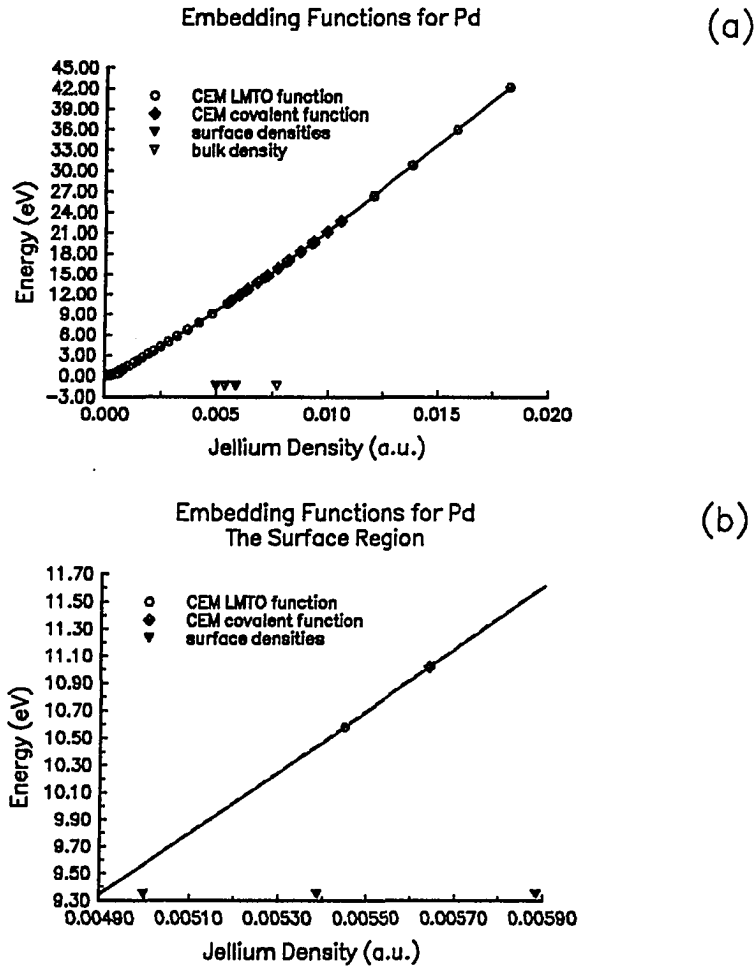


**Fig. 2:** A comparison of the CEM LMTO and covalent embedding functions for Pd a) over a large range of jellium densities and b) over the surface region only.

## LMTO Embedding Functions for Cu

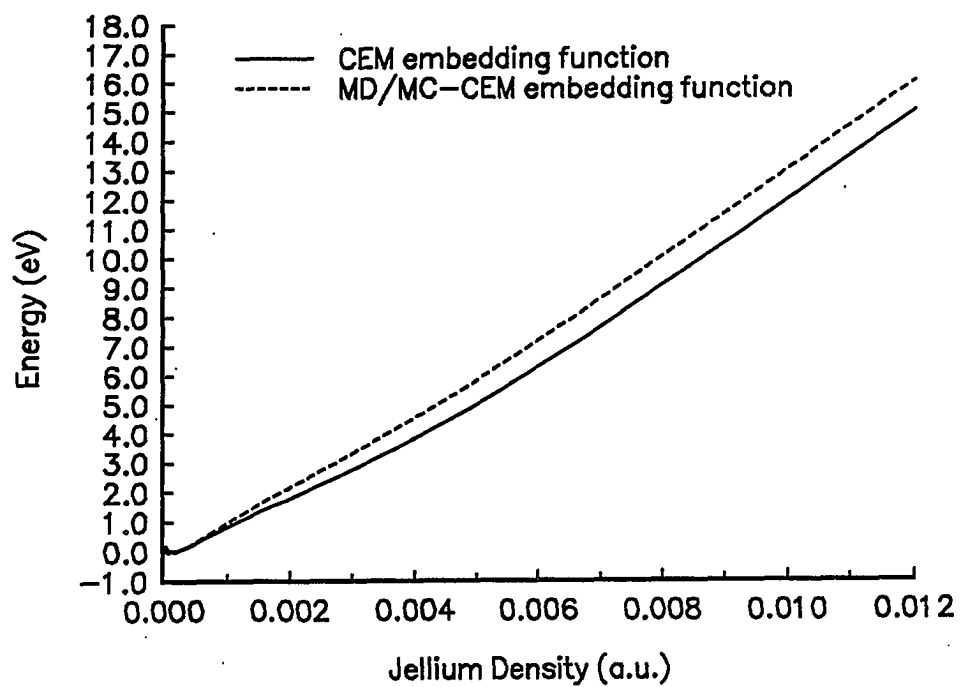


**Fig. 3:** A comparison of the LMTO CEM an MD/MC-CEM embedding functions for Cu.

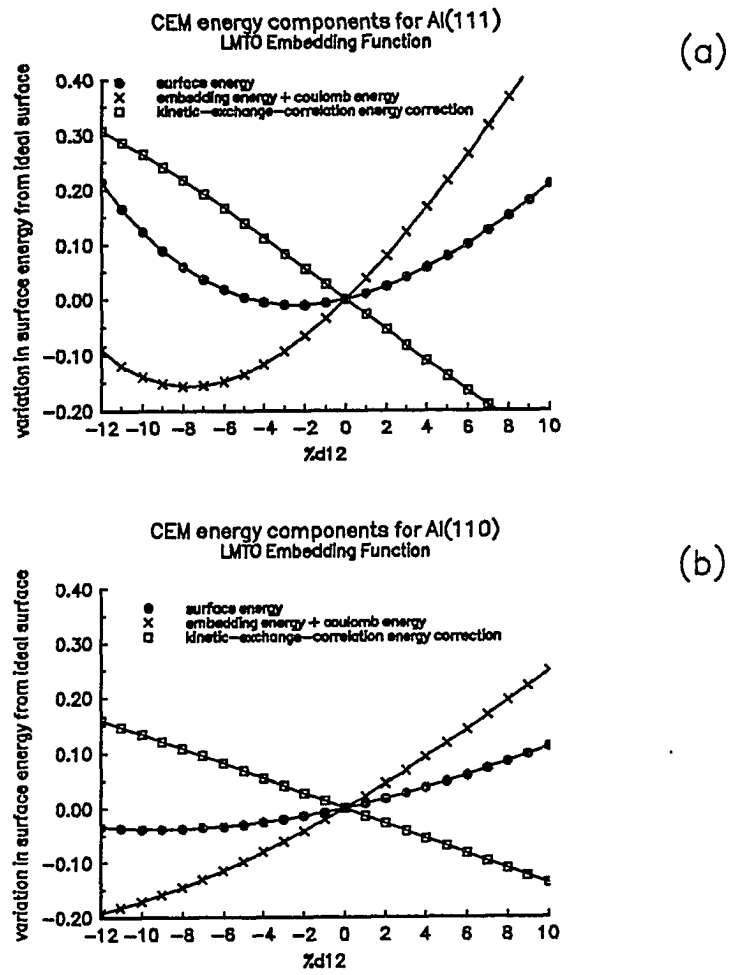


**Fig. 4:** The CEM energy components for a) Al(111) and b) Al(110) utilizing the LMT0 embedding energies. Energies are in  $\text{J/m}^2$ .

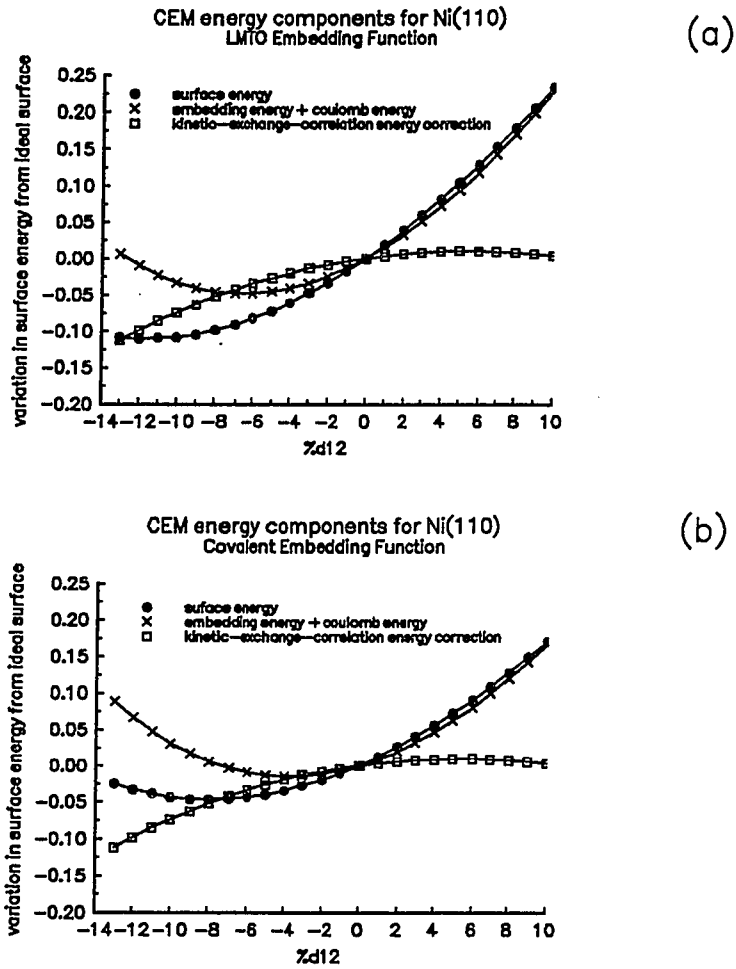


**Fig. 5:** A comparison of the CEM energy components for Ni(110) utilizing the a) LMT0 embedding energies and b) the semi-empirical embedding energies. Energies are in  $\text{J}/\text{m}^2$ .

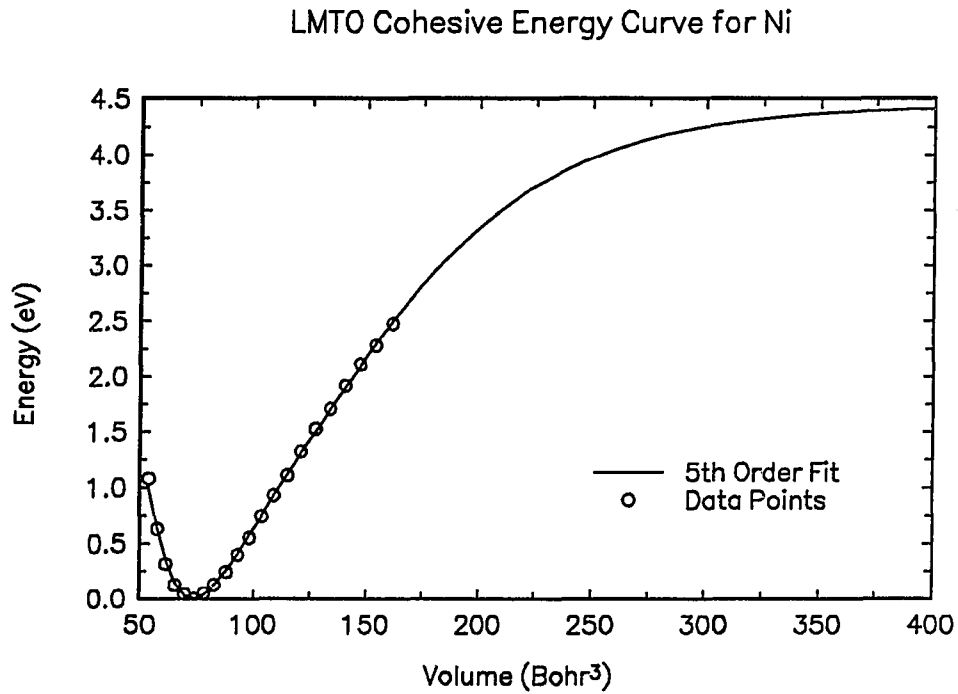


**Fig. 6:** The LMTO cohesive energy curve for Ni. The line is a fifth-order Chebyshev representations in Eq. (9) and the points are the LMTO calculated values.

PAPER 3. EXPLORATION OF APPROXIMATIONS OF THE  
KINETIC-EXCHANGE-CORRELATION ENERGY

EXPLORATION OF APPROXIMATIONS OF THE  
KINETIC-EXCHANGE-CORRELATION ENERGY

Susan B. Sinnott, Cynthia L. Kelchner and Andrew E. DePristo

Ames Laboratory - USDOE and

Department of Chemistry

Iowa State University

Ames, Iowa 50011

**ABSTRACT**

We present the results of our work to estimate the many-body kinetic-exchange-correlation energy with a two-body approximation. The approximation does not use any adjustable parameters or any functional form. Results of this approximation used within the corrected effective medium method in place of exact numerical integration are provided for Ni, Cu, Rh, Pd and Ag. Systems that are studied include diatomics, surfaces and the bulk lattice. Among the quantities calculated are surface energies, energies of formation for various bimetallic solids and the barriers and predicted mechanism of the diffusion of Cu on Cu(100). Finally, we discuss the validity of approximating a many-body energy with a two-body function.

## INTRODUCTION

The energy for a system of atoms,  $\{A_i, i=1, \dots, N\}$ , has two central components: the Coulomb,  $V_c$ , and kinetic-exchange-correlation,  $G(\{A_i\})$ , energies. The former is easy to understand since it is of classical electrostatic origin, and inexpensive to calculate since it involves pairwise (analytic) integrals. The latter is more complex and rather expensive to calculate since it requires the evaluation of a three dimensional numerical integral in which the integrand is dominated by the large densities near the nuclei<sup>1</sup>. While SCF density functional theories can do little but evaluate  $G(\{A_i\})$ , approximate density functional methods commonly approximate this term.

One approximate density functional theory, the corrected effective medium (CEM) method<sup>2-8</sup>, models the interaction of any one atom with all the other atoms in the system by that atom interacting with jellium. This is repeated for all the atoms in the system, and the total of all these atom-jellium interactions forms the zeroth order representation. The explicit corrections to this model are found by considering the inhomogeneous electron density of the real atoms in the system. The differences between the real and atom-in-jellium systems are determined non-self-consistently and involve Coulombic energies in addition to kinetic-exchange-correlation energies.

Of interest is the difference in the kinetic-exchange-correlation energy between the real system and the many atom-jellium systems,  $\Delta G$ . The simplest CEM method (for use in molecular dynamics (MD) and Monte Carlo (MC) calculations, with acronym MD/MC-CEM) treats this correction energy as a function of the jellium

density<sup>6</sup>. Other uncorrected and empirical effective medium type theories, such as the very successful embedded atom method<sup>9</sup> and the related "glue"<sup>10</sup> and Finnis-Sinclair<sup>11</sup> models, approximate this kinetic-exchange-correlation energy difference as a set of two-body functions.

The purpose of the present paper is to critically examine the validity of these approximations by comparing them to the exact numerical evaluation of  $\Delta G$ . This is a more rigorous approach than fitting a function to experimental data and assuming the method is universally applicable. The two simplifications we discuss each make the computational effort in the sophisticated many-body theories nearly equivalent to that of simple two-body techniques, such as the Lennard-Jones method. By contrast, direct evaluation of  $\Delta G$  requires from  $10^3$ - $10^4$  more effort.

We present our work to unambiguously determine a two-body representation of  $\Delta G$ . The resulting function has no adjustable parameters. We test the validity of the approximation by using it within the CEM theory to calculate many different quantities, including surface energies, surface relaxation, energies of formation for various bimetallic alloys and the diffusion of Cu on Cu(100). When the two-body approximation is used within the CEM theory we label the method CEM-Pair. No comparisons are made to experiment since from the standpoint of the approximation of the kinetic-exchange-correlation energy term, the only comparisons of interest are those between CEM-Pair, MD/MC-CEM and CEM. References to the exact values will in all cases mean those values calculated with the CEM theory using converged numerical integration of  $\Delta G$ .

The rest of this paper is organized as follows. Section II details how the two-

body approximation of the many-body kinetic-exchange-correlation energy difference is derived. Section III A examines differences between  $\Delta G$  calculated with the two approximate methods and the converged numerical values. Section III B describes the interaction energy results. Finally, section IV presents some conclusions.

## THEORY

The explicit form of the kinetic-exchange-correlation energy function is

$$G = \int [\tau(n^+(\vec{r})) + \tau(n^-(\vec{r})) + \epsilon_{xc}(n^+(\vec{r}), n^-(\vec{r}))] d\vec{r} \quad (1)$$

where  $\tau$  is the kinetic energy functional and  $\epsilon_{xc}$  is the exchange-correlation energy functional. An accurate Pade approximate representation of the full gradient expansion<sup>12</sup> is used for the kinetic energy functional. The local Dirac functional<sup>13</sup> is used for the exchange energy. The Gunnarrson-Lundqvist functional<sup>14</sup> is used for the correlation energy.

The quantity of interest is the difference in the kinetic-exchange-correlation energy between the many-atom system and the many atom-in-jellium systems,  $\Delta G$ :

$$\Delta G = G(\sum_i A_i) - \sum_i G(A_i) - \sum_i [G(A_i + n_i) - G(A_i) - G(n_i)] \quad (2)$$

where  $n_i$  is the jellium density. The first two terms on the right hand side (RHS) of the equation represent the difference between the system of interacting atoms and the individual atoms in the system. The third term on the RHS of the equation is the difference between the many atom-jellium systems and the many atom and many jellium systems.

If the system electron density,  $n(\{A_i\})$ , is significantly distorted from that of the sum of the individual atoms,  $\sum n(A_i)$ , the approximation of  $\Delta G$  by a sum of pairwise terms must break down. Since the current many-body theories all utilize the approximation of summed atomic densities, we shall also retain this assumption.

This provides a best case scenario for the approximation, since then

$$G(n(\{A_i\}))=G(\sum n(A_i)).$$

The results in this paper are not sensitive to the use of local vs. non-local functionals in Eq. (1). However, the results do depend strongly on the choice of jellium density,  $n_1$ , used in Eq. (2). This is determined<sup>8</sup> by setting  $|\Delta G| = 0$  and solving for  $n_1$ . This is not possible to do analytically since  $\Delta G$  is a complicated functional of  $n_1$ . The solution was found<sup>3</sup> by approximating the integrand in Eq. (1) with a quadratic in  $n^+$  and  $n^-$ , which are the atomic spin densities. Then setting  $|\Delta G| = 0$  leads to solutions which are independent of the coefficients of the fit. The most symmetric solution was chosen, which can be written as follows for spin-unpolarized atoms:

$$n_1 = \frac{1}{2Z_1} \sum_{j \neq 1} \int n(\vec{r} - \vec{R}_j) n(\vec{r} - \vec{R}_j) d\vec{r} \quad (3)$$

Note that the original functionals are used to calculate  $\Delta G$ ; the quadratic approximation to the integrand in Eq. (1) is only used to find the jellium density  $n_1$ . If the quadratic approximation *were* used as the integrand in Eq. (1) then Eq.(2) would be equal to zero.

It is the evaluation of  $\Delta G$  that is time consuming, and it is therefore this quantity that must be approximated to speed up CEM. Less computationally expensive techniques are necessary to simulate larger systems with molecular dynamics or Monte Carlo methods. Examples of systems of current interest are epitaxial growth on surfaces (about 5,000 atoms) and the study of bimetallic mixing

in clusters with over 1,000 atoms. To accommodate this need for a faster technique, the very simple theory, with acronym MD/MC-CEM, was developed<sup>6</sup> by assuming that  $\Delta G$  is a function of the jellium density:

$$\Delta G_{\text{MD/MC-CEM}} = \sum_i f_i(n_i) \quad (4)$$

To determine  $f_i(n_i)$  directly, consider a bulk system with one atom per unit cell. Then, every atom is equivalent and  $f_i(n_i)$  is found from the following expression:

$$\Delta G_{\text{WS}(i)} = f_i(n_i) \quad (5)$$

WS(i) indicates that the evaluation of the 3D integral used to calculate the kinetic-exchange-correlation energy of the many-atom system extends only over the Wigner-Seitz cell of atom "i". This estimate is much faster than the exact numerical integration of  $\Delta G$ . However, as we shall show in detail, it is a poor approximation of  $\Delta G$  at surfaces and, more importantly, in mixed metal systems. Thus there was incentive to derive a more flexible method of estimating  $\Delta G$  that would be free of these shortcomings.

The approach we have taken is to approximate  $\Delta G$  as follows:

$$\Delta G_{\text{pair}} = \frac{1}{2} \sum_{ij} g_2(R_{ij}) \quad (6)$$

where  $g_2(R_{ij})$  is a two-body function and  $R_{ij}$  is the interatomic distance between atoms  $A_i$  and  $A_j$ . We derive  $g_2(R)$  from the bulk system in an approach similar to that used earlier to find  $f_i(n_i)$ :

$$\Delta G_{\text{WS}(i)} = \frac{1}{2} \sum_{j \neq i} g_2(R_{ij}) \quad (7)$$

The value of  $\Delta G_{\text{WS}(i)}$  for any one lattice constant is thus approximated by a summation over the two-body functions from atoms in the first, second, third, etc. nearest neighbor shells. Changing the lattice constant provides all the needed information via the following procedure.

Denote the set of values of  $\Delta G_{\text{WS}(i)}$  at the lattice constants,  $\{a_\alpha, \alpha=1, \dots, N_{\text{lat}}\}$  by  $Y_\alpha$ . The number of first, second, third, ..., nearest neighbors is independent of the lattice constant with each integer denoted by  $\{M_\beta, \beta=1, \dots\}$ . All values of the internuclear separation are simply proportional to  $a_\alpha$  and for any neighbor can be written as  $R_{ij}(a_\alpha) = a_\alpha C_\beta$  where we have used the fact that  $j=j(\beta)$ . The approximation then becomes

$$Y_\alpha = \sum_{\beta} g_2(a_\alpha C_\beta) M_\beta \quad (8)$$

where the summation is over the number of neighbor shells.

Based upon Eq.(8), the following iterative technique is used to ascertain the two-body function

$$g_2^{(k+1)}(a_\alpha C_1) = \frac{2}{M_1} [Y_\alpha - \frac{1}{2} \sum_{\beta \neq 1} g_2^{(k)}(a_\alpha C_\beta) M_\beta] \quad (9)$$

where the superscript "(k)" identifies the iteration and where  $g_2^{(0)}=0$ . This scheme simply determines the function in the first neighbor shell from knowledge of  $Y_\alpha$  and then uses this for the other shells at the next iteration. Convergence is attained

when the function does not change between two consecutive iterations.

The  $k^{\text{th}}$  iterate,  $g_2^{(k)}$ , is fit to a quasi-Hermite spline as a function of inverse interatomic distance squared,  $R^{-2}$ . This enables evaluation of this function in the equation for the  $(k+1)^{\text{th}}$  iterate as well as in any other calculation since the distances are not the same for the  $\{a_\alpha C_1\}$  and  $\{a_\alpha C_\beta, \beta=2, \dots\}$ .

The value of  $g_2$  for Ni is shown in Fig. 1 as a function of the iteration number. The convergence is fast and uniform, which confirms the utility and generality of the direct numerical determination of the two-body functions. In order to determine the two-body function for a metal using Eq. (9), a range of bulk lattice constants must be chosen as well as the step size between lattice constants. For each of the systems studied, a step size of 0.05 bohr was used. Larger step sizes led to oscillations between points due to the fitting of the quasi-Hermite spline; smaller step sizes did not improve the fit of the approximation to  $\Delta G$ .

The physical limit for  $\Delta G$  is zero as the lattice constant increases and the interatomic interactions decrease. However, at very expanded lattice constants the kinetic energy functional used in Eq. (1) becomes the Weizacker form<sup>8</sup> because the value of  $\nabla n/n^{4/3}$  becomes large. This functional overestimates the kinetic energies, which makes  $\Delta G$  negative. Thus, the endpoint at large lattice constant (small  $R^{-2}$ ) is chosen so that  $\Delta G$  remains positive; beyond this endpoint the two-body function is set equal to zero. The small lattice endpoint (large  $R^{-2}$ ) is chosen to include all physically relevant regions. A linear extrapolation (in  $R^{-2}$ ) is used past the endpoint.

The two-body function between unlike atoms in a mixed metal (alloy) system is determined in a similar fashion. First,  $\Delta G$  is calculated for the basis set of atoms

in a bulk unit cell as a function of the bulk lattice constant. Then the interactions between like atoms are evaluated using the appropriate, previously constructed two-body functions and subtracted from the total  $\Delta G$ . This yields the contributions to  $\Delta G$  from pairs of unlike atoms only as a function of interatomic distance. From this point on the two-body function is determined as described above for the homogeneous atom system. In Fig. 2, we show the Ni-Ag and Ag-Ag two-body functions in addition to reproducing the Ni-Ni function from Fig. 1.

## RESULTS AND DISCUSSION

### Kinetic-Exchange-Correlation Energies

We illustrate the quantitative agreement of the two-body approximation with the exact  $\Delta G$  by showing the difference between  $\Delta G$  and  $\Delta G_{\text{pair}}$  for Ni in Fig.3a. The differences are the numerical inaccuracies associated with CEM-Pair and are negligible compared to  $\Delta G$  (see Fig. 3b). These figures and each of the remaining figures in this paper are plotted over the physically relevant region of  $0.75a_0$ - $1.10a_0$ , where  $a_0$  is the equilibrium bulk lattice constant.

Next, we compare  $\Delta G$ ,  $\Delta G_{\text{MD/MC-CEM}}$  and  $\Delta G_{\text{pair}}$  for an atom in each layer of a 2-dimensionally periodic surface for various bulk-terminated, low-index surfaces. This is a good test of the two-body approximation because the functions were derived from the bulk environment in which the coordination of the focus atom is always 12, but in which the distance between atoms changes. Changing the number of nearest neighbors at fixed distance is not equivalent.

Table I shows  $\Delta G$ ,  $\Delta G_{\text{MD/MC-CEM}}$  and  $\Delta G_{\text{pair}}$  per atom in each layer of the surface until the bulk value is reached for bulk-terminated, low-index Ni surfaces. Non-relaxed systems were chosen so that the differences in the numbers would be due to true differences in the method and not different relaxed geometries. Ni is shown as the example, but the behavior and conclusions hold for every system we have studied.

The table shows that  $\Delta G_{\text{pair}}$  is always smaller than or equal to  $\Delta G$ , while  $\Delta G_{\text{MD/MC-CEM}}$  is always larger than or equal to  $\Delta G$ . The difference between  $\Delta G_{\text{pair}}$

and  $\Delta G$  for an atom in the first layer of each of the (111), (100) and (110) surfaces is 0.08, 0.11 and 0.11 eV respectively. Equivalent differences in the atoms in the second layers are 0.01, 0.02 and 0.06 eV respectively. The large jump in error seen for the second layer atom in the (110) surface is due to the fact that this atom is missing one first nearest neighbor while the second layer atoms in the other surfaces are not missing any nearest neighbors. By the third layer for the most close-packed surfaces, and the fourth layer for the (110) surface, the atoms are in a sufficiently bulk-like environment that  $\Delta G_{\text{pair}}$  and  $\Delta G$  are identical.

It is important to note that since  $\Delta G_{\text{pair}}$  is derived from the bulk environment, it agrees with  $\Delta G$  in the bulk *by definition*. These results show that missing nearest neighbors, even if it is only one, causes the greatest differences between  $\Delta G_{\text{pair}}$  and  $\Delta G$ . The reason for this is that in the bulk an atom has many positive long-range interactions, as shown in Fig. 1. At the surface, the atom is missing many long-range interactions. When the two-body function values are summed, the result is too small.

$\Delta G_{\text{MD/MC-CEM}}$ , as observed earlier, is consistently larger than  $\Delta G$  at the surface, and is also exact for the bulk by definition. In fact,  $\Delta G_{\text{MD/MC-CEM}}$  seems relatively invariant to the changing coordination of the atom: an atom in the first layer of the (111), (100) and (110) surfaces has differences in  $\Delta G_{\text{MD/MC-CEM}}$  from the *bulk* of 0.02, 0.03 and 0.07 eV respectively. (Comparable differences in  $\Delta G$  and  $\Delta G_{\text{pair}}$  are 0.16, 0.20 and 0.28 eV and 0.24, 0.31 and 0.39 eV respectively.) This relative insensitivity is illustrated in Fig. 4, which shows  $\Delta G_{\text{MD/MC-CEM}}$  versus jellium density. Again, Ni is the example, but the result is true for all the systems studied.

There are also significant differences between  $\Delta G_{\text{MD/MC-CEM}}$  and  $\Delta G$  for mixed metal systems. Fig. 5 shows these differences for the  $\text{Ni}_{0.25}\text{Ag}_{0.75}$ ,  $\text{Ni}_{0.5}\text{Ag}_{0.5}$  and  $\text{Ni}_{0.75}\text{Ag}_{0.25}$  alloys. At the equilibrium lattice constants of the above three alloys, the difference between  $\Delta G$  and  $\Delta G_{\text{MD/MC-CEM}}$  is -0.19, -0.34 and -0.34 eV respectively.

In CEM-Pair, the mixed metal components of  $\Delta G$  are treated separately from the homogeneous atom contributions which gives the method greater flexibility than MD/MC-CEM in treating mixed metal systems. However, a major concern in deriving mixed metal two-body functions is the feasibility of using the same function for different combinations of the two metals. One test of this is to compare the two-body functions derived from several different combinations of Ni and Ag. Fig. 6a shows the difference between the Ni-Ag functions derived from the  $\text{Ni}_{0.25}\text{Ag}_{0.75}$  and  $\text{Ni}_{0.75}\text{Ag}_{0.25}$  alloy systems, and the Ni-Ag function derived from the  $\text{Ni}_{0.5}\text{Ag}_{0.5}$  alloy. The  $\text{Ni}_{0.5}\text{Ag}_{0.5}$  derived Ni-Ag two-body function underestimates  $\Delta G_{\text{mixed}}$  in the  $\text{Ni}_{0.25}\text{Ag}_{0.75}$  alloy over most of the region of interest. The opposite is true for the two-body function derived from the  $\text{Ni}_{0.75}\text{Ag}_{0.25}$  alloy.

Since the two-body function is an approximation of  $\Delta G$  for one interaction between two atoms (e.g. one Ni-Ag interaction), any difference between the functions is magnified when they are used to calculate the total  $\Delta G$  in a system which involves multiple Ni-Ag interactions. Using the two-body function derived for the  $\text{Ni}_{0.5}\text{Ag}_{0.5}$  alloy gives poor results for the  $\text{Ni}_{0.25}\text{Ag}_{0.75}$  and  $\text{Ni}_{0.75}\text{Ag}_{0.25}$  alloys, as seen in Figure 6b. The difference in  $\Delta G$  for these two alloys contains a reflection about zero, which indicates that the Ni-Ag function derived from the  $\text{Ni}_{0.5}\text{Ag}_{0.5}$  alloy is the best choice if we must use only one function.

It is important to note that the overall difference in  $\Delta G$  is much larger for the heterogeneous atom systems in Fig. 6b ( $\approx 0.03$  eV) than for the homogeneous atom system in Fig. 3 ( $\approx 10^{-7}$  eV). The small errors in the homogeneous atom system are purely numerical. In the heterogeneous atom systems, there are also physical differences which come into play. The cause of these in the NiAg system is the large size difference between the two atoms (i.e., the equilibrium lattice constant for Ag is 1.077 bohr larger than that for Ni). Recall that the numerical calculation of  $\Delta G$  involves the evaluation of a three dimensional integral dominated by the large densities near the nuclei. When one atom is significantly larger than another, the densities near the nucleus of the larger atom will dominate  $\Delta G$ . Because  $\Delta G$  is really a many-body quantity, this dominance does not vary in a two-body fashion as the number of large atoms in the unit cell changes, hence leading to the physical differences in  $g_2$  with different arrangements of atoms.

To test this idea, we looked at the NiCu alloy system where the equilibrium lattice constant difference is only 0.170 bohr. The differences in the two-body functions for three alloys of Ni and Cu are shown in Fig. 7a, and are an order of magnitude smaller than the differences in the Ni-Ag functions in Fig. 6a. We use the Ni-Cu function derived from the  $\text{Ni}_{0.5}\text{Cu}_{0.5}$  alloy function to calculate the difference between  $\Delta G$  and  $\Delta G_{\text{pair}}$  for two different alloys of Ni and Cu. The results, shown in Fig. 7b, prove that, indeed, for this system the single function does quite well for all Ni-Cu combinations, with an absolute error over the entire range of 0.002 eV or less.

To examine how the differences in  $\Delta G$  and  $\Delta G_{\text{pair}}$  change as a function of the

lattice size mismatch, we looked at the CuPd, CuRh and PdPt systems, where the lattice constant difference between the two metal atoms is 0.529, 0.359 and 0.057 bohr respectively. We then examined the differences between  $\Delta G$  and  $\Delta G_{\text{pair}}$  for combinations of atoms in the bulk alloy identical to those used for the NiAg and NiCu systems above, using the function derived from the  $A_{0.5}B_{0.5}$  alloy. The resulting curves are very similar to Fig. 6b and 7b in shape and are therefore not reproduced here. The maximum difference between  $\Delta G$  and  $\Delta G_{\text{pair}}$  is 0.065, 0.071 and 0.013 eV for the CuPd, CuRh and PdPt systems respectively. These differences do not scale in any simple way with the lattice constant difference.

### Total Interaction Energy Calculations

The total energy results used embedding energies determined from SCF-LMTO calculations<sup>7</sup>. Table II shows the minimized energies and corresponding bond lengths and vibrational frequencies of diatomic molecules found using the full theory and the two approximate methods. Plots of  $\Delta G$  for the Ni diatomic are shown in Fig. 8. The  $\Delta G_{\text{pair}}$  curve is consistently lower than and roughly parallel to the  $\Delta G$  curve. In Fig. 1, we saw that at moderate interatomic distances (small  $R^{-2}$ ) the two-body function,  $g_2(R)$ , is positive and at compressed interatomic distances (large  $R^{-2}$ ) it becomes negative. In the bulk lattice from which  $g_2(R)$  is derived, every atom has many long-range interactions which add up to  $\Delta G_{\text{pair}}$ . When there is only one interaction, we see that  $\Delta G_{\text{pair}}$  is too negative.

$\Delta G_{\text{MD/MC-CEM}}$  is consistently larger than or equal to  $\Delta G$ , and the difference between the two becomes quite large at compressed bond lengths. Recall that MD/MC-CEM approximates  $\Delta G$  associated with an atom in any environment by that

for an atom in a bulk environment of the same jellium density. However, an expanded bulk lattice is not an equivalent electronic environment to that of a diatomic molecule. Thus,  $\Delta G_{\text{MD/MC-CEM}}$  has the wrong shape and diverges from the  $\Delta G$  curve. The agreement for dissociation energies in Table II should be considered fortuitous, and due to the relatively flat binding energy predicted by the MD/MC-CEM method.

Of more relevance than diatomic molecules is the description of surface atoms. Table III shows the surface energies of the bulk-terminated, low-index surfaces of Ni, Cu, Rh, Pd and Ag. CEM-Pair predicts surfaces that are too stable relative to the exact values by between 0.24 and 0.32 J/m<sup>2</sup>. MD/MC-CEM predicts surface energies which are destabilized by between 0.12 and 0.37 J/m<sup>2</sup>. In both cases, the differences are roughly face independent.

At this point, we have examined how well the approximate methods calculate the energy of static homogeneous atom systems where the atoms have different coordination numbers than the bulk. Now we examine how the trends we have discussed so far affect the predictive capabilities of CEM, MD/MC-CEM and CEM-Pair. We do this by examining the differences in the predictions of surface relaxation of the (110) surface of Ni, Cu, Rh, Pd and Ag and mechanism for the diffusion of Cu on Cu(100).

Table IV presents the relaxation results. The CEM-Pair results show excellent agreement with the exact values for the relaxation of the first interlayer spacing. However, CEM-Pair predicts significant, oscillatory relaxation not seen by CEM. The reason for this lies in the fact that, as mentioned earlier, the loss of long-

range interactions affects  $\Delta G_{\text{pair}}$  more than it affects  $\Delta G$ . The end result is that CEM-Pair is more sensitive to long-range changes in the geometry. MD/MC-CEM, on the other hand, produces worse results since it is quite invariant to changes in the geometry (e.g.  $\Delta G_{\text{MD/MC-CEM}}$  is fairly flat as a function of jellium density in Fig. 4).

Next we consider the homodiffusion of Cu on Cu(100). There are two distinct mechanisms by which the diffusion can take place. In the replacement mechanism, the adatom replaces an atom in the first layer, and the displaced atom then moves to the four-fold hollow site diagonal from the adatom's original four-fold site. In the bridge mechanism, the diffusing atom hops from a four-fold hollow site to an adjacent four-fold hollow site over the intervening two-fold bridge site.

For the replacement mechanism, the barriers to diffusion are 0.44, 0.05 and 0.96 eV as predicted by CEM<sup>15</sup>, CEM-Pair and MD/MC-CEM<sup>15</sup>, respectively. For the bridge mechanism, the barriers to diffusion are 0.70, 0.31 and 0.68 eV respectively. Both CEM and CEM-Pair predict the replacement mechanism to be the preferred mechanism for the diffusion of Cu on Cu(100). The barrier to diffusion by the replacement mechanism is lower than the barrier to diffusion by the bridge mechanism by 0.26 eV for both methods. As we noted earlier, CEM-Pair predicts surface geometries to be too stable. In this case, CEM-Pair finds each of the transition states to be too stable by 0.39 eV relative to the initial and final states.

MD/MC-CEM does not show agreement with CEM and predicts the bridge mechanism to be the preferred mechanism by 0.28 eV for the diffusion of Cu on Cu(100). This is because  $\Delta G_{\text{MD/MC-CEM}}$  increases more quickly with density than it should (see Fig. 9). The difference is not too large at the four-fold site or the bridge

site because these are relatively low-density sites. However, the replacement transition state is a very crowded, high density configuration. Consequently,  $\Delta G_{\text{MD/MC-CEM}}$  is too repulsive at this geometry compared to  $\Delta G_{\text{MD/MC-CEM}}$  at the initial and final geometries. Thus, the barrier for the replacement mechanism is too repulsive compared to the barrier for the bridge mechanism.

A major motivation behind this work was to describe large bimetallic systems accurately. We have discussed the difficulties of using the same two-body function for alloys with large size mismatch and examined the limits of the approximation. Now we use these two-body functions to study the energy of formation for alloys.

In Table V, we present the energy of formation for bulk alloys where the atoms are present in a 1:1 ratio. The energy of formation is calculated as follows:

$$\Delta E_f(\text{A}_{0.5}\text{B}_{0.5}) = E_{\text{coh}}(\text{A}_{0.5}\text{B}_{0.5}) - \frac{1}{2}E_{\text{coh}}(\text{A}) - \frac{1}{2}E_{\text{coh}}(\text{B}) \quad (10)$$

where  $E_{\text{coh}}$  is the cohesive energy per atom in the bulk lattice. The energies of formation predicted by CEM-Pair agree quite well with the exact values, as one would expect since the systems under consideration are exactly those from which the mixed two-body functions are derived. The differences seen between CEM and CEM-Pair are purely numerical and on the order of a few meV/atom. These values contrast with the MD/MC-CEM energies of formation. The largest difference is for  $\text{Ni}_{0.5}\text{Ag}_{0.5}$ , where the CEM-Pair energy of formation is 9.0 kJ/mol lower than the MD/MC-CEM value.

To see what effect different Ni-Ag two-body functions would have on the predicted energy of formation, we used the Ni-Ag two-body functions derived from

the  $\text{Ni}_{0.25}\text{Ag}_{0.75}$  and the  $\text{Ni}_{0.75}\text{Ag}_{0.25}$  alloys to predict the energy of formation of the  $\text{Ni}_{0.5}\text{Ag}_{0.5}$  alloy. The resulting values are 1.19 and 1.40 kJ/mol respectively, which differ by 0.10 and 0.11 kJ/mol from the value in Table V. These differences are smaller than the numerical differences seen above between the CEM and CEM-Pair energies of formation.

## CONCLUSIONS

Finding a way to approximate the exact kinetic-exchange-correlation correction energy within effective medium type theories is important if these methods are going to be able to study large systems. Here we have examined and compared two different methods of approximating this many-body quantity: 1/ as a function of the jellium density; and 2/ as a sum of two-body functions.

As we have seen, each method has weaknesses.  $\Delta G_{\text{MD/MC-CEM}}$  is too insensitive to changes in the electron density.  $\Delta G_{\text{pair}}$  works best for extended systems when atoms are present at both short and long distances from the atom of interest. In addition, there are problems in deriving accurate mixed two-body functions when the atoms have a large size mismatch. For best results the exact, numerical integration of  $\Delta G$  is still preferable, provided the system is small enough to make this feasible.

However, these approximate methods also have important strengths. MD/MC-CEM does the better job for diatomics, and does an adequate job at calculating surface energies. CEM-Pair does an adequate job of calculating surface energies and a much better job of calculating the energies of formation of bulk alloys. More importantly, CEM-Pair does a very good job of describing processes on metal surfaces, such as surface relaxation and the homodiffusion of Cu on Cu(100). We therefore conclude that estimating the kinetic-exchange-correlation energy with a two-body function is perfectly valid as long as the limitations of this approximation, which we have detailed here, are taken into consideration.

Now that we can describe the energies of formation accurately with a faster method, we can hope to describe larger mixed metal systems more accurately, such as the behavior of bimetallic clusters (e.g. segregating or alloying), molecular dynamic simulations of epitaxy, etc. These are topics for future work.

One can imagine additional modifications to the CEM-Pair approach that would improve the accuracy of the method. One approach might be to approximate  $\Delta G$  with a function that depends on both the jellium density and a two-body function (i.e., some kind of combination of  $\Delta G_{\text{MD/MC-CEM}}$  and  $\Delta G_{\text{pair}}$ ). Another possibility might be to include a coordination-dependent scaling factor in  $\Delta G_{\text{pair}}$  to bring it into perfect agreement with  $\Delta G$ . In other words, scale the  $\Delta G_{\text{pair}}$  curve in Figs. 8 and 9 as a function of the number of nearest neighbors so that it lies exactly on the  $\Delta G$  curve.

**ACKNOWLEDGEMENTS**

One of us (S.B.S.) thanks Procter & Gamble for financial support. This work was supported in part by NSF grant CHE-8921099. This work was supported also in part by the Division of Chemical Sciences, Office of Basic Energy Sciences of the U.S. Department of Energy through the Ames Laboratory, which is operated for the U.S. DOE by Iowa State University under Contract No. W-7405-Eng-82. All calculations were performed on the Silicon Graphics 4D/380S purchased by an NSF instrumentation grant.

**REFERENCES**

1. R. G. Parr and W. Yang, *Density-Functional Theory of Atoms and Molecules* (Oxford, New York, 1989).
2. J. D. Kress and A. E. DePristo, *J. Chem. Phys.* **87**, 4700 (1987).
3. J. D. Kress and A. E. DePristo, *J. Chem. Phys.* **88**, 2596 (1988).
4. J. D. Kress, M. S. Stave and A. E. DePristo, *J. Chem. Phys.* **93**, 1556 (1989).
5. T. J. Raeker and A. E. DePristo, *Phys. Rev. B* **39**, 9967 (1989).
6. M. S. Stave, D. E. Sanders, T. J. Raeker and A. E. DePristo, *J. Chem. Phys.* **93**, 4413 (1990).
7. S. B. Sinnott, M. S. Stave, T. J. Raeker and A. E. DePristo, *Phys. Rev. B* **44**, 8927 (1991).
8. T. J. Raeker and A. E. DePristo, *Int. Rev. Phys. Chem.* **10**, 1 (1991).
9. M. S. Daw and M. I. Baskes, *Phys. Rev. B* **29**, 6443 (1984); M. S. Daw, *Phys. Rev. B* **39**, 7441 (1989).
10. F. Ercolessi, M. Parrinello and E. Tosatti, *Surf. Sci.* **177**, 314 (1986); F. Ercolessi, M. Parrinello, and E. Tosatti, *Philos. Mag.* **A58**, 213 (1988) and references therein.
11. M. W. Finnis and J. E. Sinclair, *Phys. Mag. A* **50**, 45 (1984); M. W. Finnis, A. T. Paxton, D. G. Pettifor, A. P. Sutton, and Y. Ohta, *Philos. Mag.* **A58**, 143 (1988).
12. A. E. DePristo and J. D. Kress, *Phys. Rev. A* **35**, 438 (1987).
13. A. E. DePristo and J. D. Kress, *J. Chem. Phys.* **86**, 1425 (1987); J. P. Perdew,

- Phys. Rev. Lett. **55**, 1665 (1985); A. D. Becke, J. Chem. Phys. **84**, 4524 (1986);  
S. K. Ghosh and R. G. Parr, Phys. Rev. A **34**, 785 (1986); O. Gunnarsson, M.  
Johnson and B. I. Lundqvist, Phys. Rev. B **20**, 3136 (1979).
14. O. Gunnarsson and B. I. Lundqvist, Phys. Rev. B. **13**, 4274 (1976).
  15. L. S. Perkins and A. E. DePristo, Surf. Sci. (to be submitted).
  16. T. J. Raeker and A. E. DePristo, J. Phys. C (to be submitted).

**Table I:** Values of  $\Delta G$  (in eV) for the low-index, bulk-terminated Ni surface layers.

Surface	Layer	$\Delta G$	$\Delta G(\text{MD/MC-CEM})$	$\Delta G$ (pair)
Ni(111)	1	0.78	0.92	0.70
	2	0.95	0.94	0.94
	3	0.94	0.94	0.94
Ni(100)	1	0.74	0.91	0.63
	2	0.96	0.94	0.94
	3	0.94	0.94	0.94
Ni(110)	1	0.66	0.87	0.55
	2	0.92	0.95	0.86
	3	0.95	0.94	0.94
	4	0.94	0.94	0.94

**Table II:** Predicted equilibrium values for selected diatomics; the binding energy ( $D_e$ ), the bond length ( $R_e$ ) and the vibrational frequency ( $\omega_e$ ).

	Method	$D_e$ (eV)	$R_e$ (bohr)	$\omega_e$ ( $\text{cm}^{-1}$ )
Ni <sub>2</sub>	CEM	1.66	3.57	445
	MD/MC-CEM	1.82	3.89	424
	CEM-Pair	3.64	3.27	484
Cu <sub>2</sub>	CEM	0.98	3.50	472
	MD/MC-CEM	1.16	4.25	116
	CEM-Pair	3.44	3.15	571
Rh <sub>2</sub>	CEM	2.28	4.03	310
	MD/MC-CEM	2.42	4.32	233
	CEM-Pair	3.62	3.94	306
Pd <sub>2</sub>	CEM	1.04	4.43	95
	MD/MC-CEM	1.54	5.03	136
	CEM-Pair	2.23	4.12	197
Ag <sub>2</sub>	CEM	1.94	4.81	272
	MD/MC-CEM	2.43	4.93	297
	CEM-Pair	2.98	4.75	244

**Table III:** The surface energies (in  $J/m^2$ ) for some unrelaxed low-index Ni, Cu, Rh, Pd and Ag surfaces. The % difference between the approximate methods and CEM is shown in parentheses.

Surfaces	CEM	MD/MC-CEM	CEM-Pair
Ni(111)	2.13	2.54 (19.2)	1.86 (-12.7)
Ni(100)	2.30	2.70 (17.4)	1.97 (-14.3)
Ni(110)	2.49	2.92 (17.3)	2.17 (-12.9)
Cu(111)	1.56	1.77 (13.5)	1.32 (-15.4)
Cu(100)	1.72	1.93 (12.2)	1.44 (-16.3)
Cu(110)	1.90	2.13 (12.1)	1.64 (-15.9)
Rh(111)	2.39	2.73 (14.2)	2.15 (-10.0)
Rh(100)	2.55	2.88 (12.9)	2.31 (-9.41)
Rh(110)	2.77	3.14 (13.4)	2.51 (-9.39)
Pd(111)	1.65	1.89 (14.5)	1.38 (-16.4)
Pd(100)	1.76	2.00 (13.6)	1.50 (-14.8)
Pd(110)	1.91	2.19 (14.7)	1.64 (-14.1)
Ag(111)	0.90	1.02 (13.3)	0.64 (-28.9)
Ag(100)	0.96	1.10 (14.6)	0.71 (-26.0)
Ag(110)	1.07	1.23 (15.0)	0.82 (-23.4)

**Table IV:** Relaxation results for CEM, MD/MC-CEM and CEM-Pair for the (110) non-reconstructing fcc metal surfaces.

	Method	$\Delta d_{12}$ (%)	$\Delta d_{23}$ (%)	$\Delta d_{34}$ (%)
Ni(110)	CEM	-12.3	0.5	-0.3
	MD/MC-CEM	-4.1	0.3	-0.5
	CEM-Pair	-14.7	3.8	-1.7
Cu(110)	CEM	-15.0	1.4	-0.1
	MD/MC-CEM	-7.8	1.1	-0.8
	CEM-Pair	-19.0	3.4	-1.2
Rh(110)	CEM	-7.4	-0.2	-0.3
	MD/MC-CEM	-4.3	0.6	-0.5
	CEM-Pair	-12.2	2.9	0.0
Pd(110)	CEM	-7.8	0.1	-0.8
	MD/MC-CEM	-3.7	0.6	-0.5
	CEM-Pair	-8.1	1.7	-1.1
Ag(110)	CEM	-7.9	-0.2	0.7
	MD/MC-CEM	-4.4	1.0	0.0
	CEM-Pair	-10.1	2.2	-0.6

**Table V:** Energies of formation calculated with CEM<sup>a</sup>, CEM-Pair and MD/MC-CEM<sup>a</sup>, in that order, for A<sub>0.5</sub>B<sub>0.5</sub> bulk alloys of selected combinations of Ni, Cu, Rh, Pd and Ag. The units are kJ/mol.

	Cu	Rh	Pd	Ag
Ni	2.17	-	-6.46	1.63
	2.16	-	-6.27	1.29
	3.06	-	-1.16	10.58
Cu	-	8.13	0.18	-
	-	8.30	-0.10	-
	-	2.29	-1.80	-

<sup>a</sup> Results from Ref. 16.

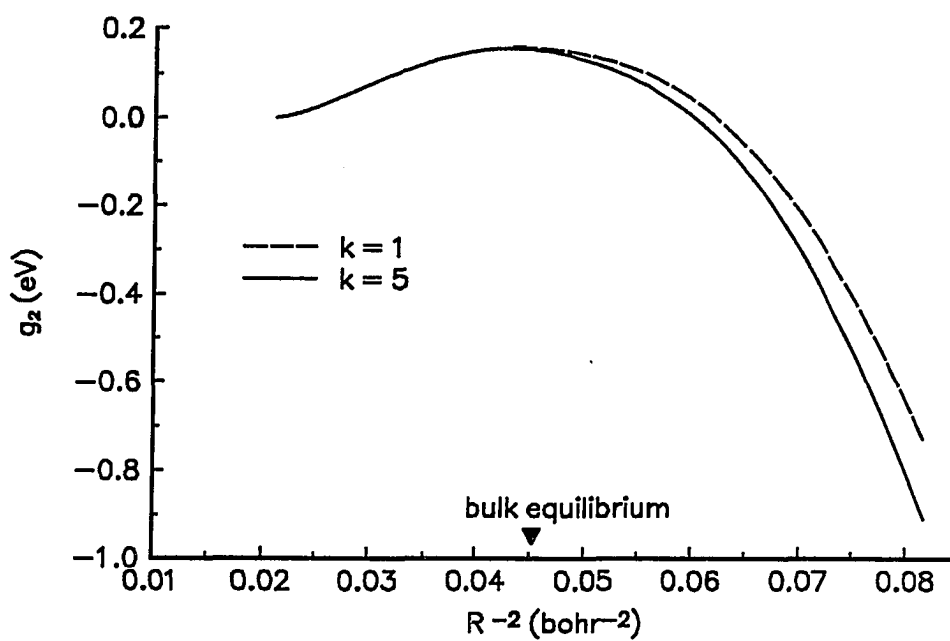


**Fig. 1:** The Ni-Ni two-body function as a function of iteration (Eq. 9). The fifth iteration is the last. It is clear that the convergence is very rapid.

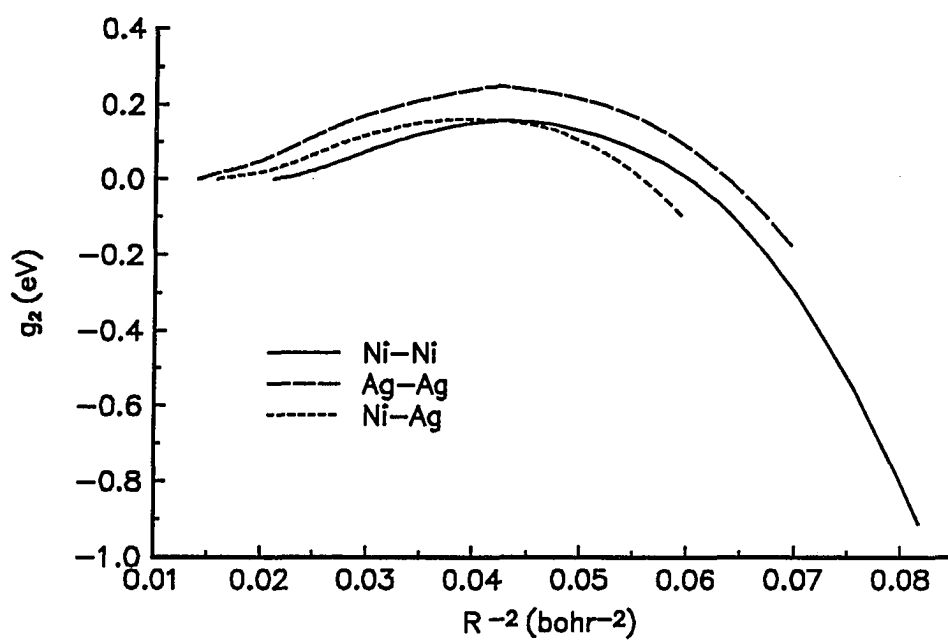


**Fig. 2:** The Ni-Ni, Ag-Ag and Ni-Ag two-body functions. The Ni-Ag function shown is derived from the  $\text{Ni}_{0.5}\text{Ag}_{0.5}$  bulk lattice.

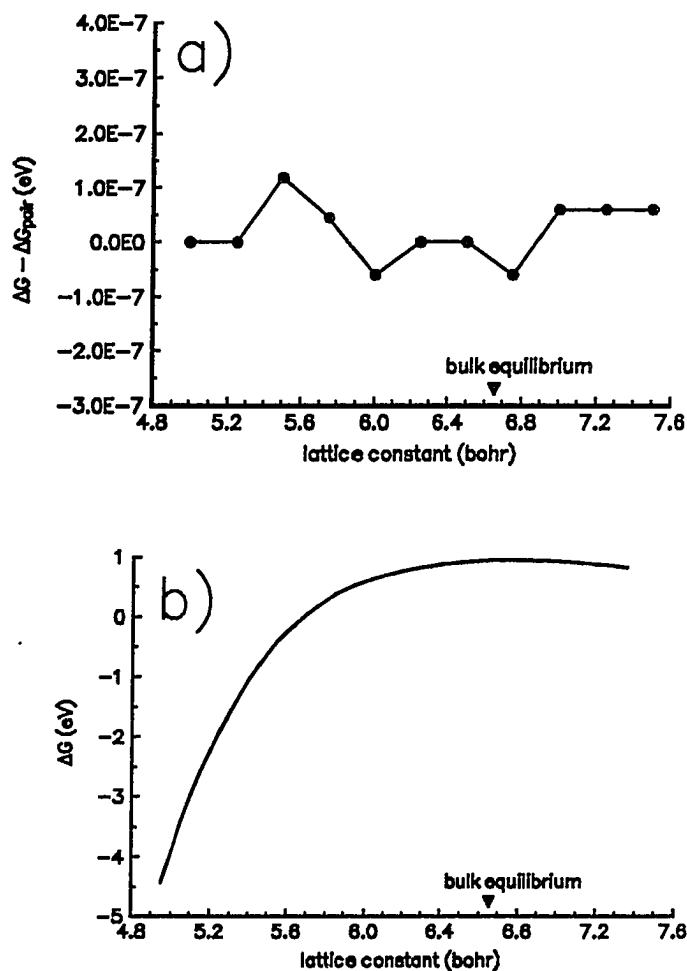


**Fig. 3:** a) The difference between  $\Delta G$  and  $\Delta G_{\text{pair}}$  for Ni over the physically relevant region of  $0.75a_0 - 1.10a_0$ . b)  $\Delta G$  as a function of lattice constant for Ni over the same region. The bulk equilibrium lattice constant for Ni is indicated on both figures.

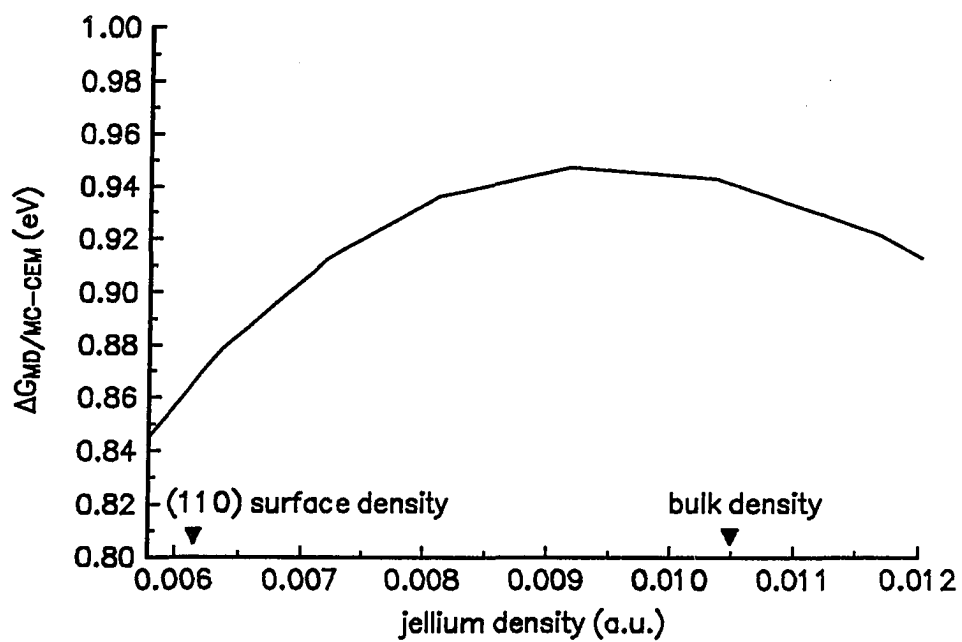


**Fig. 4:**  $\Delta G_{MD/MC-CEM}$  versus jellium density for Ni. The density of an atom at the surface of Ni(100) and in the bulk lattice is indicated by the triangles.

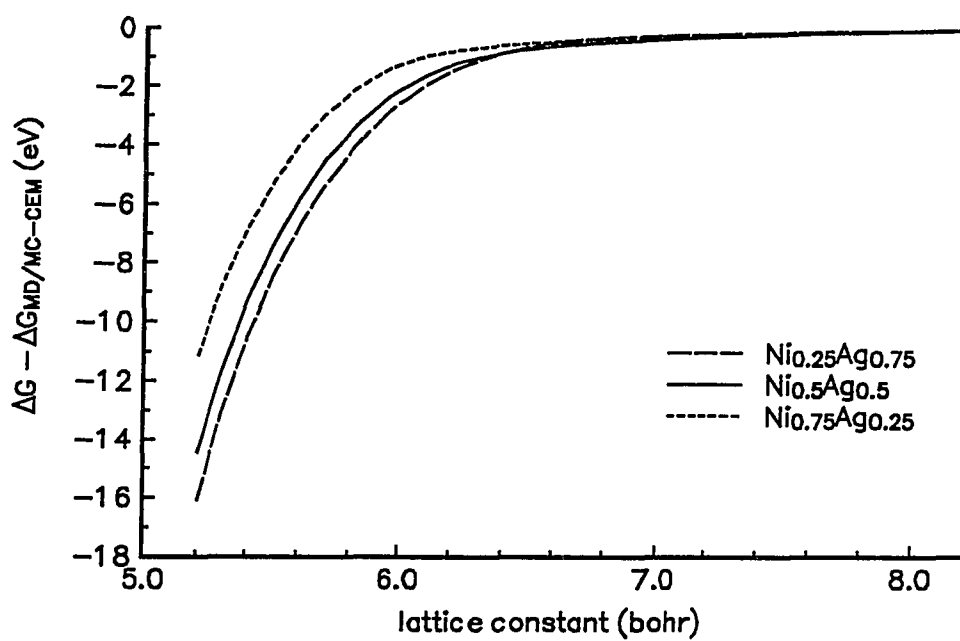


**Fig. 5:** The difference between  $\Delta G$  and  $\Delta G_{MD/MC-CEM}$  versus lattice constant for  $Ni_{0.25}Ag_{0.75}$ ,  $Ni_{0.5}Ag_{0.5}$  and  $Ni_{0.75}Ag_{0.25}$ .

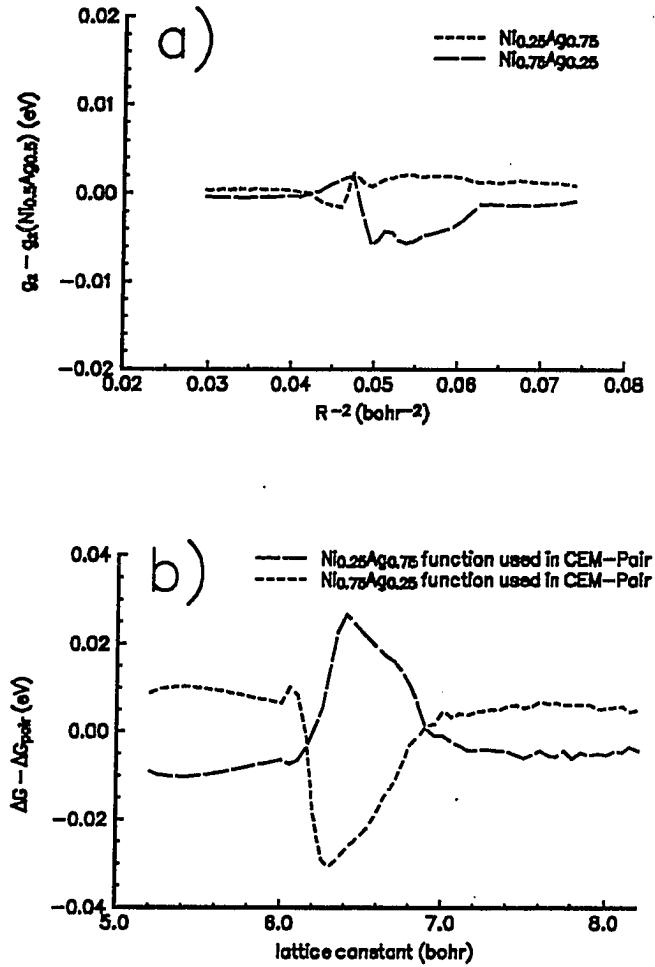


**Fig. 6:** a) The difference between the  $\text{Ni}_{0.25}\text{Ag}_{0.75}$  and  $\text{Ni}_{0.75}\text{Ag}_{0.25}$  functions and the  $\text{Ni}_{0.5}\text{Ag}_{0.5}$  function. b) The difference between  $\Delta G$  and  $\Delta G_{\text{pair}}$  for the  $\text{Ni}_{0.25}\text{Ag}_{0.75}$  and  $\text{Ni}_{0.75}\text{Ag}_{0.25}$  bulk alloy systems. Each  $\Delta G_{\text{pair}}$  calculation here uses the Ni-Ag two-body function derived from the  $\text{Ni}_{0.5}\text{Ag}_{0.5}$  alloy system.

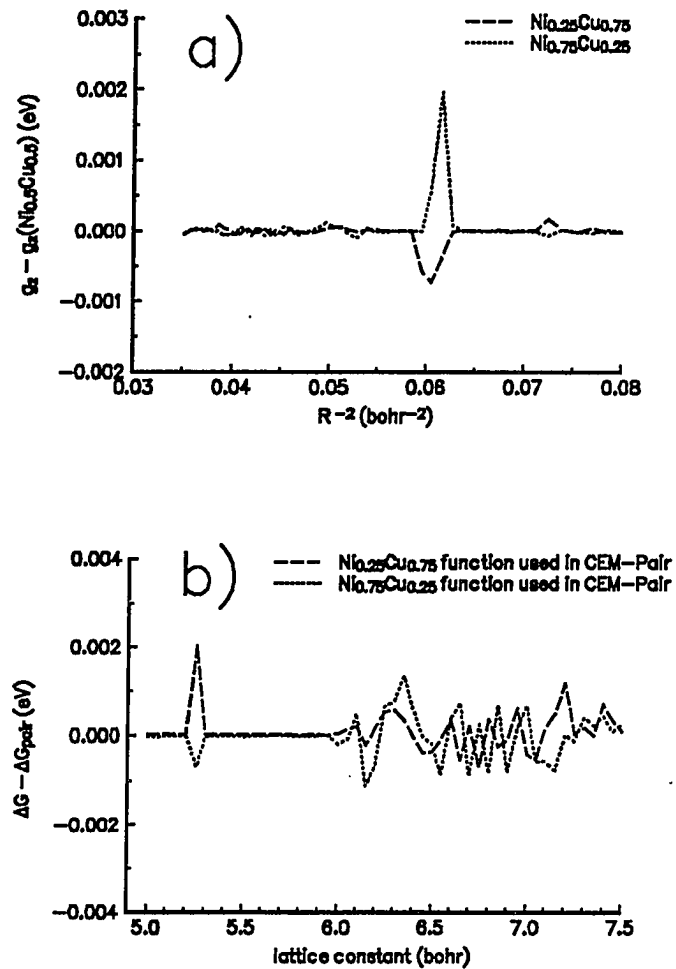


**Fig. 7:**

a) The difference between the  $\text{Ni}_{0.25}\text{Cu}_{0.75}$  and  $\text{Ni}_{0.75}\text{Cu}_{0.25}$  functions and the  $\text{Ni}_{0.5}\text{Cu}_{0.5}$  function. b) The difference between  $\Delta G$  and  $\Delta G_{\text{pair}}$  for the  $\text{Ni}_{0.25}\text{Cu}_{0.75}$  and  $\text{Ni}_{0.75}\text{Cu}_{0.25}$  bulk alloy systems. Each  $\Delta G_{\text{pair}}$  calculation here uses the Ni-Cu two-body function derived from the  $\text{Ni}_{0.5}\text{Cu}_{0.5}$  alloy system.

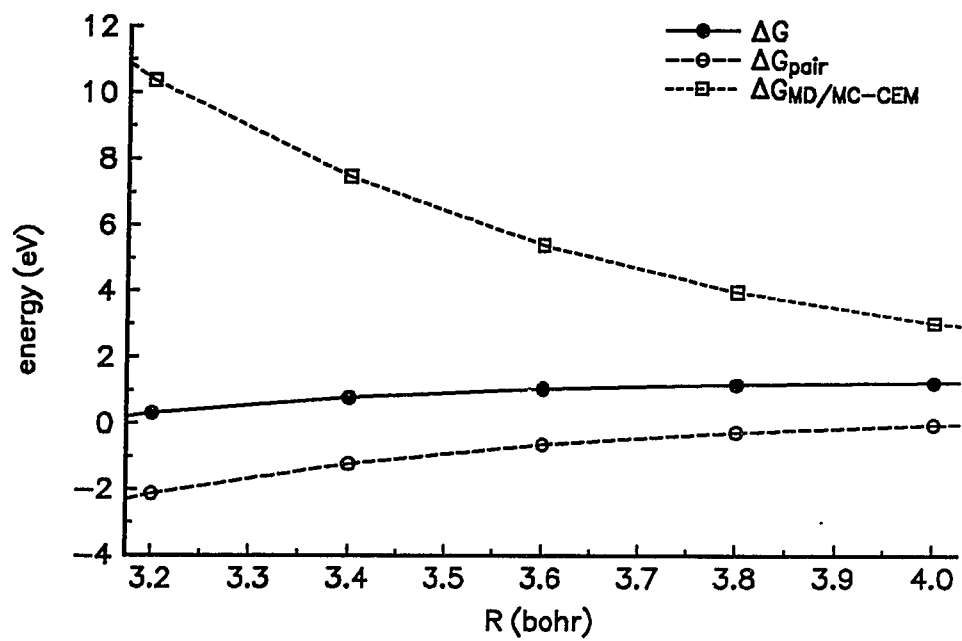


**Fig. 8:** The kinetic-exchange-correlation energy curves for Ni<sub>2</sub> as a function of the bond length.

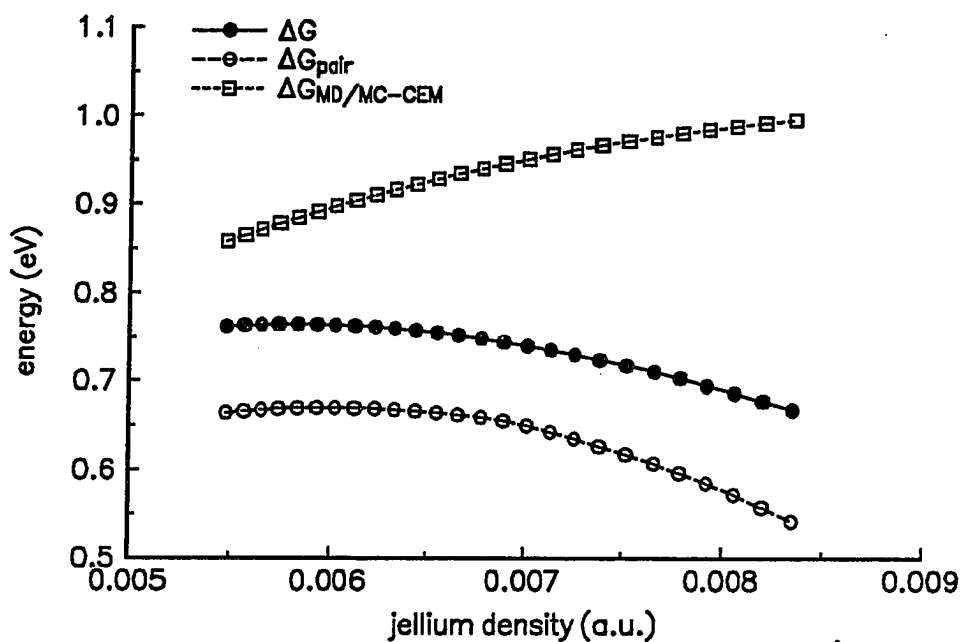


**Fig. 9:** The kinetic-exchange-correlation energy curves for a Cu atom on the surface of the Cu(100) surface as a function of the jellium density. The density was varied by contracting the first interlayer spacing from 0 - 25%.

## GENERAL CONCLUSIONS

This work covers a wide range of theoretical chemistry. In paper 1, a previously developed method is used to gain understanding of the different types of bonding that can occur in small silicon clusters. The calculations provide much information, such as binding energies, equilibrium geometries and the hybridization of silicon atoms that is of chemical interest. Paper 2 explores the limitations of a theoretical technique and the consequences of improving on an existing method. This is important to better understand the theory and the physics of the process being studied. Even negative results are useful in this regard. Finally, paper 3 details the development of a new theoretical technique. The paper discusses the motivation behind the work, the actual derivation and the testing of the finished method.

This work also emphasizes the usefulness of DFT in electronic structure calculations. Paper 1 shows how first principles, non-local DFT calculations can provide chemically accurate data that show almost perfect agreement with experiment without any empirical corrections. Papers 2 and 3 show how accurate values of the kinetic-exchange-correlation correction energy are crucial to CEM's success at describing processes at metal surfaces. DFT thus has an important role to play in both first principles and semi-empirical applications.

## GENERAL REFERENCES

1. For a trial density,  $n(\vec{r})$  such that  $n(\vec{r}) \geq 0$  and  $\int n(\vec{r}) d\vec{r} =$  the number of electrons,  $E_0 \leq E[n(\vec{r})]$ , where  $E_0$  is the true ground state energy.
2. A functional is a function of a function and is denoted by square brackets. For example,  $f(x)$  is a function of  $x$ ;  $G[f(x)]$  is a functional of  $f(x)$ .
3. P. Hohenberg and W. Kohn, Phys. Rev. **136**, B864 (1964).
4. W. Kohn and L. J. Sham, Phys. Rev. **140**, A1133 (1965).
5. P. A. M. Dirac, Proc. Cambridge Philos. Soc. **26**, 376 (1930).
6. O. Gunnarsson and B. I. Lundqvist, Phys. Rev. B **13**, 4274 (1976).
7. S. H. Vosko, L. Wilk and M. Nussair, Can. J. Phys. **58**, 1200 (1980).
8. J. P. Perdew and Y. Wang, Phys. Rev. B **33**, 8800 (1986); J. P. Perdew, Phys. Rev. B **33**, 8822 (1986).
9. D. R. Salahub, R. Fournier, P. Mlynarski, I. Papai, A. St-Amant and J. Ushio, in *Density Functional Methods in Chemistry*, edited by J. K. Labanowski and J. Andzelm (Springer, New York, 1991).
10. A. St-Amant and D. R. Salahub, Chem. Phys. Lett. **169**, 387 (1990).
12. M. S. Daw and M. I. Baskes, Phys. Rev. B **29**, 6443 (1984); M. S. Daw, Phys. Rev. B **39**, 7441 (1989).
13. F. Ercolessi, M. Parrinello and E. Tosatti, Surf. Sci. **177**, 314 (1986); F. Ercolessi, M. Parrinello and E. Tosatti, Philos. Mag. **A58**, 213 (1988); M. W. Finnis and J. E. Sinclair, Phys. Mag. A **50**, 45 (1984).
14. M. W. Finnis, A. T. Paxton, D. G. Pettifor, A. P. Sutton and Y. Ohta, Philos.

- Mag. A58, 143 (1988).
15. J. D. Kress and A. E. DePristo, *J. Chem. Phys.* **87**, 4700 (1987).
  16. J. D. Kress and A. E. DePristo, *J. Chem. Phys.* **88**, 2596 (1988).
  17. J. D. Kress, M. S. Stave and A. E. DePristo, *J. Phys. Chem.* **93**, 1556 (1989).
  18. T. J. Raeker and A. E. DePristo, *Phys. Rev. B* **39**, 9967 (1989).
  19. M. S. Stave, D. E. Sanders, T. J. Raeker and A. E. DePristo, *J. Chem. Phys.* **93**, 4413 (1990).
  20. T. J. Raeker and A. E. DePristo, *Int. Rev. Phys. Chem.* **10**, 1 (1991).
  21. A. E. DePristo and J. D. Kress, *Phys. Rev. A* **35**, 438 (1987).